AN ABSTRACT OF THE DISSERTATION OF

Walter C. Hurlbut for the degree of Doctor of Philosophy in Physics presented on October 19, 2006.
Title: The Nonlinear Optical Properties of Gallium Arsenide Pertaining to Terahertz Generation.

Abstract Approved:

Yun-Shik Lee

Gallium arsenide shows excellent promise for terahertz generation using mid infrared. This is for two reasons. First, the indices of refraction for the terahertz (n_{THz}=3.61 at 1 THz) and mid infrared (n_{opt}=3.431 at 2 μm) are close allowing a long interaction length. Second, the linear absorption is low at terahertz frequencies (α_{THz}=.5 to 4.5 cm^{-1} for 1 to 3 THz). Since gallium arsenide is a direct bandgap material, multiphoton absorption and nonlinear refraction are issues for efficiency and system design in the mid infrared. In fact, linear absorption makes this material opaque at or below 870 nm. Additionally, two photon absorption is quite pronounced between 870 nm and 1.74 μm.

I will present the theory then the experimental data for two and three photon absorption (870 nm to 1.74 μm and 1.74 μm to 2.61 μm, respectively) as well as for nonlinear refraction. The three photon absorption has a minimum at 2 μm in the spectral range of 1.74 to 2.61 μm thus it is the preferred wavelength for terahertz generation. At 2 μm the anisotropy in the three photon absorption was almost 50 %. The nonlinear refraction remains fairly constant in this range as expected. However at 2 μm the anisotropy in nonlinear refraction was only 16% as compared with the predicted factor of

2. Qualitatively, the anisotropic behavior of the nonlinear refraction still conforms to the expected symmetry class of zincblende crystals.

Terahertz time domain spectroscopy will be discussed on both theoretical and experimental levels. The results will show that terahertz generation is promising in the mid infrared range for wavelengths 2 μm and above. At 2 μm I demonstrate the advantages of a quasi-phase matched structure. One, the inverting structure generates a narrow band source. Additionally, shaped domains map to the terahertz electric field allowing shaped pulses. Also, of benefit is the increase in power production from having a longer effective interaction path in the crystal.

The Nonlinear Optical Properties of Gallium Arsenide Pertaining to Terahertz Generation

by

Walter C Hurlbut

A DISSERTATION

submitted to

Oregon State University

in partial fulfillment of
the requirements for the
degree of

Doctor of Philosophy

Presented October 19, 2006

Commencement June 2008

Doctor of Philosophy dissertation of Walter C. Hurlbut
Presented on October 19, 2006.

APPROVED:

Major Professor, representing Physics

Chair of the Department of Physics

Dean of the Graduate School

I understand that my dissertation will become part of the permanent collection of Oregon State University libraries. My signature below authorizes release of my dissertation to any reader upon request.

Walter C. Hurlbut, Author

ACKNOWLEDGEMENTS

The author expresses sincere appreciation to DARPA (Research done under DARPA grant FA9550-04-1-0465) and to Vladimir Kozlov of Microtech Instruments. (Provider of quality samples and helped provide support during completion of this document)

CONTRIBUTION OF AUTHORS

On various experiments different people contributed as is listed in each experimental section. Dr. Yun-Shik Lee, Jeremy Danielson, Naaman Amer, Bryan Norton, Vladimir Kozlov, and Konstantin Vodopyanov all contributed to the data collection. Yun-Shik Lee and Konstantin Vodopyanov were the principle data analysts with discussion and interpretation being a team effort. Dr. Yun-Shik Lee and Dr. Konstantin Vodopyanov wrote much of the excerpted sections from collected publications in Chapter 12 with editorial help from the author.

TABLE OF CONTENTS

TABLE OF CONTENTS (Continued)

LIST OF FIGURES

LIST OF FIGURES

LIST OF FIGURES

Figure Page

LIST OF FIGURES

Figure Page

LIST OF FIGURES

Figure Page

LIST OF TABLES

Part I

Introduction

1 Mission Statement

Terahertz (THz=10^{12} hertz) generation using gallium arsenide (GaAs) is promising for numerous reasons. The first is its large second order susceptibility. GaAs is well studied with an existing large manufacturing base. GaAs also has a small refractive index mismatch between the mid infrared and THz frequency ranges making it ideal for quasi-phase matching. Additionally, GaAs has low absorption in both the mid infrared (IR) and THz frequency ranges making it very promising for use in devices such as optical parametric oscillators.

On the other hand, GaAs has a band gap of 1.43 eV[1] which corresponds to a photon wavelength of 870 nanometers thus standard near infrared generation techniques are inadequate due to direct absorption. Also; nonlinear effects such as nonlinear refraction, multiphoton absorption, and optical damage must be taken into account when designing successful nonlinear devices for THz wave generation using GaAs.

The first part of this dissertation presents the theory and experimental confirmation of nonlinear absorption and refraction in GaAs for the mid infrared range.

In the second part, I discuss the application of GaAs to THz wave generation. The theory and experimental results confirming the promise of quasi-phase matched GaAs are presented showing a world record level of efficiency ($\tilde{}10^{-3}$)[2] for optical to THz wave conversion using a mid infrared input beam.

2 Nonlinear Optical Properties and THz pulse Generation

The wavelength corresponding to the direct bandgap of GaAs is 870 nm. This makes it opaque to shorter wavelengths and causes free carrier generation which results in strong absorption in the THz frequency range. So, unlike zinc telluride, the use of near infrared femtosecond duration pulsed lasers as an optical pump such as a Ti-sapphire laser is excluded. One must go to wavelengths longer than the band gap equivalent wavelength to pump GaAs in standard fashion.

Previous work in theory[3] and experimental studies[4] also indicated that GaAs has strong two photon absorption. As a result, our team looked to the previously unstudied three photon absorption range in the mid infrared range. Theoretical modeling indicated that just above 2 microns was promising.

The first step then was to characterize the multiphoton absorption using the 'z-scan' technique. by physically moving the sample along the propagation axis through a focal plane of a focused beam while measuring the transmitted signal one can using the sample thickness, spatial profile, incident power, and transmitted power determine the appropriate nonlinear absorption at a given wavelength. Additionally, by measuring the central beam power one can determine the nonlinear refraction as well.

This was done for selected wavelengths of 2, 3, 4, and 5 photon absorption. The data was fit to existing theory showing reasonable agreement. Some expected effects not compensated for in the theory were evident such as the tail 2 photon absorption seen in the low wavelength range of the 3 photon absorption one would expect at room temperature.[2]

The nonlinear refraction was shown to be dominated by the second order refraction as expected at the same frequencies as chosen in the multiphoton absorptions study using the 'closed aperture z-scan' technique.

Even if one used a longer wavelength to reach into higher order absorptions where one can go to higher intensities at some point the self phase modulation and beam distortion produced by nonlinear refraction will limit system design. At some critical intensity one reaches the surface damage threshold and this is the ultimate additional limiting factor to consider.

3 Generation and Detection of THz Pulses

Once characterization of the nonlinear optical properties of GaAs had been completed the next step was to study the optical to THz wave generation properties and compare them to theory. This work is interesting for numerous reasons which can be understood once one knows more about the THz spectral range.

The terahertz frequency band is in the far infrared just above the microwave range. This band extends from about .1 to 10 THz. It is just above the range electronics can operate in and just below the typical optical source range. This makes the THz range difficult to generate and detect.

This range is interesting for a number of reasons. Many molecules have rotational or vibrational spectra in this range. Micromachining is capable of building structures on scale with this range as the wavelength corresponding to 1 THz is 300 μm. So one can readily study the behavior of photonic crystals in the THz band. There are phonon resonances in condensed matter structures which among its variety of uses allows characterization of transport properties in semiconductors. For semiconductor nanostructures quantum beats are in this range as well.

There are numerous ways to generate THz. Backwards wave oscillators are an older technology developed for producing THz from .03 to about 1.5 THz as a continuous wave source with a fairly high intensity relative to most

other sources with narrow bandwidth [5] [6]. Another method to produce THz waves is to use a photoconductive switch driven by a femtosecond laser this technique generates single cycle broadband pulses.[7] Optical rectification in noncentrosymmetric crystals is one of the most common methods and this thesis will focus on this technique. On the high end, there are particle accelerator sources like free electron lasers, which are very expensive, but produce strong THz output.

Just as there are many forms of THz generation, there are numerous methods of detection as well. Some semiconductor detectors operate up to 1 THz with pulsed repetition rates up to 20 GHz. Pyroelectric detectors work to 3 THz with a window to block out background thermal sources. In an environment where this is unnecessary, they can operate as high as 20 THz. [6] The primary issue for pyroelectric detectors is that the signal must be chopped no faster than 30 Hz. Similarly, Golay cells can operate across the whole THz spectrum but have a slow response time limiting them to about 40 Hz. Additionally, Golay cells, detectors using the thermal expansion of a gas to measure THz radiation, are extremely vibration sensitive. Bolometers can detect THz waves with great sensitivity but require cryogenic fluids. The detection method which is of primary importance to this thesis is electro-optical detection. This detection method utilizes the electro-optic effect where an electric field rotates the polarization of an optical pules inside of a noncentrosymmetric crystal.[8]

Once one has methods for both generation and detection the next step

is the characterization of the emitter (GaAs) and the understanding of the effective interaction length so that one can develop period inverting structures to increase the effective interaction length. These structures are known as quasi-phase matched structures.

The length during which the optical pulse envelope and the generated THz wave are co-propagating in a temporally overlapped fashion is known as 'the walk off length'. Once the optical pulse envelope no longer overlaps the generated THz wave then constructive interference increasing the THz wave no longer takes place. After this length the optical pulse interferes destructively with the THz wave and so this length is the optimal length for THz wave generation in a material in which the optical index of refraction differs from the generated THz index of refraction.

To overcome this one can align layers whose thickness is the walk off length along the propagation direction. Each layer has its structure rotated 180 degrees from the previous about the propagation axis so the electric field of the THz wave of that layer is of opposite direction of the immediate preceding or following layer. This, in effect, builds a multi-cycle THz wave one half wavelength at a time from the back to the front of the wave in a similar way to how a boat builds waves from bow shock in water.

By use of this technique the output power and conversion efficiency are increased above the capability of bulk material. This makes quasi-phase matching very useful in device construction. So techniques for inverting the layers needed developing and study.

Three methods of constructing quasi-phase matching (QPM) structures in GaAs were employed and studied by our team. The first is orientation patterned gallium arsenide (OP-GaAs). The second is optically contacted gallium arsenide. The third is diffusion bonded gallium arsenide (DB-GaAs).

OP-GaAs has the most promise as structures other than simple periodic plane parallel structures such as fanned out structures are possible with this crystal growth technique. These samples are constructed using standard vapor deposition growth techniques on a template constructed so as to form vertically growing regions that alternate in structure from their horizontal neighbors. The difficulty with this method is growing a sample of well defined structure for a sufficient surface area. currently the cross section limit along the vertical growth direction seen at Hanscomb air force base for this method is just above 7 mm. As a result of the sample being thin along one of the cross-sectional directions, the THz waves reflect, and scatter before being emitted from the outlet face of the sample limiting power production and beam quality.

OC-GaAs uses separate wafers carefully slid together with their orientations inverted between layers at the time of assembly followed by applying a steady downward pressure on the stack to drive out air and results in a surface tension bond between layers. The advantage here is when it is successful there are large cross-sectional areas of periodic inversion. The disadvantage of this technique is that impurities and surface irregularities lead to a limited number of layers one can successfully construct before there is no clear

aperture in the mid IR range through the sample.

Diffusion bonding is similar to optical contacting. After the layers are assembled (usually in deionized water) the sample is pressed inside a furnace so that the layers partially melt sticking together. This technique has a very low yield and is no longer employed. We had old samples available from when it was used at Stanford University and used them for comparison. The advantage here was that one of the samples turned out to be the best overall performer in the conversion efficiency experiments.

For these samples the conversion efficiency was studied using a well characterized focused optical beam of known pulse duration and wavelength to generate THz waves from the sample. The waves were collected using a 50 mm focal length picarin lens focusing them into a bolometer. The generated THz intensity was compared to the input intensity to calculate the optical to THz conversion efficiency.

Next, we needed the relationship between the QPM structures and the frequency of the generated THz waves. This was characterized using both a Michelson interferometer with a bolometer detector and also using a two color THz time domain spectrometer. The periodicity to THz frequency relationship was experimentally determined and was in good agreement with the theory.

Part II

Nonlinear Optical Properties of Gallium Arsenide

4 Theories of Multi-Photon Absorption and Nonlinear Refraction

4.1 The Parabolic Two-Band Theory of Direct Bandgap Material Multi-Photon Absorption

Understanding multi-photon absorption and nonlinear refraction are critical to designing devices using mid IR to generate THz waves. Without a good characterization the design limits for maximum intensity before effects such as optical pump beam attenuation from multi-photon absorption, THz wave absorption and lensing due to free carrier generation, or temporal pulse spreading due to self phase modulation in the optical pump pulse are unknown. As a result it is necessary to present the theory and experimental characterization of GaAs in the mid IR in the first section.

First, I will present the theory and then our results. The multi-photon absorption is the primary intensity limiting term and since optical to THz wave generation efficiency improves with intensity this will be presented first.

Then the design modifying parameter of nonlinear refraction will be presented. Since there are ways to compensate with certain limits of beam stability for effects such as nonlinear refraction and spectral broadening. By design of the system and of the optical components one can account for the increased refraction and spectral broadening. Techniques such as adjusting

optical focal length to account for additional refraction at the desired power level and mirror such as specially constructed 'chirped' dielectric mirrors can account for spectral broadening. Since once the nonlinear refraction is known it can be compensated for it is of secondary importance. It is still somewhat limiting as the stability of the input source sets design parameter limits one can achieve but these are more engineering limits and less intrinsic physical limits of the material. As a result I will present them second.

4.2 Introduction to Parabolic Direct bandgaps and Multiphoton Absorption

Understanding multi-photon absorption is critical for nonlinear optical devices such as infrared detectors, spin-flip Raman lasers, optically bistable semiconductor elements, THz sources and OPO's. It is also important to understand the transparency limitation of window materials. It can also be viewed as an initiation mechanism in optical surface damage of such devices. Our application is GaAs as a THz Source. Multiphoton absorption at a given wavelength limits the intensity and thus sets a conversion efficiency limit on THz production.

In this chapter, a simple model using parabolic direct gap bands will be discussed.[3] Appendix 1 presents the mathematical development of this theory in detail for those interested. In later chapters this model will be applied for specific cases and compared to the experimental results. This

two-band model gives reasonable agreement both with my experimental data and with previous data in the two photon absorption range by others. A more detailed model will be discussed in a later section on the concept of anisotropy.

Consider the case for N photon absorption where we can define an absorption coefficient, K_N. The rate of energy absorption for a unit volume of material we define as $K_N I^N$. If we then decide to define K_N in terms of the interband transition rate per unit volume of material associated with the simultaneous absorption of N photons, W_N, we have a relationship related to a quantum mechanical property this way. To connect the quantum mechanics of the system to the bulk theory consider when the unit volume contains one molecule. This leads us to our familiar transition rate from time dependent perturbation theory and we can apply the Fermi Golden Rule. Then we can write by following this procedure:

(1) $$K_N = W_N N \hbar \omega I^{-N}$$

The simplest model to use is a 2 parabolic band model. GaAs is a 'direct bandgap material. This means that in a plot of energy versus wave vector the conduction band energy minima is at the same k value as the valence band energy maxima. This is an important band structure for photonic devices. Since photons carry little momentum this is necessary for photonic

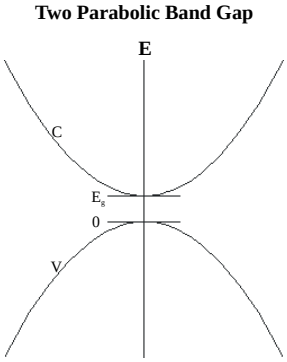

Figure 1: This energy versus wave vector graph diplays two parabolic bands.

transitions. This model is shown below in Figure 1. Note that the mass relationship between the upper and lower bands is $m_c = -m_v$.

To apply the Fermi golden rule we sum over all possible transitions between the valence and conduction bands and introduce the matrix element, $M_{cv}^{(N)}$, for the N-photon transition. So using the electron wave vector W_N can then be defined as:

$$(2) \quad W_N = \frac{2\pi}{\hbar} \sum |M_{cv}^{(N)}(\overrightarrow{k})|^2 \delta(E_{cv}(\overrightarrow{k}) - N\hbar\omega)$$

In standard perturbation fashion we define the single photon matrix as the perturbation Hamiltonian radiation/matter interaction matrix between the initial and final state associated with a single photon absorption. Then

to get the higher order absorption terms we perturb over intermediate states in standard fashion. So this appears first as:

$$(3) \quad M_{cv}^{(1)} = H'_{cv}$$

Next, we perturb to an intermediate state in the interaction picture this is done by summing across the product of an intermediate state with the same perturbation Hamiltonian only ending in the intermediate state multiplied by the perturbation Hamiltonian from the intermediate state to the final state and divide by the difference in energy between the intermediate state and the photon energy. This is the result one gets in the interaction picture and is found in many textbooks such as Shankar or Cohen and Tannouji.

$$(4) \quad M_{cv}^{(2)} = \sum_{a} \frac{H'_{ca} H'_{av}}{E_{av} - \hbar\omega}$$

One can follow the same iterative procedure and solve the general cases for even and odd N. This leads to general formula that are consistent with observation within an appropriately chosen scaling factor for a given N. To reach this solution one uses the $\overrightarrow{k} \cdot \overrightarrow{P}$ approach with the appropriate Kane parameter.

From here the derivation is shown in Appendix 1. For those interested I

go over the mathematical procedure in detail.

4.3 Theoretical Results

For the case of even numbered multiphoton absorption, the relationship is:

(5)

$$K_N = \sqrt{2}\pi^{N-1}2^{N-1}N^{4N}((N-1)!)^2\frac{f_{2N-2}}{f}(\frac{e^2}{\hbar c})^N\frac{P^{2N-3}\hbar^{N-1}}{n^N E_g^{4N-5}}\frac{(N\hbar\omega/E_g-1)^{3/2}}{(N\hbar\omega/E_g)^{4N-3}}$$

where f and f_{2N-2} are numerical factors calculated from standard definitions in the $\overrightarrow{k}\cdot\overrightarrow{P}$ model.

The important part for us is the frequency dependence. We shall examine whether the data supports this behavior.

In the case of odd numbered multiphoton absorption, a slightly different theoretical relationship is found. This relationship is:

(6)

$$K_N = \sqrt{2}\frac{\pi^{N-1}}{2^N}\frac{N^{4N-2}}{((\frac{N-1}{2})!)^4}\frac{f_{2N}}{f^3}(\frac{e^2}{\hbar c})^N\frac{P^{2N-3}}{n^N E_g^{4N-5}}\frac{(N\hbar\omega/E_g-1)^{1/2}}{(N\hbar\omega/E_g)^{4N-3}}$$

Note the frequency dependence in the numerator is different here. This frequency dependence difference in the exponent does not change the boundary conditions. This is as one expects. At the high frequency end one expects the lower number (N-1) multiphoton absorption to take place before the next

photon arrives and thus the multiphoton absorption should drop off. At the other end where the energy is no longer sufficient one also expects a drop off to zero at the lower limit. Both of these functions provide this fitting well with our physical intuition. The difference in dependence mainly results in a different tail behavior at the boundary to the next more energetic multiphoton absorption.

Of course, all of this is calculated with absolute zero temperature so one can expect that the limit end where it goes to zero actually has a thermal tail as well. This was consistent with our observations out to 1.8 μm as we saw higher than the predicted values in 3 photon absorption as can be seen later in the experimental presentation.

4.4 $\chi^{(3)}$ and $\chi^{(5)}$ effects in GaAs

Now, having a microscopic theory one needs some way to connect this result to a measurable result by some specific reproducible procedure in the laboratory. To do this a systematic approach to what will be observed with a gaussian beam in a simple transmission experiment is presented.

4.4.1 Two and Three Photon Absorption from Both First Principles Approach and the Macroscopic Approach: Connecting Theory to a Practical Measurement Approach

$\chi^{(3)}$ effects are very important for gallium arsenide. As GaAs is a direct bandgap material with a bandgap of 1.43 eV it absorbs photons promoting

free carriers directly for photons of equal or higher energy than this. So it is opaque to photons with energy greater than the bandgap.

Below the bandgap effects such as 2 photon absorption (2PA) and nonlinear refraction come into play. In the range from 870 nm to 1.74 μm two photon absorption is the dominant effect responsible for attenuation of pump signals at high intensity. Since THz generation is our primary interest and it goes as a function of intensity we want the highest intensity possible. It turns out that two photon absorption strongly limits the intensity throughput in GaAs hence the need to go beyond 1.74 μm outside the 2 photon absorption range.

Even still, another $\chi^{(3)}$ effect to consider is the nonlinear refraction which is proportional to the real part of $\chi^{(3)}$. Here I will give a treatment of both and in a later chapter show our results measuring 2 photon absorption compared to theory.

As seen in the previous section, there is a general formula for two photon absorption derivable from first principles in the microscopic regime. Inputting the numbers into the general formula gives

$$(7) \quad \beta = 2^9\sqrt{2}(\frac{e^2}{\hbar c})^2\frac{f_2}{f}\frac{\hbar P}{n^2E_g^3}\frac{(2\hbar\omega/E_g-1)^{3/2}}{(2\hbar\omega/E_g)^5}$$

Using a macroscopic approach we can find an expression relating the transmission to the intensity for a given wavelength. Such an approach gives

a method for measurement to compare to the microscopic theory. Since true infinite uniform plane waves don't exist, a gaussian average will be taken across the beam profile leading to important relationships we can compare. The relationship we will explore is between the peak intensity (I_0), the baseline linear transmission (T_0), and the measured actual transmission (T), due to multi-photon absorption through a sample of a given thickness (ℓ).

Additionally, simplifying the problem some is the use of femtosecond pulses so that transient effects[9] such as losses due to free carriers are minimized. This is because the optical pulse has exited the sample before the characteristic excitation time of the free carriers or other transient effects. This simplifies the differential equation to its simplest form of

$$\frac{dI}{dz} = -\alpha I - \beta I^2 - \gamma I^3 ... \tag{8}$$

For the case where 2PA is dominant with $\alpha \ll \beta I$ first solving the differential equation for a given intensity proceeds directly.

$$\frac{dI}{dz} = -\alpha I - \beta I^2 \simeq -\beta I^2 \tag{9a}$$

$$\frac{dI}{I^2} = -\beta dz \tag{9b}$$

Integrating both sides recognizing that when $z = 0$ then $I = I_0$.

$$(10)\quad \int_{I_0}^{I} \frac{dI'}{I'^2} = \int_0^{\ell} (-\beta) dz = -\beta\ell$$

$$(11)\quad \frac{1}{I} - \frac{1}{I_0} = \beta\ell$$

Rearranging and multiplying through by I_0 and recognizing $I/I_0 = T$

$$(12)\quad \frac{1}{T} = 1 + \beta\ell I_0$$

Now this is the transmission function at any point. We need the transmission function averaged over a gaussian beam. The transformation process for this is outlined conveniently in a paper by Kolodner, Kwok, Black, and Yablonovitch[10]. Using their results for $f(I) = IT$:

$$(13a)\ T = T_0 \frac{d\ln(\int_0^{I_0'} \frac{1}{1+\beta\ell I_0} dI)}{d\ln(I_0')}$$

$$(13b)\quad = \frac{T_0}{1+\beta\ell I_0}$$

The final result for 2PA in inverse transmission form is

$$\frac{1}{T} = \frac{1}{T_0}(1 + \beta \ell I_0) \tag{14}$$

This result is linear in intensity so finding the value of β becomes a simple transmission measurement matter. There are issues involving the effects of nonlinear refraction to consider though since this means the beam will be focusing inside the sample causing an overestimate with traditional transmission measurement techniques. Use of z-scan measurements minimizes this compared to standard transmission measurements.[11]

Similarly for the 3 photon absorption coefficient, γ, one can by the same process find the relationship for transmission.

$$\frac{dI}{dz} = -\alpha I - \gamma I^3 \simeq -\gamma I^3 \tag{15a}$$

$$\frac{dI}{I^3} = -\gamma dz \tag{15b}$$

$$\int_{I_0}^{I} \frac{dI'}{I'^3} = \int_0^{\ell} (-\gamma) dz = -\gamma \ell \tag{15c}$$

$$\frac{1}{I^2} - \frac{1}{I_0^2} = \gamma \ell \tag{15d}$$

$$\frac{1}{T^2} = 1 + \gamma \ell I_0^2 \tag{15e}$$

$$\frac{1}{T} = (1 + \gamma \ell I_0^2)^{1/2} \tag{15f}$$

Now we again use the transform to the gaussian beam

$$
\begin{aligned}
\text{(16a) } T &= T_0 \frac{d\ln(\int_0^{I_0'} \frac{1}{(1+\gamma\ell I_0^2)^{1/2}} dI)}{d\ln(I_0')} \\
\text{(16b)} &= \frac{T_0}{(1+\gamma\ell I_0^2)^{1/2}} \\
\text{(16c) } \frac{1}{T} &= \frac{1}{T_0}(1+\gamma\ell I_0^2)^{1/2}
\end{aligned}
$$

The 3PA result in the limit where $\gamma\ell I_0^2 \ll 1$ can be reduced using a Taylor expansion in typical fashion to the quadratic function

$$\text{(17)} \quad \frac{1}{T} = \frac{1}{T_0}(1+2\gamma\ell I_0^2)$$

This gives a method for distinguishing between 2PA and 3PA at low intensity. The 2PA is always linear and 3PA being quadratic at low intensity is easily distinguishable from it. In the high intensity limit 3PA is again linear making fitting a very practical matter for 3PA. This will come in handy later. The linearity of 2PA making the fitting procedure straightforward.

This gives a macroscopic way to connect to experiment. One measures several MPA coefficients calculated this way for a set of wavelengths in the appropriate wavelength range of the desired MPA theory to be tested. This gives a data point for each wavelength which can then be directly compared with the theoretical first principles result derived earlier.

The measurements needed to accomplish this are the average incident

power, the beam waist (w), The thickness of the sample, the average transmitted power through the sample, the low power (first order) transmission), and the pulse duration. Then using standard optical equations such as $I = I_0 e^{-\frac{2r^2}{w^2}}$, $P(r) = I_0 \int_0^r \int_0^{2\pi} e^{-\frac{2r'^2}{w^2}} r' dr' d\phi$, and $T = \frac{P_{throughput}}{P_{incident}}$ one can generate all the terms other than the absorption coefficient itself.

4.4.2 Nonlinear Refraction: n_2

General Approach In this field there is one landmark paper that I will follow along carefully in appendix 2. In the paper mentioned previously by Bahae, Hutchings, Hagan, and Van Stryland [12] the 2 parabolic bandgap model is carried to a more in-depth level by inclusion of Stark and Raman effects. The inclusion of Stark shifting and Raman scattering brings a more exact calculation that produces a wavelength dependent nonlinear refraction more in line with experimental observation.

Nonlinear refraction is predominantly the second order term such that one can write $n = n_0 + n_2 I$. we are interested in n_2. This is also often referred to as the Kerr effect. There are two types of this effect. If the material has a negative lensing ($n_2 \prec 0$) when the material reaches an absorption limit the intensity will suddenly rise and such a material is called a saturable absorber. The other effect is positive lensing ($n_2 \succ 0$) and this is generally what people refer to by Kerr lensing. This intensity dependent self focusing can lead to damage and in general changes the beam profile in an unstable manner that limits functional design in devices such as OPO's.

GaAs is self focusing and this is of critical importance in designing any optical system at high intensities. Suppose one were to design an OPO without including this effect, then the mirror optics would not focus at the correct point and all the path lengths would be incorrect. For high intensity OPO systems path length is very critical as the round trip time must be an integer multiple of the pump laser repetition period. One can not simply adjust the mirrors closer to find the appropriate distance. This distance is fixed at design time by the mirror choice and the repetition rate of the system.

There are two approaches one can use to calculate n_2. One approach uses the real component of $\chi^{(3)}$. The other approach uses a variational approach from the Kramers-Kronig relations. The K-K relation is in general a causal approach that implicitly uses $\chi^{(3)}$. The general integral form is:

$$(18) \quad n(\omega) - 1 = \frac{c}{\pi} \int_0^\infty \frac{\alpha(\omega')}{\omega'^2 - \omega^2} d\omega'$$

Introducing a perturbation[12], ξ, takes us directly to:

$$(19) \quad \Delta n(\omega) = \frac{c}{\pi} \int_0^\infty \frac{\Delta\alpha(\omega')}{\omega'^2 - \omega^2} d\omega'$$

Now we could plug in the change in β directly and this would be good until we were near the band edge. To get a more accurate measure across the entire

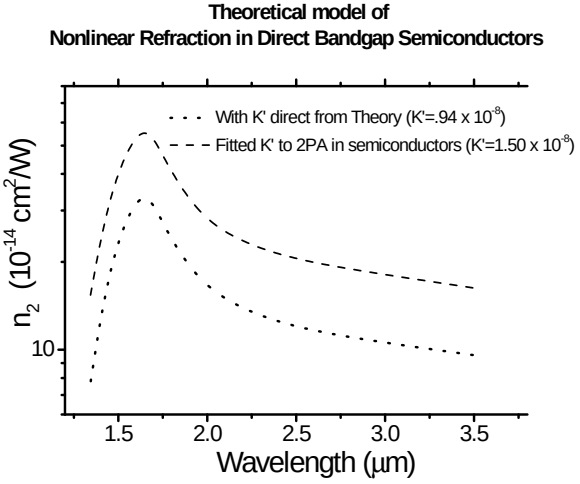

Figure 2: Figure 2: Theoretical model showing fitted and directly calculated nonlinear refraction in gallium arsenide.

desired spectral range an inclusion of other effects such as Raman Transitions, Linear AC Stark Effect, and Quadratic AC Stark effect are necessary as well. These are derived in explicit detail in appendix 2.

The computational method required to resolve the divergences in some of the terms results in a computational model that is not readily analytic. However some general properties can be described and are detailed in the figure below.

The expected peak near resonance is visible here in the 1.74 μm neighborhood. And as one would expect it drops as one approaches the direct absorption limit where the linear index of refraction diverges. In the low energy regime the tail drops gradually and is fairly constant over the 3PA

range. All of this fits our physical intuition. Since n_2 is a $\chi^{(3)}$ effect we would expect it to peak around the wavelength corresponding to half the bandgap. Similarly, as one goes off this resonance one would expect it to drop. The slow rate of this drop at longer wavelengths can be seen as due to Raman scattering and the linear Stark effect contributions.

4.4.3

Anisotropy in GaAs Anisotropy is crucially important to understand as the orientation of the GaAs in the beam to optimally produce THz waves is easily calculable as will be shown in the THz generation section. To calculate the multi-photon absorption and nonlinear refraction in a given configuration correctly one must take anisotropy into account. This is especially important for the refraction when designing the optical components in a type 2 DFG system as the two optical pump pulses have different polarization orientations with regard to the GaAs. As a result the self phase modulation, spectral broadening and beam distortion are different for the two different overlapped pulses.

Multiphoton Absorption Anisotropy $\bar{4}$3m group has 2 fold and four-fold symmetry. In terms of rotation a tensor has a rotation of $e^{i\theta}$[13] for each tensor axis. This means that for $\chi^{(2)}$ with only 3 axes the maximum symmetry that it can present is 3 fold. For $\chi^{(3)}$ the full four-fold symmetry is demonstrable. In terms of what this means let us suppose that there is

anisotropy in the axes of GaAs, then a rotation function about any axis can have symmetry of the form $x = x_0 + x_2 \cos(2\theta + \theta_0) + x_4 \cos(4\theta + \theta_0)$. This is in fact what is seen[14][15].

Numerous authors have done various attempts at theorizing the 2PA anisotropy[14][16]-[18]. Analysis of the bulk behavior and bulk theory have been done on GaAs for 2PA showing both data and theory supporting my previous paragraph.[14][17]

Several detailed first principles approaches have been attempted [16][18]. In 1990 one paper outlines two different approaches to direct band structure calculations for the anisotropy in $\chi^{(3)}$ for GaAs[16]. The empirical tight-binding band structure technique was the dominant focus of this paper and produced similar but not too useful results to the other more primitive method. In defense of this technique it must be stated that it did work rather successfully on numerous materials for $\chi^{(2)}$. The other technique called semi-ab initio band structure gave unremarkable results as well here. A plus to this method is that it gave zero frequency calculations that made physical sense for the first time and to some degree corresponded with real world measurements for several materials such as silicon.

Continuing to refine their approach to multiphoton absorption, Hutchings and Wherrett went to a seven band model[18] using the higher conduction band set contributions to calculate the linear versus circular polarized 2PA anisotropy as well. "Theory of Anisotropy of two-photon absorption in zinc-blend semiconductors" is the current reference paper used extensively when

discussing 2PA anisotropy in GaAs.

In the symmetry group $\bar{4}$3m $\chi^{(3)}$ has only 21 nonzero elements of which only 4 are independent.[18][19] The four independent elements are χ_{xxxx}, χ_{xxyy}, χ_{xyxy}, χ_{xyyx}. When there is only one frequency involved then this reduces to 3 independent elements as then $\chi_{xyxy} = \chi_{xyyx}$.[18] For compactness in writing one can define $\chi^{"}_{xxxx} = Im(\chi^{(3)}_{xxxx})$. Then three parameters defined allows us to describe the anisotropy in 2PA. Those three parameters are the strength of the absorption, $\chi^{"}_{xxxx}$, the anisotropy, σ, and the dichroism, δ. For the latter two the definitions are:[18]

$$\text{(20a)}\ \sigma = \frac{\chi^{"}_{xxxx} - \chi^{"}_{xxyy} - 2\chi^{"}_{xyxy}}{\chi^{"}_{xxxx}}$$

$$\text{(20b)}\ \delta = \frac{\chi^{"}_{xxxx} + \chi^{"}_{xxyy} - 2\chi^{"}_{xyxy}}{2\chi^{"}_{xxxx}}$$

With these the 2PA coefficient can be written to describe either its anisotropy with respect to linear or circular polarization. In the linear polarization case the angles refer to the angle the electric field makes with a crystal axis in spherical coordinates about that axis. In the circularly polarized case the standard propagation definition given earlier in this paper with respect to the z crystal axis is used. The results of which are below. [18]

$$\text{(21a)}\ \beta^L(\theta,\phi) = \beta^L[0,0,1](1-\sigma\frac{\sin^2(2\theta)+\sin^4(\theta)\sin^2(2\phi)}{2})$$

$$\text{(21b)}\ \beta^C(\theta,\phi) = \beta^L[0,0,1](1-\delta-\sigma\frac{\sin^2(2\theta)+\sin^4(\theta)\sin^2(2\phi)}{8})$$

The linear coefficient can be rewritten once ϕ is recognized to be $\frac{\pi}{4}$ and that θ in the spherical coordinates about the z axis is the same as the rotation angle in the plane normal to the direction of propagation. One needs to keep track of whether the rotation is clockwise or counterclockwise as well. Then, after rearrangement the linear 2PA coefficient becomes:

$$\text{(22)}\qquad \beta^L[1,1,0](\theta) = \beta^L[0,0,1](1-\frac{11}{32}\sigma)+\frac{1}{8}\sigma\beta^L[0,0,1]\cos(2\theta)$$

$$\text{(23)}\qquad +\frac{7}{32}\sigma\beta^L[0,0,1]\cos(4\theta)$$

Notice this has the expected form where $\beta_0 = \beta^L[0,0,1](1-\frac{11}{32}\sigma)$, $\beta_2 = \frac{1}{8}\sigma\beta^L[0,0,1]$, and $\beta_4 = \frac{7}{32}\sigma\beta^L[0,0,1]$. Obeying the symmetry considerations discussed earlier. However others with a very good data fit for 2PA had by a macroscopic approach come to a similar but slightly different relationship that still obeyed the symmetry conditions at the beginning of this section.[13]-[15]

The other relationship begins similarly in appearance but one notices immediately that instead of subtracting both forms of rotation from the 2PA

for [0,0,1] this relationship adds the 4th order and subtracts the 2nd order. It should be noted that σ was found to be the same in both approaches.

$$(24)\quad \beta^L[1,1,0](\theta) = \beta^L[0,0,1](1 + 2\sigma(\frac{3}{4}\sin^4(\theta) - \sin^2(\theta))$$

After rearranging this one becomes:

$$(25)\qquad \beta^L[1,1,0](\theta) = \beta^L[0,0,1](1 - \frac{7}{16}\sigma) + \frac{1}{4}\sigma\beta^L[0,0,1]\cos(2\theta) + \frac{3}{16}\sigma\beta^L[0,0,1]\cos(4\theta)$$

This raises questions about the anisotropy theory so popularly quoted. The data fit the latter approach better. Both have a very similar appearance as would be expected. This latter approach actually shows a larger maximum anisotropy than the microscopic theoretical model.

Anisotropy in n_2 First, the principle authors in this area wrote a paper using a 4 band Kane model.[20] This theory provided considerably better results on dispersion relations in nonlinear refraction and even lead to some correspondence with dispersion in NLR for AlGaAs in the 1.5 to1.7 μm wavelength range. The four band Kane model was a vast improvement. It still had shortcomings in that it was isotropic for NLR purposes. There was no predicted anisotropy.

Again, D.C Hutchings and B. S Werrett wrote the paper of note here. And again they used the seven band model.[21] Their prediction gives the anisotropy that we should observe to have the same angular dependence at a given wavelength. In the two photon range their calculated values for GaAs were a little larger than experiment has shown but close enough to be considered within reason.[18] As their results were an extremely good fit for Al_xGa_{1-x}. [21][22] However it should be noted that in the 3PA range our data showed significantly smaller anisotropy than the predicted amount of ~50%.

$\chi^{(5)}$ Three Photon Absorption and anisotropy Three photon absorption is given by the equation derived earlier for 2PA in a zincblende crystal. The anisotropy is expected and found to have the same form as in two photon absorption. This is expected as the $\bar{4}$3m group has no additional symmetries to resolve. Since there are no additional symmetries one can expect the final form to have the same general structure without intensive calculations. The scope of this paper is experimental and so rather than derive from scratch a more exacting theoretical model the author will present results and show the fit to the general theoretical model.

5 Experimental Measurement of Multi-photon Absorption and Nonlinear Refraction

5.1 Standard Transmission Measurement

The standard transmission measurement is shown in Figure 3. The mid IR beam passes through the variable attenuator through a beam splitter to a CaF_2 lens that focuses the beam. The sample is placed at a position just in front of the focal plane at a spot well characterized by knife-edge measurement. The split off beam is sent to a pyroelectric detector and the detector output is used as the input reference to an oscilloscope controlled by a computer using a two channel software written by Konstantin Vodopyanov. The transmitted beam though the sample is collected at another pyroelectric detector and sent to the other channel on the oscilloscope as the signal.

During data collection the software collects time averaged data at regular intervals. To get transmission versus intensity profile data one just slowly adjusts the variable attenuator during the time between collection of each data point. Generally, this is done by starting with the beam blocked to give 10 data points showing the no signal value of the detector output. Then the beam is unblocked at high intensity and dialed down gradually until the level is back to detector threshold minimum value. The software is then stopped and the data saved to a file. The set up was constructed by Yun-Shik Lee

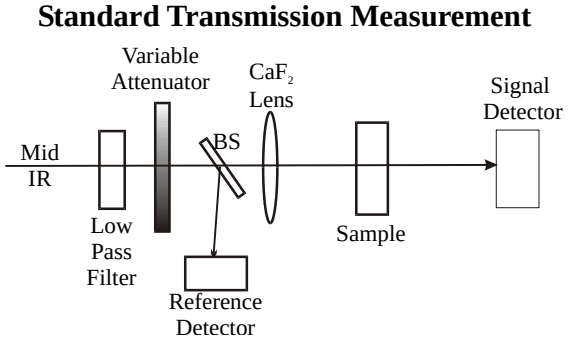

Figure 3: The mid IR beam is filtered and attenuated. In this experiment the attenuator is changed in small increments throughtout the experiment to provide different incident intensities on the sample. The transmitted throughput mid IR is measured by the signal detector.

and the author. The data was collected by Bryan Norton and the author.

After the data is collected, a Molectron J-9 energy meter is placed first along the signal path to measure the input energy per pulse versus the reference detector signal so that a linear fit can be done of averaged power to detector signal. Then with the sample removed the signal detector measurement is compared to the molectron measurement and a linear fit of the detected power to detected signal can be done as well.

It is necessary to take spectral measurements with the monochromator and pulse duration measurements with the autocorrelator here as well. They are described in appendix 3.

To convert the data into an usable form is merely a matter of converting from the detector voltage recorded to the appropriate power using the fits done with the calibrated Molectron detector versus data acquiring pyroelec-

tric detector data. From there using knife-edge measurements of the beam profile at the sample location and the pulse duration one can calculate the input intensity (See appendix 3 for a description of these procedures). Comparison of the input power and the transmitted power gives the transmission.

Since the linear transmission is well known[20], the transmission relations derived in the theory section can now be used to find out the order of nonlinear transmission at the wavelength the experiment was performed at. Further, the appropriate absorption coefficient can be estimated by fitting with the previous mentioned relationships reproduced below.

$$\frac{1}{T} = \frac{1}{T_0}(1 + \beta \ell I_0) \tag{26}$$

$$\frac{1}{T} = \frac{1}{T_0}(1 + \gamma \ell I_0^2)^{1/2} \tag{27}$$

In Figure 4 are some selected data sets taken at 4 different wavelengths. One can readily see the wavelengths expected to be 3PA are quadratic at low power as expected distinguishing them from the 2PA linear behavior.

Data analysis was provided by Yun-Shik Lee for this experiment.

The standard transmission experiment was an important step. We determined several useful facts from this data. One, by distinguishing the shapes of the transmission curves one can see the difference between two and three

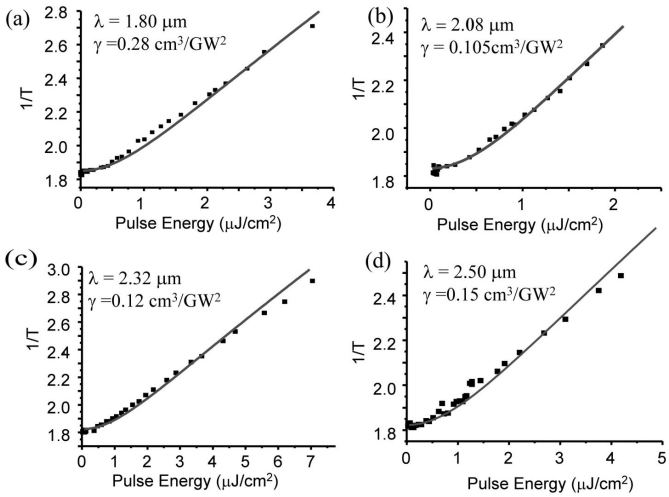

Figure 4: The solid squares are data. The solid line represents the fit using the 3PA coefficient listed. (a) Transmission measurement just above the two photon absorption edge. (b) The fit is better in the middle of the 3PA zone. Note this wavelength is near an absorption minimum making 2.08 μm the preferred wavelength to work in the 3PA range. (c) By 2.32 μm, the coefficient is increasing again. (d) Approaching the 3PA band edge at 2.5 μm and the 3PA coefficient is still larger than at 2.08 μm

photon absorption showing which case we had at a given wavelength. Two, around 2.1 μm there is a local minimum in the three photon absorption making it an interesting wavelength for optical design purposes. This experiment established that we were indeed looking at the wavelength regime of three photon absorption. We obtained general values which were within a factor of 3 of what we determined with the more precise technique we used next.

Now, the next experiment to do are open and closed aperture z-scans. These would generate more refined data. Z-scans also would measure nonlinear refraction at the same time as the now demonstrated to be of correct order appropriate multi-photon absorption.

5.2 Z-Scans

5.2.1 Introduction

The z-scan is a powerful tool in that it gives both absorption and nonlinear refraction data with a minimization on overestimation due to self focusing[11]. This technique allows measurement of these properties using only one beam unlike pump/probe methods. When the pulse duration is very short free carrier generation contributions become negligent.

The basic idea of the open aperture z-scan is shown in Figure 5. A beam is first split so that a reference can measure the time averaged incident power then the beam is focused using a lens. The sample is moved along the path of the beam symmetrically about the focal plane. The beam is focused onto

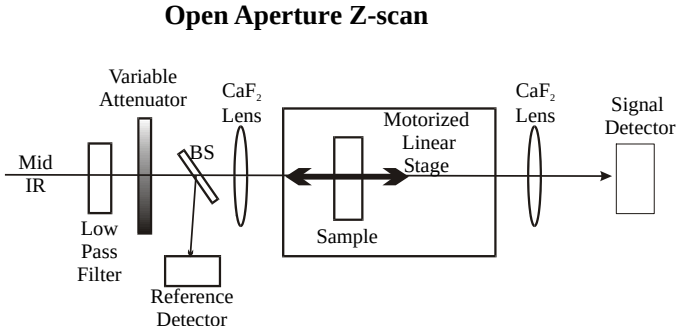

Figure 5: Different from the standard transmission experiment in that the attenuator is only adjusted prior to the experiment to get the desired transmission dip of between 5 and 10 %, The open aperture z-scan setup above uses movement of the sample along the beam path to obtain different incident intensities.

a detector with a second lens. So as the sample moves closer to the focal plane the intensity increases and the transmission will drop due to increased multiphoton absorption.

With a well characterized beam the exact intensity profile can be established for all the positions the sample moved through establishing an intensity versus transmission data set. Again, one needs to characterize the pulse width and center wavelength using a autocorrelator and a monochromator. Also the detectors need power calibration as described in the transmission experiment. This experiment differs from the transmission experiment in that an entire length of beam must be characterized for intensity but the incident power remains constant and that the sample is moved.

In the open aperture z-scan it is important to collect the entire transmitted beam. So a CaF_2 lens is used to collect the throughput and focus it onto

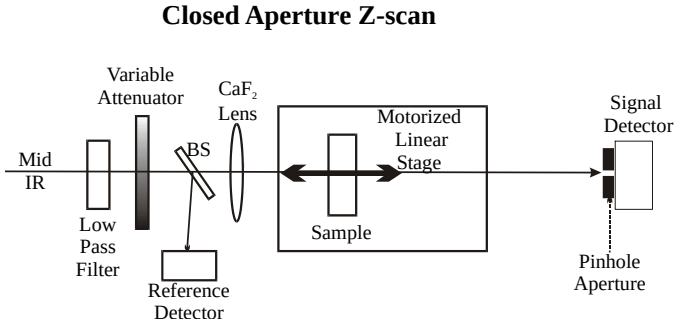

Figure 6: Now the lens to the detector is removed and a pinhole placed immediately in front of the detector.

the detector.

The closed aperture z-scan is very similar to the open aperture z-scan except the signal detector that measures the transmission no longer has a lens focusing all the beam onto it and instead has a pinhole centered on the beam so that only the central intensity is measured. This is illustrated in Figure 6.

This setup can measure the nonlinear refraction. However, to be accurate one needs both the open and closed aperture scans so the effects of absorption can be divided out.[23] In the case of positive n_2, when the sample is nearer the lens than the focal plane it focuses the beam even more tightly so the focal plane with the sample is nearer the lens and farther from the detector. This increased length to the detector from the original focal plane means the beam will be larger in diameter at the detector due to increased divergence so the intensity will drop. When the sample is further than the focal plane of the lens then the n_2 effect is to reduce the divergence of the beam and

thus increase the intensity. If the sign of n_2 is negative these are reversed. One can immediately look at a z-scan and know whether one has positive or negative lensing by where the peak and valley are relative to the focal plane without a sample.

5.2.2 The Theory Behind the Z-Scan Measurement

Nonlinear Refraction with Linear Absorption For this case, define nonlinear refraction and the incident wave as follows.

$$
\begin{aligned}
\text{(28a)} \quad n &= n_0 + n_2 I(z,r,t) \\
\text{(28b)} \quad E(z,r,t) &= E_0(t)\frac{w_0}{w(z)} e^{-\frac{r^2}{w^2(z)} - \frac{ikr^2}{2R(z)}} e^{-i\phi(z,t)} \\
\text{(28c)} \quad w^2(z) &= w_0^2\left(1 + \frac{z^2}{z_0^2}\right) \\
\text{(28d)} \quad z_0 &= \frac{kw_0^2}{2} \\
\text{(28e)} \quad R(z) &= z\left(1 + \frac{z_0^2}{z^2}\right) \\
\text{(28f)} \quad I(z,r,t) &= \frac{\epsilon_0 c}{2}\left|E(z,r,t)\right|^2
\end{aligned}
$$

Here the origin is taken to be at the focal plane in the center of the beam. This is a standard gaussian beam representation.[24][25]

For thin samples where the thickness, L, of the sample is smaller than z_0 then in the slowly varying envelope approximation (embedded in the E_0 term) the beam diameter changes within the sample due to diffraction and

nonlinear refraction are small. So to low order one can refer to this as the "external self-action" case[23].

Of interest is the change in phase, $\Delta\phi$, generated by passing through the thin sample. Two simple coupled differential equations govern this. One is the change in phase with position along the propagation axis in the sample, $z\prime$, and the other is the intensity change along the propagation axis in the sample. The latter being most familiar. The former is related to the induced change in the wave front by the nonlinear refraction.

$$\frac{d\Delta\phi}{dz'} = \Delta n(I)k \tag{29}$$

$$\frac{dI}{dz'} = -\alpha I \tag{30}$$

The latter equation of course having the well known simple solution. The former is a little more subtle. This is the slowly varying envelope approximation and a similar derivation will be done in the THz generation and detection section. Rather than working through this tedious differential equation I will present the results obtained in the principle reference [23] for this section.

$$(31)\quad \Delta\phi(z,r,t) = \frac{kn_2 I(0,0,t)}{1+\frac{z^2}{z_0^2}} \frac{1-e^{-\alpha L}}{\alpha} e^{-\frac{2r^2}{w^2(z)}}$$

For brevity later I will follow the main reference[23] practice of defining a piece that is radially independent here.

$$(32)\quad \Delta\phi_0(z,t) = \frac{kn_2 I(0,0,t)}{1+\frac{z^2}{z_0^2}} \frac{1-e^{-\alpha L}}{\alpha}$$

and

$$(33)\quad \Delta\phi_0 = kn_2 I(0,0,t) \frac{1-e^{-\alpha L}}{\alpha}$$

Using the result for the intensity and this result for the phase distortion we can write the electric field after the sample, $E_e(z,r,t)$, in terms of the unperturbed field with no sample, $E(z,r,t)$.

$$(34)\quad E_e(z,r,t) = E(z,r,t) e^{-\frac{\alpha L}{2}} e^{i\Delta\phi(z,r,t)}$$

Here we have an exponential in an exponent so we need some way to sim-

plify this and the standard technique is to Taylor expand this and the result will be a sum of gaussian waves of different order. This is called gaussian decomposition. If one simply decomposes the $e^{i\Delta\phi(z,r,t)}$ term it becomes:

$$(35)\quad e^{i\Delta\phi(z,r,t)} = \sum_{m=0}^{\infty} \frac{(\Delta\phi_0(z,t)e^{-\frac{r^2}{w^2(z)}})^m}{m!} = \sum_{m=0}^{\infty} \frac{(\Delta\phi_0(z,t))^m}{m!} e^{-\frac{mr^2}{w^2(z)}}$$

If one includes the original beam curvature this gets more messy but is still practical to do. It gives the added advantage that now each gaussian can be propagated to a detector through an aperture and summed up. The field as seen at the aperture at a distance, d, from the sample can be described more compactly using the following definitions.

$$(36a)\quad g = 1 + \frac{d}{R(z)}$$

$$(36b)\quad w_{m0}^2 = \frac{w^2(z)}{2m+1}$$

$$(36c)\quad d_m = k\frac{w_{m0}^2}{2}$$

$$(36d)\quad w_m^2 = w_{m0}^2(g^2 + \frac{d^2}{d_m^2})$$

$$(36e)\quad R_m = \frac{d}{1 - \frac{g}{g^2 + \frac{d^2}{d_m^2}}}$$

$$(36f)\quad \theta_m = \tan^{-1}(\frac{d}{d_m g})$$

Then the electric field at the aperture is given:

$$(37)\quad E_a(r,t) = E(z,0,t)e^{-\frac{\alpha L}{2}}\sum_{m=0}^{\infty}\frac{(i\Delta\phi_0(z,t))^m}{m!}\frac{w_{m0}}{w_m}e^{-\frac{r^2}{w_m^2}-\frac{ikr^2}{2R_m}+i\theta_m}$$

It appears odd when one notices the z dependence still in several of the terms. However, when the fact that the sample position can change so d is actually a variable and z is the distance from the free space focal plane to the sample is considered then it makes sense to still see z mentioned. The distance from the sample to the detector must be far enough to be in the far field so $d \gg z_0$.

In detection through an aperture the amount of power incident on the detector without a sample would be the total power through the aperture where w_a is the beam waist without the sample at the aperture and r_a is the aperture size. This is given below. In the equation below z is still the distance from the focal plane to the detector.

$$\begin{aligned}
(38a)\ P(t) &= 2\pi\int_0^r I(z,r',t)rdr \\
(38b) &= \frac{\pi w_0^2 I_0(t)}{2w_a^2}\int_0^{r_a} e^{-\frac{2r^2}{w_a^2}}d(2r^2) \\
(38c) &= \frac{\pi w_0^2 I_0(t)}{2}(1-e^{-\frac{2r_a^2}{w_a^2}})
\end{aligned}$$

We can define the effects of the aperture with a new term called S, the aperture parameter. S is then given by $S = 1 - e^{-\frac{2r_a^2}{w_a^2}}$. This will be a very important parameter for the measurement of nonlinear refraction. For compactness we can also define the total incident power without a sample $P_i(t) = \frac{\pi w_0^2 I_0(t)}{2}$

With the sample the phase distortion comes into play and then the transmitted power would be:

$$\text{(39a) } P_T(t) = 2\pi \int_0^r I(z, r', t) r' dr'$$

$$\text{(39b) } = \frac{\pi \epsilon_0 c}{n_0} \int_0^{r_a} |E_a(r, t)|^2 \, r dr$$

Then the time averaged transmission can be calculated from the ratio of the time integrals for the two power functions. Z here is the distance between sample and free space focal plane again.

$$\text{(40) } T(z) = \frac{\int_{-\infty}^{\infty} P_T(t) dt}{S \int_{-\infty}^{\infty} P_i(t) dt}$$

It has been found by extensive numerical analysis[23] that only a few terms of the gaussian decomposition of the aperture field need to be calculated to get a high accuracy. Additionally, the distance between peak and valley along z has been found to be $\Delta z_{p-v} \simeq 1.7 z_0$. Even more the change

in transmission between peak and valley for vary small values of S has been found to be $\Delta T_{p-v} \simeq .406\,|\Delta\phi_0|$. For larger aperture parameters still smaller than 1 analysis revealed $\Delta T_{p-v} \simeq .406(1-S)^{.25}\,|\Delta\phi_0|$ when $|\Delta\phi_0| \leq \pi$. These results however describe the CW case. For a gaussian pulse a factor of $\sqrt{2}$ is multiplied by the time averaged value to get the instantaneous value of the nonlinear refraction, n_2.

Nonlinear Refraction and 2PA In this case both effects are $\chi^{(3)}$ effects and so since they are of the same order one can expect the mixture to show in the closed aperture case obscuring the change in transmission from peak to valley. However, as mentioned previously, one can divide out the absorption and recover the nonlinear refraction.[23] To understand why this is true consider the case where 2PA is dominant so $\beta I > \alpha$. Then our intensity differential equation becomes:

$$\frac{dI}{dz} = -(\alpha I + \beta I^2) \tag{41}$$

The solution is substantially more tedious than the last one. A new parameter that make the solution easier to follow is q. Let's define $q(z,r,t) = \beta I(z,r,t)\frac{1-e^{-\alpha L}}{\alpha}$. Here z is again the sample position relative to the free space focal plane. Then the solutions are:

$$(42a)\quad I_e(z,r,t) = \frac{I(z,r,t)e^{-\alpha L}}{1+q(z,r,t)}$$

$$(42b)\ \Delta\phi(z,r,t) = \frac{kn_2}{\beta}\ln(1+q(z,r,t))$$

$$(42c)\quad E_e(z,r,t) = E(z,r,t)e^{-\frac{\alpha L}{2}}(1+q)^{i\frac{kn_2}{\beta}-\frac{1}{2}}$$

At this point if one follows the exact same procedures as in the linear absorption case a very similar result is obtained. In fact, to go from the linear case to the 2PA case the propagated electric field only needs the modification:

$$(43)\quad \frac{(i\Delta\phi_0(z,t))^m}{m!} \rightarrow \frac{(i\Delta\phi_0(z,t))^m}{m!}\prod_{n=0}^{m}(1+i(2n-1)\frac{\beta}{2kn_2})$$

One needs the m=0 case to still be 1. Clearly the same procedure could be used from there if one simply knew β. Then it could be inserted into the power calculation and n_2 found by fitting. In fact, the primary reference [23] did just this first. Then by numerical analysis it was determined that with 10 % uncertainty one can get the same results if $\frac{\beta I_0(t)}{1+\frac{z^2}{z_0^2}}\frac{1-e^{-\alpha L}}{\alpha}$ and $\frac{\beta}{2kn_2}$ are both less than 1 by just dividing the closed scan by the open scan and then fitting with the linear absorption case. This is clearly the advantage of the need for a low number of terms in the gaussian decomposition. It makes practical measurement simpler.

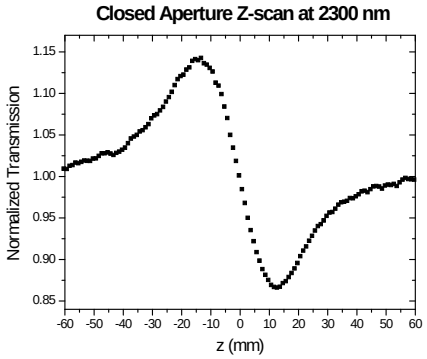

Figure 7: The symmetric shape of this scan shows the dominance of nonlinear refraction over 3PA. The positive z direction is taken to be towards the lens in this example. This is positive lensing.

Higher Order MPA Since for M>2 these are higher order susceptibility terms than for n_2 the dominant term is the nonlinear absorption. The closed aperture z-scans show little influence from the absorption as seen in Figure 7. And even if they did the absorption term being less significant makes the division of the closed aperture scan by the open even more accurate. The harder trick here is the calculation of the absorption coefficient and even that can be simplified by arranging the data by inverse transmission versus intensity and using the approach outlined for transmission measurements. This is even advantageous as the z-scan significantly better estimates the absorption without overestimation than a standard transmission experiment[11].

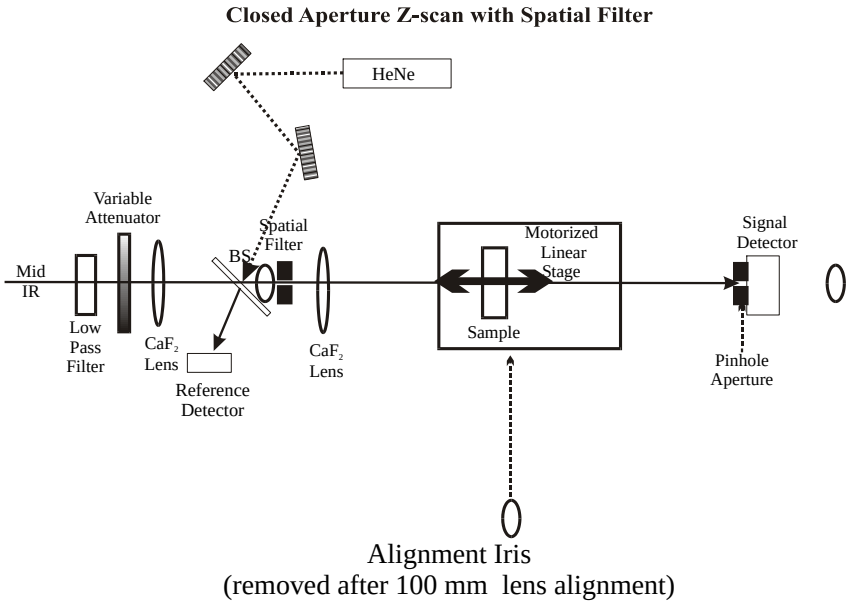

Figure 8: Shown here is the modified closed aperture z-scan. The modifications are the same for the open aperture z-scan. The earlier simplified diagram is modified by the insertion of a spatial filter at the focal plane and addition of an alignment beam.

5.2.3 Detailed Experimental Setup

In this experiment a HeNe alignment beam is a must. Alignment, careful beam profiling and laser stabilization are crucial to getting reasonable data. This experiment is very sensitive to power fluctuations and beam deformation. As beam deformation is a real issue here and the OPA is a serious source of said deformation, a spatial filter must be used. The setup is shown in Figure 8.

The beam was first sent through a 2.5 micron low pass filter to remove the visible light that accompanies the beam out of the OPA and then attenuated

at a variable attenuator to achieve the desired transmission dip at the focal plane in the z-scan.

The location of the 200 mm focal length lens for the spatial filter and the location of the beam splitter were planned carefully and the beam splitter was placed before setting the two alignment irises. This was important so that the beam path can be set parallel to the motorized linear stage very precisely. Setting up such a system one wants to use two very separated irises when doing the initial alignment of the two beams. (HeNe and mid IR) They were set very far apart (greater than the anticipated length of the setup) and the two beams aligned. It is best to set the beam splitter in the beam path at the desired angle (as near orthogonal as one can and still pick up the split off signal close by) before aligning the beams and irises so that the lateral dislocation of the beam path takes place before the irises.

The beam was focused using a 200mm CaF_2 lens. Shortly after the lens, a beam splitter was introduced to allow measurement of the incident power while also allowing the alignment of a HeNe laser beam. After the beam splitter an aperture was placed. It was found to be easiest to get a quality alignment if one placed this iris just after where the anticipated location of the spatial filter would be so that the beams didn't diverge too large making accurate placement of the spatial filter problematic. An additional iris is placed close to the anticipated focal plane in the z-scan. A third iris is placed beyond the intended detector location giving the needed distance for a precise alignment. a detector is temporarily placed just after the last iris

and both the HeNe visible beam and the mid IR beam are aligned through these three irises.

Then the near iris was removed and a 100 or 50 μm high power pinhole aperture from Thorlabs was placed at the focal plane using a linear stage to adjust along the propagation direction and a two axis adjustable fixture to align the beam orthogonal to the propagation direction. The HeNe beam was used to get close to the focal plane by observing its' focal plane on a white card but there was some need for further alignment. The two beams are never perfectly overlapped and when adjusting to within microns distance on a focused beam the error becomes apparent. The mid IR beam was blocked at first and alignment performed with just the HeNe beam through the spatial filter. Once the HeNe beam was centered through the spatial filter a power meter with a large aperture (the Molectron J-9) was placed immediately after the spatial filter. The mid IR beam was unblocked and the power maximized first with the 2 axis mount. The power level was recorded and the spatial filter position moved 1mm along the beam path to one side or the other. Maximization was performed again and compared to the original level. If the power increased the procedure was repeated in the same direction. If it dropped then I went back the other way and investigated the other direction. I found the focal plane within 100 microns for these experiments.

When done sufficiently accurate one still has an alignment beam at this point. This is particularly useful for aligning the samples orthogonal to the beam by reflection later. And it makes the next lens placement and alignment

much easier.

The beam diverges very rapidly from the spatial filter. Generally, to get the entire beam without clipping in a 1" lens one has to use a 100 mm focal length CaF_2 lens at this point. The closer to the spatial filter (Outside of the 100 mm) the lens is placed the farther away the focal plane will be by geometric optics. The neighborhood of 11 to 13 cm has worked sufficiently in the past.

Next one uses a thermal sensitive plastic card to find the focal plane for the IR beam. The beam was blocked before the lenses then and the motorized stage placed offset to one side of the beam path far enough to allow for mounting the sample. A 3 position stage was then mounted on the motorized stage to give precision control to sample placement.

A pyroelectric detector was placed 15 cm past the expected end of travel of the sample. Another 100 mm focal length CaF_2 lens was used to point the mid IR beam onto the detector so that the measured signal is maximized. I had to move around the propagation direction some to find this point as too close to focus saturates an area of detector and too far and the beam is not completely on the detector.

Detector characterization comparing the power measured with the Molectron just after the lens for the z-scan zone and the two detectors at various power settings was done next. Using the method described in the transmission measurement section the reference detector was calibrated first. Then using the same software and technique with the Molectron removed the ref-

erence was used to calibrate the signal detector. Alternatively passing the Molectron in and out at various power levels had been tried. Small fluctuations in the power during the two measurements made this method less accurate.

Next, the sample was placed in a holder and appropriately mounted to the 3 position stage mounted on the motorized track so that the sample was centered in the beam with the beam at normal incidence. This was accomplished using the HeNe beam. The mid IR beam was blocked by the OPA or at least before the beam splitter. Then the lights were turned out and a thin piece of paper was used to find the beam just in front of the sample. The paper was passed to the sides of the HeNe beam to find the reflection as well. Once the reflection was found the sample position and angles were adjusted until the reflection from the sample overlapped the incoming HeNe beam. The optical part of the system was complete at this point.

The motorized track was connected to the ESP300 stage controller. The signal detector was connected to the lock-in amplifier. The 1KHz trigger from the Legend SDG control box was connected to both the lock-in amplifier and an oscilloscope as the trigger. The reference was connected to the oscilloscope. Oscilloscope, lock-in amplifier, and ESP300 stage controller were all connected to the data acquisition computer system by GPIB cables. In the past, either THz.vi or pp.vi were used to collect data and run the motorized stage. These software did not collect the reference and so the reference had to be closely watched to make sure that the data run was performed with

power fluctuations of no greater than 1%. In the future, new software thanks to Jeremy Danielson will collect the data complete with the reference.

The incident power was measured next with the Molectron after the lens while obtaining the reference level at the same time. Immediately before the data was collected and again immediately after the open aperture run.

Once the open aperture data was collected, the lens that steers the beam onto the signal detector was removed and an iris added using a flexible fastening material. The iris was carefully centered on the beam and the iris was closed down almost all the way shut. If it was closed too far interference fringes began to dominate the data. So the author found that about double the diameter of a 1/2" iris at maximum close was about correct for good shaping of the peak and valley. (~2 mm)

Monitoring the incident power for fluctuations during the closed aperture data run was also performed. Data with runs that stayed within 1% of incident power level were required. Open aperture dips were best in the 8% transmission dip neighborhood. Greater than 10 % was found to increase error.

A Razor blade mounted as a knife edge was carefully placed to mark the stage zero position of the sample front face.

Next, the sample was removed and a knife edge placed on a 1" motorized stage attached in place of the sample. Measurements were performed at selected positions on the propagation axis to characterize the beam profile both vertically and horizontally. Additionally, the center wavelength of the

optical pulse was measured using a monochromator. Last, the pulse duration was measured. These procedures are described in appendix 3.

Data on this experiment was primarily collected by the author with some help from Bryan Norton, Naaman Amer, Jeremy Danielson, and Yun-Shik Lee. Analysis of the beam profile was done by the author and Yun-Shik Lee. Further data analysis was done by Yun-Shik Lee and Konstantin Vodopyanov.

5.2.4 Z-scans: Multiphoton Absorption and Nonlinear refraction in GaAs

Intrinsic GaAs (semi-insulating gallium arsenide) is a direct bandgap material with a direct gap of 1.43 eV at room temperature (300 K). The wavelength corresponding to this energy is 870 nm. At or below this GaAs is opaque. Above 870 nm to 1.74 μm is the two photon absorption region. Above 1.74 μm to 2.61 μm is the 3PA region. In general, 870 nm $\times$(M-1) to 870 nm $\times$ M is the zone for MPA.

Using the z-scan setup described in detail earlier we characterized GaAs at selected wavelengths from 1.2 μm to 2.5 μm. With the addition of a DFG system we also characterized at 3.5 and 4.4 μm. The samples were from AXT. The samples were 350 μm thick 2" wafers with the (1,1,0) direction being out of the face. The polarization was along the z crystal axis for the MPA experiments other than the anisotropy experiment at 2 μm

Two selected wavelengths showing the raw data are given in Figure 9.

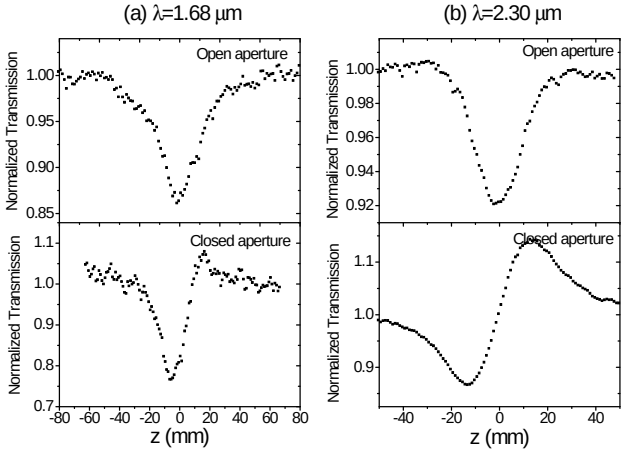

Figure 9: Normalized transmission data of open- and closed-aperture Z-scan measurements (a) at 1.68 μm and (b) 2.30 μm

One immediately notices the marked difference between a 2PA closed aperture scan and a 3PA closed aperture scan. In the 2PA case the absorption dominates the nonlinear refraction as they are both $\chi^{(3)}$ effects. Where in the 3PA case the absorption effects are negligent compared to n_2. Also easily noticed is the pronounced shape indicating positive n_2. This is all to be expected as 1.68 μm is within the 2PA range and 2.30 μm is well into the 3PA range.

Once the intensity is calculated using the knife edge measurements, the power conversions for the detectors, and the pulse duration the data can be converted into inverse transmission versus intensity plots and fit to give the appropriate multiphoton coefficients using the equations derived before. Recalling them:

$$(44)\quad \frac{1}{T} = \frac{1}{T_0}(1 + \beta \ell I_0)$$

$$(45a)\quad \frac{1}{T} = \frac{1}{T_0}(1 + \gamma \ell I_0^2)^{1/2}$$

$$(45b)\quad \simeq \frac{1}{T_0}(1 + 2\gamma \ell I_0^2)$$

Selected data are shown in Figure 10. The 1.68 μm data shows its linear nature clearly in good agreement with the theoretical expectations. The fit value is consistent with ~3 cm/GW found previously[26]. The 3PA quadratic behavior at low intensity is clearly visible in the 2.30 μm data as is the linearity of the same data at high intensity again confirming the 3PA theory and providing a data point that is consistent with theory. The 3.47 μm data does not fit either 4 or 5PA and as it is within 10 nm of the boundary between the two it is not surprising it is some mixture of the two combined. This is similar to results I observed near 1.75 μm

After fitting the various curves and extracting the appropriate MPA coefficients all of this is compared to the theories derived earlier from the two parabolic band model. The agreement is good for this kind of measurement as typical experimental error is on the order of 200 % for this type of experiment. [23] This data is in Figure 11.

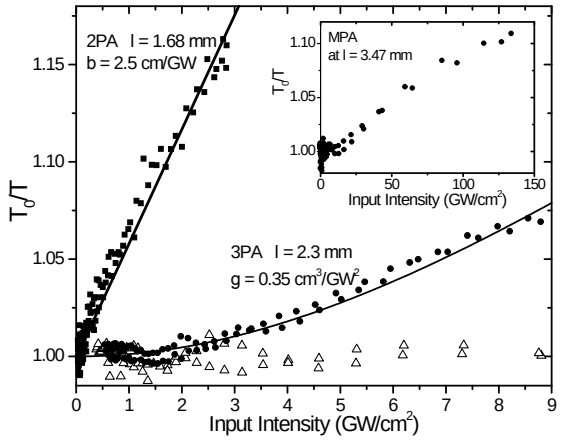

Figure 10: Experimental data and theoretical curves of best fit (solid line) for normalized nonlinear transmission inverse ($\mathbf{T}_0/T$) vs input intensity ($\mathbf{GW/cm^2}$) at 1.68 μm (solid squares), 2.30 μm (solid circles), and 3.47 μm (open triangles). Inset shows nonlinear transmission curve for 3.47 μm at much higher intensities.

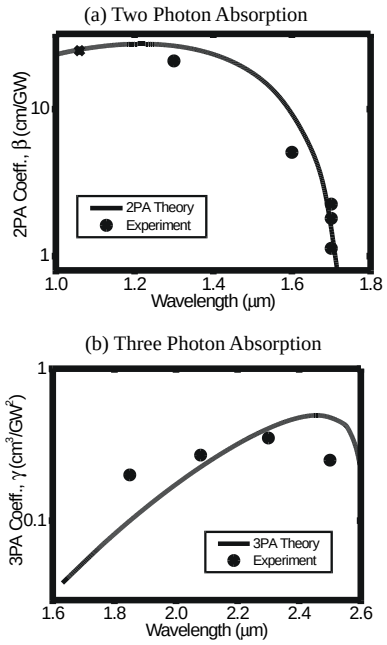

Figure 11: Experimental data and theoretical curves of (a) 2PA and (b) 3PA coefficients vs. Wavelength.

Near the 3PA to 2PA band edge the theory doesn't take into account the 2PA tail effects so the increase in that neighborhood is in line with expectations as one would expect some hybrid mix of 2PA and 3PA to be taking place in that neighborhood at room temperature. It would be interesting to see if this vanishes as one approaches absolute zero.

Since 3PA is a $\chi^{(5)}$ effect it should be able to resolve both the 2 and 4 fold symmetry of the zincblende structure of GaAs. Figure 12 shows the fit to data taken by rotating the GaAs sample while maintaining the beam power level and polarization. by measuring the change in dip in an open aperture z-scan the anisotropy in 3PA was resolved and fit well to the phenomenological function for this crystal symmetry. Given the phenomenological equation $\gamma(\theta) = a + b\sin(2\theta) + c\sin(4\theta)$ one finds that for $a = .22cm^3/GW^2$, $b = -.021cm^3/GW^2$, and $c = -.020cm^3/GW^2$ fits well to the anisotropy data confirming the essential expected anisotropy.

Next, using the equation for the small aperture case in the closed aperture z-scan the nonlinear refraction was found. for the difference between peak and valley normalized transmittance, ΔT, recall:

$$\Delta T = .406 \times \frac{2\pi \ell n_2 I}{\lambda} \tag{46}$$

where ℓ is the distance along the z axis between the two, λ is the free space wave vector, and I is the intensity. Using the theoretical model with a fitted

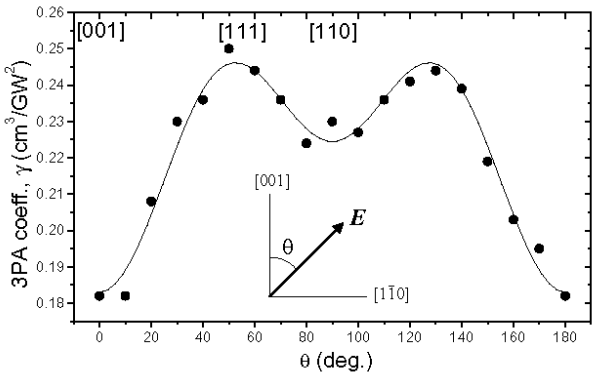

Figure 12: Experimental data (solid-circle0 and numerical fit (solid-line) of the 3PA coefficient at 2 μm as a function of the angle θ between the optical polarization and the [0,0,1] axis.

constant of .86 $\times 10^{-8}$ developed by Bahae et al. [12] in the 2 parabolic band model presented earlier a good fit between theory and experiment is seen for the dispersion in n_2. However, as can be seen in Figure 13 the anisotropy is much smaller than expected by the theoretical model. It does however, obey the general behavior of the crystal class.

clearly the prediction of $n_2([1,1,0])/n_2([0,0,1]) \approx 2$ is not supported by this data. However the general dispersion fits well to the model developed earlier for dispersion n n_2 using the 2 parabolic bands with both Stark effects and Raman effects accounted for.

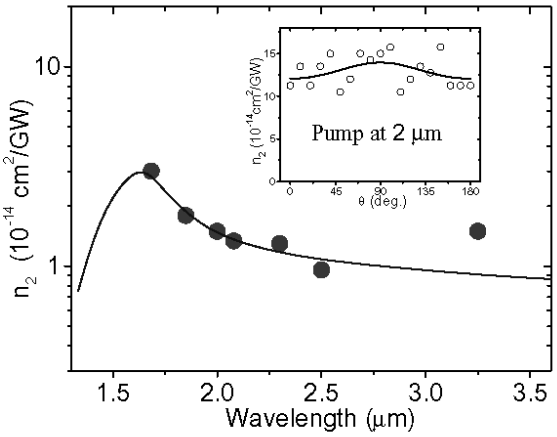

Figure 13: Experimental data and theoretical curve from [12]. (solid line) of nonlinear refractive index, n_2, vs. wavelength (polarization along [1,1,0]). Inset shows results of n_s anisotorpy measurement.

Part III

Terahertz Pulse Generation and Detection in Gallium Arsenide

The principle mission of this research was to collect the basic physical properties of GaAs necessary to design a THz generating OPO at Stanford University. The first stage on mid IR properties having been completed in the previous section prepares the way for the next stage necessary in development.

Next, the appropriate information relevant to THz wave generation from the mid IR pump beam is needed. Typically this is done using either optical rectification or difference frequency generation both of which are $\chi^{(2)}$ effects. Since both are second order nonlinear effects the scope of the THz wave generation and detection section will begin there. The nature of $\chi^{(2)}$ for the $\bar{4}$3m crystal class which GaAs belongs to is examined in detail. The optimal angle for THz generation using optical rectification is calculated which is also the optimal angle for detection via the electro-optic effect.

THz wave generation and the optical to THz conversion efficiency are examined. This is done using a bolometer on various samples with different quasi-phase matched structures made using different approaches.

The next consideration is to verify the behavior of quasi-phase matched structures. This is done using a two color terahertz time domain system. It uses a mid infrared pump on the GaAs samples and detects with a near infrared probe beam and a standard zinc telluride detection crystal. The center frequency of the resultant multi-cycle pulses and the bandwidth are then calculated.

6 The Theory of Optical Rectification and

Electro-Optic Sampling

It is important to note that optical rectification (OR), electro-optic effect and difference frequency generation (DFG) are all second order nonlinear ($\chi^{(2)}$) effects. Mathematically, this can be seen by extending the typical first order terms presented in electromagnetism text books such as Jackson's and collecting terms of the same order as demonstrated below.

$$\text{(47a)} \quad \overrightarrow{P} = \chi \overrightarrow{E}$$

$$\text{(47b)} \quad \overrightarrow{P} = \overrightarrow{P}^{(1)} + \overrightarrow{P}^{(2)} + \overrightarrow{P}^{(3)} ... = \chi_i^{(1)} \overrightarrow{E} + \chi_{ij}^{(2)} \overrightarrow{E}\,\overrightarrow{E} + \chi_{ijk}^{(3)} \overrightarrow{E}\,\overrightarrow{E}\,\overrightarrow{E} ...$$

$$\text{(47c)} \quad \overrightarrow{P}^{(1)} = \chi_i^{(1)} \overrightarrow{E},\ \overrightarrow{P}^{(2)} = \chi_{ij}^{(2)} \overrightarrow{E}\,\overrightarrow{E},\ \overrightarrow{P}^{(3)} = \chi_{ijk}^{(3)} \overrightarrow{E}\,\overrightarrow{E}\,\overrightarrow{E}, ...$$

One can readily see that the even order susceptibility tensors will always result in the same polarization regardless of sign for the electric field in a single beam. This means there is an asymmetry in the crystal polarizability. Such an asymmetry means that only noncentrosymmetric crystals can be used for optical rectification, electro-optic effect, sum frequency generation, difference frequency generation and second harmonic generation.

Thus we will need to study noncentrosymmetric crystals for our desired application. A careful, in depth approach to the second order susceptibility tensor, $\chi^{(2)}$, will be necessary as well. To really understand what causes this behavior one must study the unit cell of a given crystal and this brings in the quantum mechanical properties.

Understanding these quantum properties and the microscopic behavior such as density of states and band structure allows the calculation of the macroscopic properties from first principles while adding in the frequency dependence that is not inherently obvious in the general bulk material equations.

Both GaAs and ZnTe have a zincblende structure ($\overline{4}$3m). ZnTe has been used for broadband THz generation and detection for many years now.[27]

Crystals have additional symmetry properties arising from a type of symmetry condition known as Kleinman symmetry. This allows us to simplify the susceptibility tensor from rank 3 to rank 2 with 3 by 6 elements instead of the $3 \times 3 \times 3$ elements of the original susceptibility tensor. In general, this is how the macroscopic analysis is done and this new tensor is usually called d_{il}.

Further simplification can be done by considering a narrow beam incident on the crystal from some direction in the crystal coordinate system with the angle of incidence specified in spherical coordinates for the $\overrightarrow{k}$ of the incident beam to give the angles θ and ϕ. Then by specifying the electric field in terms of the previously defined angles one can calculate the magnitude of the polarization as an angular function times the electric field magnitude squared. A new term called d-effective (d_{eff}) is constructed from the terms in the polarization excluding the electric field magnitude squared. This is done by grouping together the previously mentioned terms to make a new angle-dependent variable. The electric field components are contracted into

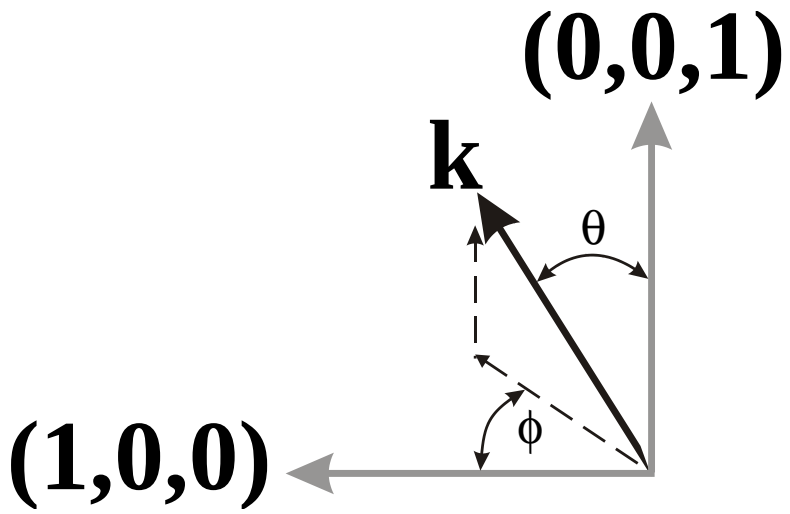

Figure 14: $\overrightarrow{k}$ is given in standard spherical coordinates with reference to the crystal coordinate system.

a 6 dimensional vector as well. . The angles are shown above in Figure 14. The contraction is shown below.

(48) $\overrightarrow{P}^{(2)} = \chi_{ij}^{(2)} \overrightarrow{E} \overrightarrow{E}$

Let

$$(49)\quad \overrightarrow{E}\,\overrightarrow{E} \rightarrow \begin{bmatrix} E_x(\omega_1)E_x(\omega_2) \\ E_y(\omega_1)E_y(\omega_2) \\ E_z(\omega_1)E_z(\omega_2) \\ E_y(\omega_1)E_z(\omega_2) + E_z(\omega_1)E_y(\omega_2) \\ E_x(\omega_1)E_z(\omega_2) + E_z(\omega_1)E_x(\omega_2) \\ E_x(\omega_1)E_y(\omega_2) + E_y(\omega_1)E_x(\omega_2) \end{bmatrix}$$

Then

$$(50)\quad \overrightarrow{P}^{(2)} = 2d_{il}\,\overrightarrow{E}\,\overrightarrow{E}$$

Next consider $\left|\overrightarrow{P}^{(2)}\right|$ for a single beam and rearrange to get d_{eff}.

$$(51a)\ P^{(2)} = 2\left|d_{il}\,\overrightarrow{E}\,\overrightarrow{E}\right|$$

$$(51b)\qquad = 2d_{eff}\left|\overrightarrow{E}\right|^2$$

I will define d_{eff} in terms of possible orientation directions of the electric field using an angle variable about the k axis (from the z axis for my particular chosen orientation) in my streamlined approach to deriving the angle

dependence as seen in the lab frame of reference.

6.1 Angular dependence of $\chi^{(2)}$ in ZincBlende Structures

6.2 Contraction to Second Rank

Members of the $\overline{4}$3m group such as zincblendes like ZnTe and GaAs have only 1 independent element in the second order susceptibility. The $\chi^{(2)}$ tensor can be contracted because of Kleinman symmetry (A symmetry that arises when the optical waves are much lower than the systems' lowest resonant frequency or if both frequencies interacting are identical) and the symmetries associated with a cubic crystal structure to a 3 by 6 contracted tensor, $d_{i\ell}$, where $\ell \in \{1, 2, 3, 4, 5, 6\}$ and the following table describes the appropriate elements from the jk contraction.[27]

jk	11	22	33	23,32	31,13	12,21
ℓ	1	2	3	4	5	6

Then we can by explicit use of the Kleinman condition write the nonlinear susceptibility tensor into the form:

$$(52) \quad d_{i\ell} = \begin{bmatrix} d_{11} & d_{12} & d_{13} & d_{14} & d_{15} & d_{16} \\ d_{16} & d_{22} & d_{23} & d_{24} & d_{14} & d_{12} \\ d_{15} & d_{24} & d_{33} & d_{23} & d_{13} & d_{14} \end{bmatrix}$$

In this form the electric field components can be rewritten to give a new form for the polarization such that $E(\omega_1)E(\omega_2)$ now has the form:

$$(53)\quad E(\omega_1)E(\omega_2) = \begin{bmatrix} E_x(\omega_1)E_x(\omega_2) \\ E_y(\omega_1)E_y(\omega_2) \\ E_z(\omega_1)E_z(\omega_2) \\ E_y(\omega_1)E_z(\omega_2) + E_z(\omega_1)E_y(\omega_2) \\ E_x(\omega_1)E_z(\omega_2) + E_z(\omega_1)E_x(\omega_2) \\ E_x(\omega_1)E_y(\omega_2) + E_y(\omega_1)E_x(\omega_2) \end{bmatrix}$$

Then the equation becomes

$$(54)\quad P_i(\omega_3) = 4d_{i\ell}E(\omega_1)E(\omega_2)$$

6.2.1 Angular Dependence Calculation

For the $\bar{4}$3m class the cubic crystal lattice symmetries simplify the situation even further as the only element that is nonzero is the d_{14} element. Then, because of cubic symmetry, the susceptibility tensor looks like:

$$(55)\quad d_{i\ell} = \begin{bmatrix} 0 & 0 & 0 & d_{14} & 0 & 0 \\ 0 & 0 & 0 & 0 & d_{14} & 0 \\ 0 & 0 & 0 & 0 & 0 & d_{14} \end{bmatrix}$$

When an optical signal is incident on a member of this crystal class from the (110) direction the generated signal is proportional to$(\sin^2(2\theta)+\sin^4(\theta))$. (Where θ is the angle of rotation about the optic axis) This can be shown by starting with the optic signal in standard (laboratory) coordinates and rotating to the crystal coordinates. In this case, the z axis of the optical signal is along the crystal (-1 -1 0) axis and the optical x axis is parallel to the crystal z axis. We choose the optical x axis to be along the crystal z axis so that this rotation can be thought of as two rotations; first a rotation of z to x about the y axis and then a 45 degree rotation about the z axis. The first rotation is 90 degrees about the y axis and can be written as:

$$(56)\quad R_1 = \begin{bmatrix} \cos(\theta) & 0 & -\sin(\theta) \\ 0 & 1 & 0 \\ \sin(\theta) & 0 & \cos(\theta) \end{bmatrix} = \begin{bmatrix} 0 & 0 & 1 \\ 0 & 1 & 0 \\ -1 & 0 & 0 \end{bmatrix}$$

Next, a 45 degree rotation about the z axis will complete the transformation.

$$(57)\quad R_2 = \begin{bmatrix} \cos(\theta) & \sin(\theta) & 0 \\ -\sin(\theta) & \cos(\theta) & 0 \\ 0 & 0 & 1 \end{bmatrix} = \begin{bmatrix} \frac{1}{\sqrt{2}} & -\frac{1}{\sqrt{2}} & 0 \\ \frac{1}{\sqrt{2}} & \frac{1}{\sqrt{2}} & 0 \\ 0 & 0 & 1 \end{bmatrix}$$

This transformation is shown in Figure 15

The product of these two rotations is the rotation directly from the optical coordinates to the crystal coordinates. This rotation is given below:

$$(58a)\ R = \begin{bmatrix} \frac{1}{\sqrt{2}} & -\frac{1}{\sqrt{2}} & 0 \\ \frac{1}{\sqrt{2}} & \frac{1}{\sqrt{2}} & 0 \\ 0 & 0 & 1 \end{bmatrix} \begin{bmatrix} 0 & 0 & 1 \\ 0 & 1 & 0 \\ -1 & 0 & 0 \end{bmatrix}$$

$$(58b) = \begin{bmatrix} 0 & -\frac{1}{\sqrt{2}} & \frac{1}{\sqrt{2}} \\ 0 & \frac{1}{\sqrt{2}} & \frac{1}{\sqrt{2}} \\ -1 & 0 & 0 \end{bmatrix}$$

A quick check here shows:

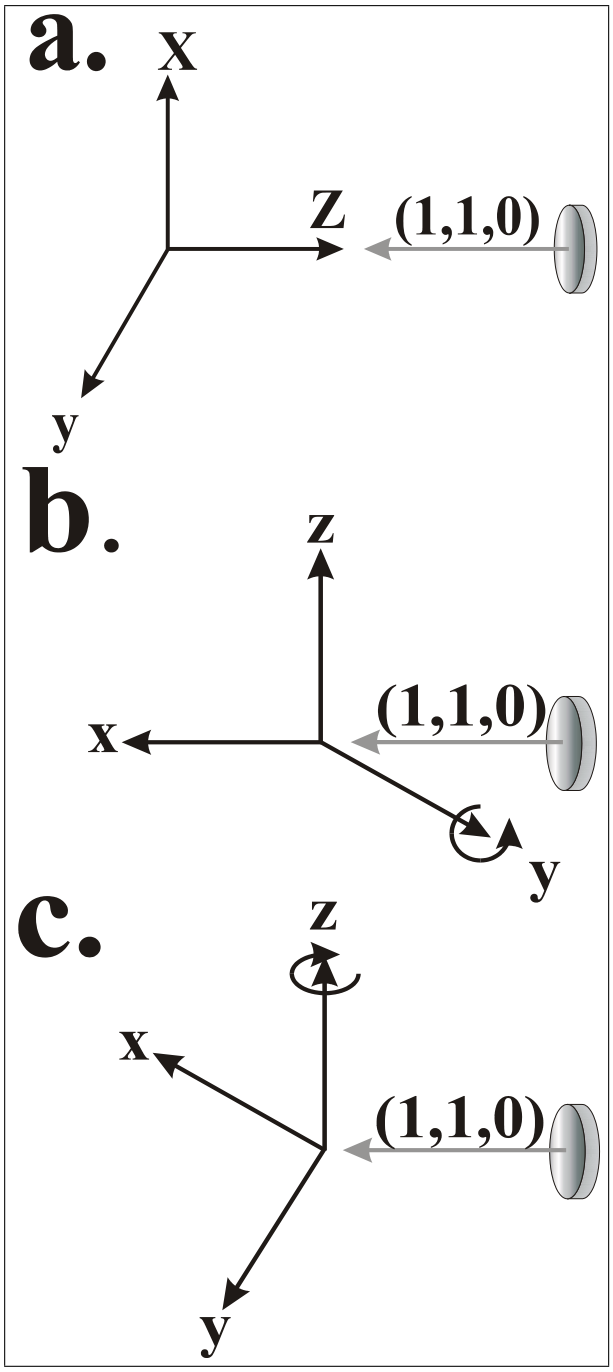

Figure 15: Rotation from optical reference frame to crystal reference frame. a. Initial reference frames for an optical beam along the (1,1,0) crystal direction. b. 90 degree counterclockwise rotation about the y axis aligning the z optic axis to the crystal z axis. c. 45 degree clockwise rotation about the z axis to complete the transformation.

$$(59a)\ R.\widehat{z} = \begin{bmatrix} 0 & -\frac{1}{\sqrt{2}} & \frac{1}{\sqrt{2}} \\ 0 & \frac{1}{\sqrt{2}} & \frac{1}{\sqrt{2}} \\ -1 & 0 & 0 \end{bmatrix} . \begin{bmatrix} 0 \\ 0 \\ 1 \end{bmatrix}$$

$$(59b) = \frac{1}{\sqrt{2}} \begin{bmatrix} 1 \\ 1 \\ 0 \end{bmatrix}$$

Verifying that the z optic axis is rotated into the crystal [1,1,0] axis as expected.

Now we rotate the electric field (which is of course built of components perpendicular to the z optical propagation axis) to the crystal coordinate system:

$$(60)\quad R. \begin{bmatrix} E_0 \cos(\theta) \\ E_0 \sin(\theta) \\ 0 \end{bmatrix} = \begin{bmatrix} -\frac{E_0 \sin(\theta)}{\sqrt{2}} \\ \frac{E_0 \sin(\theta)}{\sqrt{2}} \\ -E_0 \cos(\theta) \end{bmatrix}$$

θ is defined as the rotation about the z optic axis with the x optic axis as the standard reference (Standard cylindrical coordinates).

Now the $\overrightarrow{E}\overrightarrow{E}$ component looks like:

$$(61)\quad \overrightarrow{E}\overrightarrow{E} = \begin{bmatrix} \frac{E_0^2 \sin^2(\theta)}{2} \\ \frac{E_0^2 \sin^2(\theta)}{2} \\ E_0^2 \cos^2(\theta) \\ -\frac{E_0^2 \sin(2\theta)}{\sqrt{2}} \\ \frac{E_0^2 \sin(2\theta)}{\sqrt{2}} \\ -E_0^2 \sin^2(\theta) \end{bmatrix}$$

For a single input frequency only the bottom 3 terms are relevant. The top three are included for completeness.

Now solving for the second order polarization one obtains by simply contracting the two tensors:

$$\overrightarrow{P} = 4E_0^2 d_{14} \begin{bmatrix} -\frac{\sin(2\theta)}{\sqrt{2}} \\ \frac{\sin(2\theta)}{\sqrt{2}} \\ -\sin^2(\theta) \end{bmatrix}$$

The magnitude of $\overrightarrow{P}$ ($|P|$) gives us the induced electric field (via the wave equation) and the intensity is proportional to the square of this. Solving for $|P|$ gives us the measurable angle dependence.

(62) $|P| = 4E_0^2 d_{14}(\sin^2(2\theta) + \sin^4(\theta))$

This result is very useful. Not only does it apply to GaAs in optical rectification or electro-optic detection, it applies to all zincblende materials such as ZnTe which we used as a detector in the THz time domain spectroscopy system. For THz Time Domain Spectroscopy (THz-TDS) on GaAs we used THz generation from GaAs by a Mid-IR beam with a 800 nm probe beam and ZnTe to generate our ellipticity that is measured to give $\overrightarrow{E}_{THz}(t)$. With minor modification ($E_0^2 \rightarrow E_0(\omega_1)E_0(\omega_2)$) this result applies to below bandgap type 1 difference frequency generation (DFG), and below half bandgap input type 1 second harmonic generation (SHG). Type 1 DFG and SHG refers to the cases where the input photons have their polarizations parallel.[19]

The magnitude of the induced second order polarization is given as an angular function above. Using the equation for a propagating wave in matter this gives us a direct way to calculate the induced terahertz electric field. There are two ways to think of this. One, is to consider that the resonant frequency of the nonlinear polarizability of a given thickness of the material results in a down conversion of very closely related frequencies in a passing optical wave packet (Frequency domain approach). The other way to think of it is the temporal envelope of the optical pulse induces an electric field as it passes through the crystal that is related to the intensity of the optic pulse,

the thickness of the crystal and the second derivative of the time dependence of the optical envelope. More will be said about these relationships in a later section from this (The time domain) point of view.

6.2.2 THz Generation via Optical Rectification

Starting with Maxwell's equations in a medium we can derive a relationship useful in calculating the amplitude of the generated THz wave. This is done in the standard manner used to derive the wave equation. First, in the SI system:

$$\text{(63a)} \quad \nabla \cdot \overrightarrow{D} = \rho$$

$$\text{(63b)} \quad \nabla \cdot \overrightarrow{H} = 0$$

$$\text{(63c)} \quad \nabla \times \overrightarrow{E} = -\mu \frac{\partial \overrightarrow{H}}{\partial t}$$

$$\text{(63d)} \quad \nabla \times \overrightarrow{H} = \overrightarrow{J} + \frac{\partial \overrightarrow{D}}{\partial t}$$

Then taking the curl of the curl of the electric field in standard fashion:

$$\text{(64)} \quad \nabla \times (\nabla \times \overrightarrow{E}) = -\mu_0 \nabla \times \frac{\partial \overrightarrow{H}}{\partial t}$$

Rearranging the order of derivation:

$$(65)\quad \nabla \times (\nabla \times \overrightarrow{E}) = -\mu_0 \frac{\partial}{\partial t}(\nabla \times \overrightarrow{H})$$

Now substituting in standard fashion:

$$(66)\quad \nabla \times (\nabla \times \overrightarrow{E}) = -\mu_0 \frac{\partial}{\partial t}(\overrightarrow{J} + \frac{\partial \overrightarrow{D}}{\partial t})$$

Next, consider there are no free charges so $\overrightarrow{J} = 0$

$$(67)\quad \nabla \times (\nabla \times \overrightarrow{E}) = -\mu_0 \frac{\partial^2 \overrightarrow{D}}{\partial t^2}$$

Using the well known formula for curl of a curl:

$$(68)\quad \nabla(\nabla \cdot \overrightarrow{E}) - \nabla^2 \overrightarrow{E} = -\mu_0 \frac{\partial^2 \overrightarrow{D}}{\partial t^2}$$

and again because there are no free charges the divergence of the electric field is zero

$$(69)\quad \nabla^2 \overrightarrow{E} = \mu_0 \frac{\partial^2 \overrightarrow{D}}{\partial t^2}$$

Now using the definition for the D field:

$$(70)\quad \nabla^2\overrightarrow{E} = \mu_0\frac{\partial^2}{\partial t^2}(\epsilon_0\overrightarrow{E} + \overrightarrow{P})$$

rearranging and converting our constants as necessary:

$$(71)\quad \nabla^2\overrightarrow{E} - \frac{1}{c^2}\frac{\partial^2\overrightarrow{E}}{\partial t^2} = \frac{1}{\epsilon_0 c^2}\frac{\partial^2\overrightarrow{P}}{\partial t^2}$$

Using the definition of the polarization in general (not to first order) this can be rewritten. Also, as we are working with GaAs, a $\bar{4}$3m point symmetry group member, and it is isotropic in first order[28] for the mid IR range we can split off the first order polarization term to form the classic 1st order D field and then the rest of the polarization can be thought of as the source term.

$$(72)\quad \overrightarrow{P} = \overrightarrow{P}^{(1)} + \overrightarrow{P}^{(NL)}$$

$$(73)\quad \nabla^2\overrightarrow{E} - \frac{1}{\epsilon_0 c^2}\frac{\partial^2\overrightarrow{D}^{(1)}}{\partial t^2} = \frac{1}{\epsilon_0 c^2}\frac{\partial^2\overrightarrow{P}^{(NL)}}{\partial t^2}$$

This tells us some very useful information. Essentially you have the wave equation on one side and the nonlinear polarization on the other. And the generated wave is proportional to the second time derivative of the nonlinear polarization. For the optical rectification case where the frequency produced is many orders of magnitude lower than the generating optical frequency the pulse envelope becomes the time scale of significance. And since it is a second derivative this factor is nonlinear. So shorter pulse duration generates a larger THz signal.[29]

There has been a steadily increasing complexity of theoretical models from this point on. One model in 1992 using no absorption or pump depletion gave the general shape solving using the Fourier transformation of this equation.[30] Next, The wide band single cycle pulse behavior was explained using the Fourier transformed nonlinear polarization averaged across the relevant spectral range and showed the THz electric field was proportional to this averaged polarization.[31] More recently using the Fourier transformed version of the equation and the previous results regarding the nonlinear polarization Faure, Tilborg, Kaindl, and Leemans[28] wrote a more general solution in the frequency domain including the absorption of the THz by the crystal during propagation however there is a more general form that is in the final model I will use here[27].

The last theoretical model[27], being very close to the immediately previous model, will be the focus of this section. Assuming the generated wave is planar or close enough to ignore non-planar effects (Such as one finds near

the focal plane) then $\nabla^2 \rightarrow \frac{\partial^2}{\partial z^2}$.

$$(74) \quad \frac{\partial^2 \overrightarrow{E}}{\partial z^2} - \frac{1}{\epsilon_0 c^2} \frac{\partial^2 \overrightarrow{D}^{(1)}}{\partial t^2} = \frac{1}{\epsilon_0 c^2} \frac{\partial^2 \overrightarrow{P}^{(NL)}}{\partial t^2}$$

We only need the second order nonlinear polarization for our case and the derivative its of the intensity envelope. Assuming this derivative can be approximated by $-\omega^2 I(t)$ where $I(t)$ is the intensity envelope function we have a viable expression for the frequency dependent part. We still need the position dependent part of the polarization. Since the polarization is generated by the optical pulse and only starts once the optical pulse enters the crystal then using $\Theta(z)$, the Heaviside step function, and the angle vector for the direction of the electric field, $\widehat{e}$, we can define $\overrightarrow{P}^{(NL)}$.

$$(75) \quad \overrightarrow{P}^{(NL)}(z,t) = \epsilon_0 e^{ikn_{opt}z} \Theta(z) I(t) \chi^{(2)} \widehat{e}\widehat{e}$$

Substitution and the approximation modifies the equation to:

$$(76) \quad \frac{\partial^2 \overrightarrow{E}}{\partial z^2} - \frac{1}{\epsilon_0 c^2} \frac{\partial^2 \overrightarrow{D}^{(1)}}{\partial t^2} = -k^2 e^{ikn_{opt}z} \Theta(z) I(t) \chi^{(2)} \widehat{e}\widehat{e}$$

Then taking the Fourier transform:

$$(77)\quad \frac{\partial^2 \overrightarrow{E}(z,\omega)}{\partial z^2} + k^2\epsilon(\omega)\overrightarrow{E}(z,\omega) = -k^2 e^{ikn_{opt}z}\Theta(z)I(\omega)\chi^{(2)}\widehat{e}\widehat{e}$$

Laplace transforming this using the complex refraction $\widetilde{n} = n + i\frac{\alpha}{2k}$ and transforming to $k\widetilde{n}$ space (this is the complex wave vector in the crystal) and inverse transforming back gives the general form of solution:

(78)

$$E(z,\omega) = E(0,\omega)e^{ik\widetilde{n}z} - \frac{I(\omega)\chi^{(2)}\widehat{e}\widehat{e}}{\widetilde{n}}\left(\frac{e^{ikz(\widetilde{n}-n_{opt})}-1}{n_{opt}-\widetilde{n}} + \frac{1-e^{ikz(\widetilde{n}-n_{opt})}}{n_{opt}+\widetilde{n}}\right)e^{ikn_{opt}z}$$

This is a combination of both forward and backward propagating waves. We can ignore the backwards propagation as it must be much smaller than the forward wave. Also, in general there is no wave at the start so in general for us $E(0,\omega) = 0$.

The transform back to time domain is done numerically for specific cases as the complex refraction and the susceptibility are usually frequency dependent.

Looking at the frequency domain solution we see that the wave vector mismatch due to differences in the index of refraction and the crystal length (z dependence) influence the magnitude of the spectral components. As a result we can use these to find the dominant frequency in our transform.

Physically, this suggests that the crystal response is centered around a frequency that is determined by the length of the crystal, the pulse duration of the optical envelope, and the difference in refractive indices.

One can further say that the difference in the refractive indices limits how far a propagating optical pulse will feed into the induced terahertz wave. When the optical pulse has moved by its own width ahead of the terahertz wave there can be no further constructive interaction. This characteristic length is called the walk-off length.

To improve efficiency and generate more THz one needs to use quasi-phase matching techniques in order to have generating structures thicker than the walk-off length.

6.2.3 Multicycle THz Generation by Engineered Domain Structures

When one uses domain layers that invert the direction of the second order polarization as in Figure 16 each domain contributes a half cycle wave constructing a multicycle THz pulse.[29][31]-[56] This contribution is built from the back forward much like the waves from the bow of a rapidly moving boat. This is because the THz is generated by the motion of the optical pulse through the engineered structure and the optical pulse typically outruns the THz generated pulse.

One should expect the optical pulse to outrun the terahertz waves inside the medium. This follows from the physical nature of the dielectric function

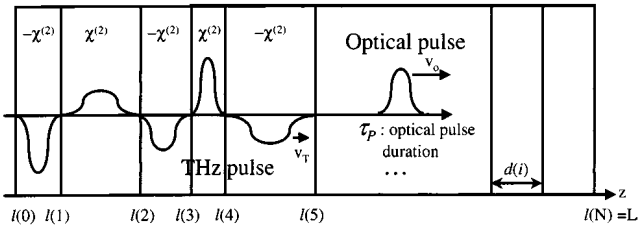

Figure 16: Schematic diagram of the THz wave form synthesis in a poled nonlinear crystal. The THz wave form coincides with the crystal domain structure.

in matter. transitions being quantized in nature act similar to delta functions. They will have a width due to certain effects such as Doppler broadening. In general, this extends as a tail into the lower frequencies while dropping off rapidly above the transition resonance. As a result the dielectric function at lower frequency will be larger than at higher frequency. Since the index of refraction is the real part of the square root of the dielectric function it too is higher at lower frequency.

The fact that $n_{opt} < n_{THz}$ typically is a wave vector mismatch that in general limits the length of phase matched THz pulse production. Once the optical pulse moves it's width ahead of the induced THz pulse there is no more constructive THz generation. Domains significantly longer than this generate a smaller signal with a distinctive spike shape. Domains significantly shorter have destructive interference as well leading to flattened out peaks in the middle of each domain.[49]

The one drawback to these structures is they must be engineered in ad-

vance and are fixed. However there is a great deal of flexibility in the engineering. Materials like $LiNbO_4$ have been engineered and fabricated for a period of years now as can be seen from the body of work referenced[31]-[56]. Among some of the shapes available are multi-domain periodically poled, alternating periodically poled, chirped, zero area, and fanned out.[50]

There are many techniques for generating periodic inversion in the crystal structure. One mentioned earlier is periodic poling. Periodic crystal structure inversion can be accomplished by other methods. Growth techniques resulting in alternating domains in layers such as orientation patterned gallium arsenide (OP-GaAs) or by assembly of wafers alternating the orientation by rotating the wafer 180 degrees about normal to the face are additional methods for construction of the periodic inversion in the crystal structure necessary for quasi-phase matching.

Gallium arsenide is not a ferroelectric crystal thus there is no remnant polarizability to use the periodic poling technique technique. However, in addition to OP-GaAs growth techniques, there are several methods for constructing domain inversion in GaAs. Diffusion bonding uses layers assembled in alternating order and then heated to partially melt together. Another method called optical contacting utilizes the surface tension between the wafers that arrises between the surfaces when the air between them is driven out under an applied pressure over a long time.

6.3 THz Time Domain Spectroscopy: Theory

6.3.1 Overview

THz-TDS is a pump-probe type of spectroscopy. The probe needs to be ultrafast (~100 femtosecond) to give well resolved data points as the probe must be much shorter than the THz signal to be measured. The pump beam must be ultrafast as well either to produce the THz signal using optical rectification or possibly in a special arrangement by difference frequency generation.

The signals must have their path lengths arranged such that they arrive at the detection stage together as it is the convolution that is essentially measured by electro-optic sampling. Since the THz signal is so much longer in period than the duration of the probe pulse the optical probe signal experiences only a DC electric field during it's passage through the crystal in which this electro-optic effect takes place. As a result, the probe signal experiences only a small rotation of the polarization axis directly proportional (to first order) to the time averaged THz electric field (averaged only over the optical pulse duration). By varying the relative path length between the two beams the THz electric field can be measured. This approach produces data with both phase and amplitude information.

To actually measure this polarization rotation one must have first fixed the polarization very precisely in the probe beam because, in practice, the rotation is only a few tens of milliradians. After the rotation in the electro-

optic crystal (Usually ZnTe) a 1/4 wave plate is used to convert the probe beam from linear to elliptically polarized. This wave plate is adjusted so that in the absence of signal the probe is circularly polarized. Since the rotation is small (On the order of milliradians) the ellipticity introduced is linearly proportional to the THz electric field. The elliptically polarized signal is passed through a Wollaston prism so that it will be broken into orthogonal components separated in space. These are incident on a pair of photodiodes connected in a push/pull configuration so that only the difference in signal is output. This signal is separated from background noise with a lock-in amplifier. This is then recorded as the data.

The pump beam is the one chosen for path length control by use of a computer controlled motorized linear stage with mirrors mounted such that the pump beam returns out parallel to the input at a fixed distance between input and output for all track positions. The pump beam is chosen because the THz produced has, by reason of it's longer wavelength, a larger diffraction limited spot size on the detection crystal than does the probe beam so the variance in convolution will be smaller if the beam walks several microns due to imperfections in the linear track construction or beam path alignment.

The THz produced along the pump path is typically single cycle. it may be multi-cycle if one uses either an adaptive approach to signal generation or a domain inversion structure in the crystal used as an emitter. Single cycle has the advantage of broad bandwidth while the other approaches produce narrow or even shaped spectrums with significantly higher spectral intensity.

The pump beam incident on the emitter crystal is typically the same frequency as the probe. However, this dissertation will present data from a two color THz-TDS system constructed by the author. Typically, in most THz-TDS systems the probe and pump beams are produced from a single ultrafast beam by a beam splitter (Usually 95% pump and 5% probe). In the two color system output from an optical parametric amplifier (OPA) is used as the pump beam while the probe is beam split from the input beam into the OPA.

6.3.2 Electro-Optic Measurement of THz Radiation

The standard reference I will follow in the main part here is by Gallot and Grischkowsky[8]. This approach is done in frequency space with the slowly varying envelope approximation. First, all the different frequency components are calculated. Next, the ellipsometry is calculated. Then, the actual detected signal is calculated from there.

I will begin by defining some terms. The axis of propagation is common for both the THz and the optical pulse and will be referred to as z' which is the [1,1,0] direction. We will consider only $\bar{4}$3m crystals for simplicity as ZnTe is the crystal used for detection in the two color THz-TDS system I will describe in the experiment description. The A_j's are the slowly varying amplitude envelopes. Subscripts of opt are for the optical pulse. THz as a subscript refers to the THz pulse. Using a + subscript refers to the generated sum frequency. and a - subscript refers to the difference frequency component.

The optical carrier frequency will be defined as ω_0. $\omega_+ = \omega_{opt} + \omega_{THz}$ and $\omega_- = \omega_{opt} - \omega_{THz}$ for this case. The wave vectors will be considered to be complex so as to include absorption, thus $k = k\prime + i\beta$. Defining the electric fields for these 4 waves is done below.

$$\text{(79a)} \quad \overrightarrow{E}_{opt}(z', \omega_{opt}) = A_{opt}(z', \omega_{opt} - \omega_0) e^{i(k_{opt} z' - (\omega_{opt} - \omega_0)t)} \widehat{u}_{opt}$$

$$\text{(79b)} \quad \overrightarrow{E}_{THz}(z', \omega_{THz}) = A_{THz}(z', \omega_{THz}) e^{i(k_{THz} z' - \omega_{THz} t)} \widehat{u}_{THz}$$

$$\text{(79c)} \quad \overrightarrow{E}_{+}(z', \omega_+ - \omega_0) = A_{+}(z', \omega_+ - \omega_0) e^{i(k_+ z' - (\omega_+ - \omega_0)t)} \widehat{u}_{+}$$

$$\text{(79d)} \quad \overrightarrow{E}_{-}(z', \omega_- - \omega_0) = A_{-}(z', \omega_- - \omega_0) e^{i(k_- z' - (\omega_- - \omega_0)t)} \widehat{u}_{-}$$

Now, recalling the wave equation from the previous section with the nonlinear polarization as only the sum and difference frequency components, one can set up the differential equation for the slowly varying envelopes. The two different cases (+ and -) will transform similarly so I will give detailed explanation of just the + case.

$$\text{(80)} \quad \nabla^2 \overrightarrow{E} - \frac{1}{\epsilon_0 c^2} \frac{\partial^2 \overrightarrow{D}^{(1)}}{\partial t^2} = \frac{1}{\epsilon_0 c^2} \frac{\partial^2 \overrightarrow{P}^{(NL)}}{\partial t^2}$$

$$\text{(81)} \quad \nabla^2 \overrightarrow{E}_{+}(z', \omega_+ - \omega_0) - \frac{1 + \chi^{(1)}}{c^2} \frac{\partial^2 \overrightarrow{E}_{+}(z', \omega_+ - \omega_0)}{\partial t^2} = \frac{1}{\epsilon_0 c^2} \frac{\partial^2 \overrightarrow{P}_{+}^{(NL)}}{\partial t^2}$$

Since propagation is limited to the z' direction the laplacian above is just the second partial derivative in the z' direction. and using the slowly varying envelope approximation this is kept only to the first derivative so for the summed nonlinear polarization:

$$(82)\frac{1}{\epsilon_0 c^2}\frac{\partial^2 \overrightarrow{P}_+^{(NL)}}{\partial t^2} = 2ik_+ e^{i(k_+ z' - (\omega_+ - \omega_0)t)}\frac{\partial A_+(z', \omega_+ - \omega_0)}{\partial z'}$$
$$-k_+^2 A_+(z', \omega_+ - \omega_0)e^{i(k_+ z' - (\omega_+ - \omega_0)t)} + \frac{1+\chi^{(1)}}{c^2}(\omega_+ - \omega_0)^2 A_+(z', \omega_+ - \omega_0)$$
$$e^{i(k_+ z' - (\omega_+ - \omega_0)t)}$$

Next, substituting the second order term (because it is the dominant term in the nonlinear polarization) for the nonlinear polarization.

$$(83)\qquad \frac{\partial^2 \chi^{(2)}\overrightarrow{E}_{opt}(z', \omega_{opt})\overrightarrow{E}_{THz}(z', \omega_{THz})}{c^2 \partial t^2} = 2ik_+ e^{i(k_+ z' - (\omega_+ - \omega_0)t)}$$
$$\frac{\partial A_+(z', \omega_+ - \omega_0)}{\partial z'} - k_+^2 A_+(z', \omega_+ - \omega_0)e^{i(k_+ z' - (\omega_+ - \omega_0)t)}$$
$$+\frac{1+\chi^{(1)}}{c^2}(\omega_+ - \omega_0)^2 A_+(z', \omega_+ - \omega_0)e^{i(k_+ z' - (\omega_+ - \omega_0)t)}$$

Since $\omega_{opt} \gg \omega_{THz}$ only the second derivative of the optical field is relevant to first order.

$$(84)\qquad -\frac{\omega_{opt}^2}{c^2}A_{opt}A_{THz}e^{i((k_{opt}+k_{THz})z' - (\omega_{opt}+\omega_{THz}-\omega_0)t)} \times \left|\chi^{(2)}\widehat{u}_{opt}\widehat{u}_{THz}\right| =$$
$$(2ik_+\frac{\partial A_+(z', \omega_+ - \omega_0)}{\partial z'} - k_+^2 A_+(z', \omega_+ - \omega_0)$$
$$(85)\qquad +\frac{1+\chi^{(1)}}{c^2}(\omega_+ - \omega_0)^2 A_+(z', \omega_+ - \omega_0))e^{i(k_+ z' - (\omega_+ - \omega_0)t)}$$

Cancelling the common time exponential throughout the equation and recognizing the term from the D field is $k_+'^2 \overrightarrow{E}_+$ allows this to be written more compactly. Also, introducing $p_+^{(2)} = A_{opt} A_{THz} \left| \chi^{(2)} \widehat{u}_{opt} \widehat{u}_{THz} \right|$ streamlines this to a manageable form again.

$$(86) \quad -\frac{\omega_{opt}^2}{c^2} e^{i(k_{opt}+k_{THz})z'} p_+^{(2)} = 2ik_+' e^{ik_+ z'} \frac{\partial A_+(z', \omega_+ - \omega_0)}{\partial z'}$$

$$(87) \quad + 2ik_+' \beta_+ A_+(z', \omega_+ - \omega_0) e^{ik_+ z'}$$

Note the β_+^2 has been dropped as it should be vanishingly small compared to the other terms.

Rearranging and expanding the complex wave vector term in the exponential then defining a phase matching term from the wave vectors, $\Delta k_+' = k_{opt}' + k_{THz}' - k_+'$,(known as the wave vector mismatching term)[8] and using the undepleted pump approximation one arrives at:

$$(88) \quad \frac{\partial A_+(z', \omega_+ - \omega_0)}{\partial z'} + \beta_+ A_+(z', \omega_+ - \omega_0) = i \frac{\omega_{opt}^2}{2k_+' c^2} e^{i\Delta k_+' z' - (\beta_{opt} + \beta_{THz}) z'} p_+^{(2)}$$

Similarly for the difference frequency case the equation is:

$$(89) \quad \frac{\partial A_-(z', \omega_- - \omega_0)}{\partial z'} + \beta_- A_-(z', \omega_- - \omega_0) = i \frac{\omega_{opt}^2}{2k_-' c^2} e^{i\Delta k_-' z' - (\beta_{opt} + \beta_{THz}) z'} p_-^{(2)}$$

where $\Delta k'_{-} = k'_{opt} - k'_{THz} - k'_{-}$

Clearly, the solution needs to be an exponential form. Since as the beams enter the crystal there is no sum or difference field then $A_{\pm}(z' = 0) = 0$. So we require a difference of two exponentials. This gives a convenient way to obtain the β_{+} term as it is simply the derivative of the expected sum frequency attenuation in the crystal. So a trial solution involving the difference between exponentials of the wave vector mismatch and the sum frequency attenuation can be plugged back in successfully if one uses the appropriate constants. The form of the solution is given below.

$$(90) \quad A_{\pm}(z', \omega_{\pm} - \omega_0) = i\frac{\omega_{opt}^2}{2k'_{\pm}c^2}p_{+}^{(2)}\frac{e^{i\Delta k'_{\pm}z' - (\beta_{opt}+\beta_{THz})z'} - e^{-\beta_{\pm}z'}}{\Delta k'_{\pm} - (\beta_{opt} + \beta_{THz} - \beta_{\pm})}$$

For a crystal of length ℓ this gives a final amplitude for our sum and difference frequency components as follows.

$$(91) \quad A_{\pm}(\ell, \omega_{\pm} - \omega_0) = i\frac{\omega_{opt}^2}{2k'_{\pm}c^2}p_{+}^{(2)}\frac{e^{i\Delta k'_{\pm}\ell - (\beta_{opt}+\beta_{THz})\ell} - e^{-\beta_{\pm}\ell}}{\Delta k'_{\pm} - (\beta_{opt} + \beta_{THz} - \beta_{\pm})}$$

Assuming that as small as the optical bandwidth is that the THz bandwidth is smaller yet and assuming no depletion of the optical signal we can sum up all the contributions from the original optical pulse and the generated components at a given frequency, ω, if we recognize that for the sum frequency case $\omega = \omega_{opt} + \omega_{THz}$, and for the difference frequency case

$\omega = \omega_{opt} - \omega_{THz}$. Then by integrating over the bandwidth of the THz pulse we can get the contributions to ω from each optical component.

$$(92) \quad E_{\pm}(\ell,\omega) = i\int_{-\infty}^{\infty} \frac{\omega^2}{2c^2 k'_{+}} \chi^{(2)}_{ijk}(\omega;\omega_{THz},\omega \mp \omega_{THz}) \frac{e^{i\Delta k_{\pm}\ell}-1}{i\Delta k_{\pm}} e^{ik_{+}\ell} A_{THz}(\omega_{THz}) e^{-i\omega_{THz}(t-\tau)} A_{opt}(\omega \mp \omega_{THz} - \omega_0) e^{-i(\omega \mp \omega_{THz} - \omega_0)t} d\omega_{THz}$$

Here I've introduced τ, the relative delay between the optical and THz pulses. This result gives us an exact amplitude for each of the sum and difference frequency components. One notes by inspection that both are directly proportional to the optical pump field. Assuming they are both small relative to the optical pump electric field then along some lab frame coordinates x and y we can rearrange or linear superposition and define some phase modulation angles that can by connection back to these relationships be exactly calculated.

$$(93a)\ E_x(\omega) = E_{opt_x}(\omega)\left(1 + i\frac{E_{+_x}(\omega) + E_{-_x}(\omega)}{iE_{opt_x}(\omega)}\right)$$

$$(93b) \qquad = E_{opt_x}(\omega)(1 + i\phi_x(\omega,\tau))$$

$$\text{(94a) } E_y(\omega) = E_{opt_y}(\omega)(1 + i\frac{E_{+_y}(\omega) + E_{-_y}(\omega)}{iE_{opt_y}(\omega)})$$

$$\text{(94b)} = E_{opt_y}(\omega)(1 + i\phi_y(\omega, \tau))$$

Now, using the first order Euler expansion of exponentials this can be rewritten to the complex form. Since we want only the real part for calculation of the measurement I going directly to the real part of the full wave equation we then have:

$$\text{(95a) } E_x(\omega) = E_{opt_x}(\omega)\cos(k(\omega)z - \omega t + \phi_x(\omega, \tau))$$

$$\text{(95b) } E_y(\omega) = E_{opt_y}(\omega)\cos(k(\omega)z - \omega t + \phi_y(\omega, \tau))$$

The next step is to introduce the phase shift from a 1/4 wave plate. Then we will add in the effects of the Wollaston prism splitting the major and minor axis components into two separate beams. Figure 17 shows the basic schematic of detection.

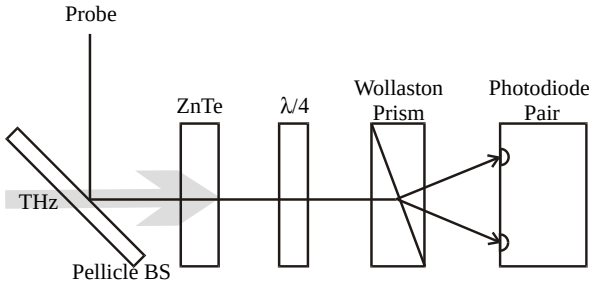

Figure 17: The probe and the THz beams are directed as co-propagating beams onto the electro-optic crystal (ZnTe) where the optical beam receives its polarization rotation. The $\lambda/4$ wave plate converts the signal to an elliptical signal. Then the Wollaston prism breaks the elliptical beam into orthogonal linear component beams propagating at an angle relative to each other. These two separate beams are then incident on a photodiode matched pair connected as a difference detector.

$$\text{(96a) } E_x(\omega) = a_0(\omega)\cos(k(\omega)z - \omega t + \phi_x(\omega,\tau))$$

$$\text{(96b) } E_y(\omega) = a_0(\omega)\cos(k(\omega)z - \omega t + \phi_y(\omega,\tau) + \frac{\pi}{2})$$

Since the rotation of the beam from the original polarization is small (on the order of milliradians) we have a near circular ellipse. For a nearly circular ellipse we can define $\phi = \phi_y - \phi_x$ and then to first order the major and minor axes can be defined by:

$$\text{(97a) } a(\omega) = a_0(\omega)(1 + \frac{1}{2}\phi(\omega))$$
$$\text{(97b) } b(\omega) = a_0(\omega)(1 - \frac{1}{2}\phi(\omega))$$

The detectors will have signals proportional to the incident intensities. The rotation angle is directly proportional to the electric field for small rotations. So to get a value proportional to the electric field the difference between the two intensities is our signal. Thus using two photodiodes balanced as a difference pair we take get an output proportional to the measured signal. So I will call this proportional output S. Then we get the following:

$$\text{(98) } S = I_a - I_b = \frac{\epsilon_0 c}{2}\int_0^\infty (|a(\omega)|^2 - |b(\omega)|^2)d\omega = \epsilon_0 c \int_0^\infty |a_0(\omega)|^2 \phi(\omega) d\omega$$

Next, lets define the effective susceptibility for the difference in our lab directions as $\chi^{(2)}_{eff} = \chi^{y}_{eff} - \chi^{x}_{eff}$. Then by substitution into the integral above using the earlier developed relationship for the difference electric field one gets the Electro-Optic signal as:

$$(99) \qquad S(\tau) = \frac{\epsilon_0 c}{2} \int_{-\infty}^{\infty} \int_{-\infty}^{\infty} A_{THz}(\omega_{THz}) \frac{\omega^2}{c^2 k'(\omega)} e^{-2\beta\ell}$$
$$\chi^{(2)}_{eff}(\omega; \omega_{THz}, \omega - \omega_{THz}) \frac{e^{i\Delta k_+(\omega_{THz},\omega)\ell} - 1}{i\Delta k_+(\omega_{THz}, \omega)}$$
$$A^*_{opt}(\omega - \omega_0) A_{opt}(\omega - \omega_{THz} - \omega_0) e^{-i\omega_{THz}\tau} d\omega_{THz} d\omega$$

We can take all the ω dependent terms out and make a new function and this makes the behavior of the measurement clearer. Defining $f(\omega_{THz})$ then rewriting our signal function below shows:

$$(100) \qquad f(\omega_{THz}) = \int_{-\infty}^{\infty} \frac{\omega^2}{k'(\omega)} e^{-2\beta\ell} \chi^{(2)}_{eff}(\omega; \omega_{THz}, \omega - \omega_{THz})$$
$$\frac{e^{i\Delta k_+(\omega_{THz},\omega)\ell} - 1}{i\Delta k_+(\omega_{THz}, \omega)} A^*_{opt}(\omega - \omega_0) A_{opt}(\omega - \omega_{THz} - \omega_0) d\omega$$

$$(101) \quad S(\tau) = \frac{\epsilon_0}{2c} \int_{-\infty}^{\infty} \int_{-\infty}^{\infty} A_{THz}(\omega_{THz}) f(\omega_{THz}) e^{-i\omega_{THz}\tau} d\omega_{THz}$$

It is now easily seen that if the optical integrand, $f(\omega_{THz})$, has no THz frequency dependence then the signal is directly proportional to the time domain THz electric field amplitude at time τ. The issues of interest here are the frequency dependence of the nonlinear susceptibility and the THz absorption as these are terms where THz frequency dependence enters.

For our case with ZnTe the TO phonon mode at 5.3 THz[57] is the source of frequency dependence. For frequencies below 3 THz one is sufficiently far enough away from the tail of this phonon to get a flat response.

The most recent modeling of the effects of the detection crystal gave the relationship using a complex index of refraction for the THz instead of a complex wave vector.[27] This result matched nicely with experiment. Their result was obtained by similar procedures to those already shown for optical rectification.

$$(102)\quad S(\tau) \propto \int_{-\infty}^{\infty} E_{THz}(\omega) \frac{e^{ik\ell(\tilde{n}_{THz}-n_{opt})}-1}{ik(\tilde{n}_{THz}-n_{opt})} e^{-i\omega\tau} d\omega$$

This sets additional constraints on the optical thickness of the crystal as there is a wave vector mismatch to take into consideration here. This however is not much of a problem for ZnTe in the below 3 THz regime when using a near infrared optical beam of between 800 and 830 nm. In that range the difference in refractive indices is small enough that crystal length necessary to see this is greater than 2 mm as can be calculated using the improved dispersion relation[Heinz-Weling reference]. In practice this isn't an issue. In fact, at ~817 to 819 nm the majority of the desired spectral range has a vanishingly small wave vector mismatch.

One of the few drawbacks of detection using the electro-optic effect is the difficulty in absolute power measurement. Every time the system is aligned

one would need to calibrate the system for such measurements. As this is time consuming and difficult in practice it is more common to devise a separate experiment to do this measurement.

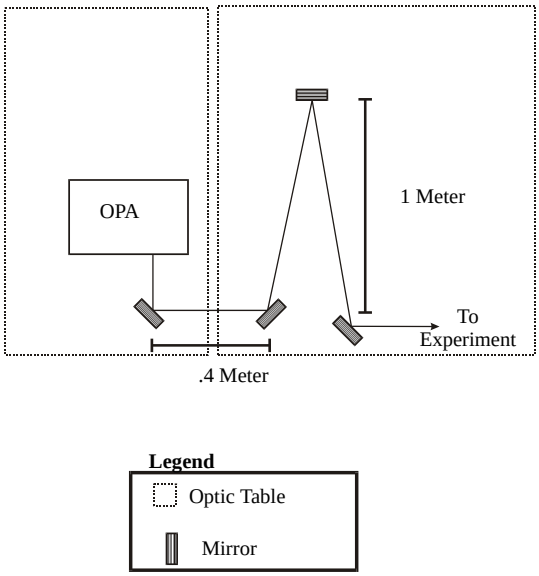

Figure 18: The beam was passed far enough along an extended path that the beam diverged to have a sufficiently large enough diameter. This decreased the beam peak intensity low enough to prevent damage to optics.

7 THz Power Measurement using a Bolometer

7.1 The Experiment: Introduction

The OPA output path is set through at least 2 meters path so that the beam (Typically exiting the OPA convergent) has spread its waist far enough not to damage optics other than mirrors such as variable attenuators as shown in Figure 18.

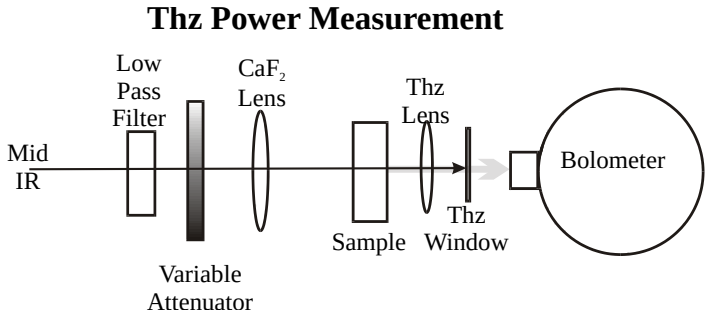

Figure 19: The incoming signal is filtered to remove visible components and atenuated to the correct power level to avoid surface damage. It is then focused onto the sample where THz waves are produced. The THz is then focused into a bolometer.

The beam can then be passed through a low pass filter to remove the visible components that exit the OPA with the signal or idler beams. This is sent through a variable attenuator to control the power incident on a sample. The beam is then focused onto the sample generating crystal by use of a calcium fluoride lens. The typical lens used was a 200 mm focal length CaF_2 lens. A THz window, typically a piece of plastic or paper, is used to block the mid IR beam that exits with the THz from the crystal. From there a THz lens, usually a f=50 mm picarin lens, focuses the THz output into a bolometer. The experimental setup is shown in Figure 19.

For GaAs we used the Idler for the 1.8 to 2.5 μm range and on the initial occasion when we used signal and idler together to do DFG it was set up by Vladimir Kozlov of Microtech Instruments. At a later occasion the results were reproduced and that was set up by the author with the help of Joel Wetzl. DFG was done for 3.5 and 4.4 μm.

The initial experiment was set up by Konstantin Vodopyanov, Yun-Shik Lee, and the author. The experiment was reproduced with corroborative data as mentioned by the author and Joel Wetzl. Data was analyzed by Yun-Shik Lee, Konstantin Vodopyanov and the author.

7.2 The Experiment: Additional details and measurements

Once properly filled as outlined in appendix 4 the bolometer is taken to the work location. An oscilloscope is hooked the output. The trigger output from the Legend system is used as the trigger signal for the oscilloscope. The signal will appear as a rounded sawtooth shape. This is because the decay time of the bolometer output is much longer than the pulse width so the bolometer reaches the full output level quickly then decays slowly.

Alignment is very critical and obtaining the first signal may take some time. The sample is mounted so it can be rotated to optimize the efficiency of THz production. After optimization of both the crystal (Both placement at the focal plane and rotation angle) and the bolometer placement then take an averaged measurement gives the averaged signal. The operating manual contains the conversion equation so that absolute output power may be calculated.

To calculate the quantities of interest such as optical to THz conversion efficiency there are several additional measurements needed. These measure-

ments are the same optical beam characterization measurements needed in the earlier transmission and z-scan experiments and are outlined in appendix 3.

One of the simple measurements necessary at this point is the average power of the input beam. Using a J-9 Molectron energy meter gives this data. To calculate conversion efficiency and quantum efficiency it is necessary to do additional measurements that give important data relevant to correctly calculate $\chi^{(2)}$ and other useful quantities include knife-edge measurement of the beam profile, spectral measurement by a monochromator, and pulse duration using an autocorrelator (See appendix 3).

It should be noted that often an alignment helium-neon (HeNe) laser can make setup and alignment much easier. The experiment described here was done both with and without one as I found it unnecessary in this case. More demanding experiments such as THz interferometry require one.

8 THz Frequency Measurement Using Interferometry

This experiment was a major collaborative effort between Konstantin Vodopyanov, Yun-Shik Lee, Jeremy Danielson, Vladimir Kozlov and the author. Laser operation was a collaboration between Yun-Shik Lee and the author. Optics placement was performed by Vladimir Kozlov and Konstantin Vodopyanov. Placement of the bolometer and alignment was shared work by the entire group at various phases. Construction of the beam splitter was done by Jeremy Danielson using materials provided by Vladimir Kozlov. The Michelson interferometer was assembled by Jeremy Danielson. The data was collected by Jeremy Danielson, Naaman Amer, and the author under monitoring by the rest of the team.

This experiment requires the use of a HeNe laser beam as an alignment beam. Mid IR and THz are not viewable with our IR viewer so the only way to align the beam is with a visible co-propagating beam. The standard technique for doing this is to send the HeNe beam through 2 mirrors as alignment mirrors and then have it incident on a beam splitter that the mid IR beam is passing through. the HeNe beam is incident from the side the Mid IR beam passes out of at the exact location of the exiting beam and the exact angle such that the transmitted HeNe beam overlaps the mid IR reflected beam. Then, by geometric optics, the two beams are co-propagating. This

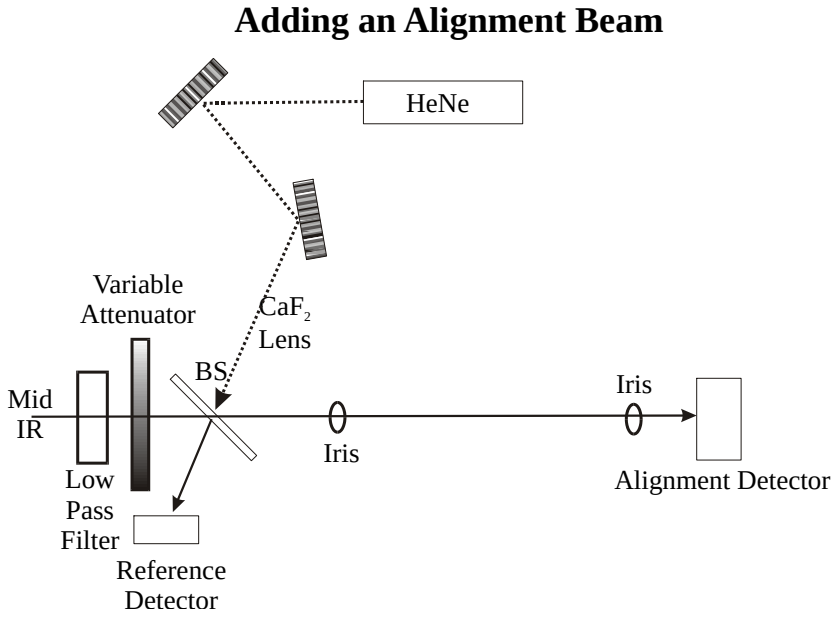

Figure 20: The mid IR beam is aligned through 2 irises using a pyroelectric detector and oscilloscope to measure throughput. Then, using two steering mirrors the visible beam from the Helium-Neon laser is aligned to the same two irises. The spacing between irises is chosen to be the pathlength of the experiment.

is seen in Figure 20.

In practice the alignment is done using two irises and an IR detector after the far iris. The irises are place centered on the Mid IR beam with at least as much distance between them as the path length of the experiment. Then the HeNe beam is adjusted to pass through them both in a centered fashion also. After this the mid IR beam can be blocked and the HeNe beam used to align the components. This means optically opaque components are placed after the full beam path is established starting with the one farthest along

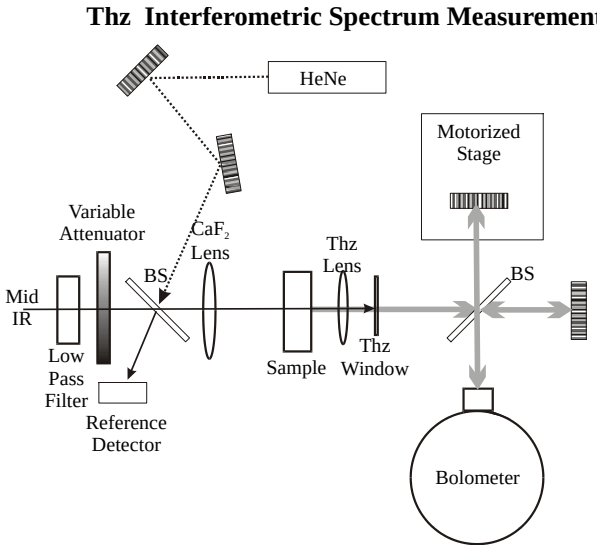

Figure 21: A reference signal is collected using a beam splitter. The beam splitter also doubles as the input point for an alignment beam. The THz is generated the same as the previous experiment. However a THz lens is placed close to the sample so that the focal length is 200 mm. Then a 25 μm Mylar beamsplitter is used to construct a Michelson interferometer. The bolometer is placed to receive the interference signal.

the beam path.

The concept of the experiment seen in Figure 21 is to use a Michelson interferometer with a motorized computer controllable stage to generate the interferogram of the THz produced from various GaAs samples. This interferogram is then Fourier transformed and analyzed for the spectrum of the samples in question. Software used for data collection was THz.vi. Signal from the bolometer was sent to the lock-in amplifier.

The mid IR beam is focused onto the QPM sample where the THz waves

will be generated. A picarin lens is used to focus the THz waves 200 mm away. Then a plastic material is used to block the mid IR and as a window for the THz waves. A 25 μm thick mylar beam splitter divides the THz signal between two arms of a Michelson interferometer. One of the flat metal mirrors used in this interferometer is mounted on a motorized linear stage. The interference signal is incident on the bolometer. The average pathlength from the THz lens to the bolometer is adjusted to be ~200 mm on either path through the interferometer. The signal is sent to a lock-in amplifier. the output recorded in a data acquisition computer.

To convert the interferogram divide the data by speed of light in the form of 300 microns per picosecond by two times the path length in microns. This gives the interferogram the correct time scaling. Finally, a fast Fourier transform of the data will give the spectrum of the THz.

8.1 Results of theTHz Power Measurement and interferogram Experiment

This section discusses the results of our THz interferometric experiments and compares them to theory. These results were published [59] by Konstantin Vodopyanov, Yun-Shik Lee, Martin Fejer, and the author. The results discussed include QPM structure to frequency matching in selected samples, and what was at the time a world record set in optical-to-THz conversion efficiency.

THz waves are produced in the optical rectification process using an electro-optic medium via self-difference-frequency mixing. This frequency mixing between the different Fourier components of the optical pulse was first demonstrated with picosecond pulses in $LiNO_3$ [58][59], ZnTe, ZnSe, CdS, and quartz [60] crystals. This technique was later demonstrated using femtosecond pulses [30]. Using femtosecond pulses has become the standard method for generating single-cycle broadband THz pulses.

The standard technique calls for the use of thin (Typically less than 1 mm) electro-optic crystals such as ZnTe. There are several reasons for use of such thin crystals. Phase matching constraints being the dominant reason. High THz absorption is another good reason for keeping the crystal thickness small. As a result the optical-to-THz conversion efficiencies achieved in optical rectification have been typically low at 10^{-6} - 10^{-9}[60]. There has been recent improvement by use of several different techniques including

tilted intensity fronts [61], QPM structures [62] in periodically poled lithium niobate (PPLN), and cryogenic cooling in PPLN[45]. The first method mentioned reached 5×10^{-4} conversion efficiency. The second and third methods combined resulted in 10^{-5}conversion efficiency.

Because of the small group velocity mismatch between THz and the mid IR and the low THz absorption in GaAs ($\alpha_{THz} = 0.5 - 4.5$ cm^{-1} at 1-3 THz [63]) it is a good candidate for quasi-phase matching. THz wave generation has been demonstrated using QPM structures in GaAs via optical rectification from femtosecond mid IR pulses [64]. Additionally, GaP QPM structures (also in the zincblende crystal group) have been used to produce THz waves using difference frequency generation from nanosecond near IR pulses [65]. A careful study and characterization of the THz frequency to QPM period were called for as a result.

Our source for this experiment was an optical parametric amplifier (OperA from Coherent Inc.) system pumped by a Ti:Sapphire 1 KHz regenerative amplifier (Legend, Coherent Inc.) at 800 nm. The effective range was extended further into the mid IR by DFG between the OPA signal and idler outputs to give a tunable pulse range of 2 to 4.4 μm for our input range. Typically, we saw pulse energy and duration of up to 3 μJ and 100 femtoseconds respectively.

The reason for working above 2 μm is to avoid 2 photon absorption effects. This avoids additional losses in the pump as well as avoiding losses at THz frequencies due to induced absorption caused by the generated free carriers.

We used two types of QPM GaAs samples. The first was diffusion-bonded GaAs (DB-GaAs) which is constructed by stacking layers of wafers with each wafer rotated 180 degrees about the mating surfaces <1,1,0> normal from the previous layer and then heating the stack while under pressure to cause the surfaces to diffuse together. The second type, orientation-patterned GaAs (OP-GaAs), is grown by photolithography, molecular beam epitaxy, and hydride vapor phase epitaxy to grow periodic inversions directly into the material.[66]

DB-GaAs is a difficult discontinued technique with a low yield whose principle advantage is that when successful produces a large clear aperture. While the principle advantage of OP-GaAs is the higher yield and consistently reproducible structures. The second advantage of OP-GaAs is it holds the promise of producing specialized structures similar to poled lithium niobate such as fanned out and zero area pulse.

The samples were not given anti-reflection coatings. The principle characteristics of interest are listed in Table 10.1.

Sample	**QPM type**	**A(mm^2)**	**L(mm)**	**Period (μm)**
DB-77	DB-GaAs	10x10	6	504
A3	OP-GaAs	0.4x3	3	1277
A10	OP-GaAs	0.4x3	10	1277
B5	OP-GaAs	0.4x3	5	759
B10	OP-GaAs	0.4x3	10	759
C5	OP-GaAs	0.4x3	5	564

Table 1: Parameters of the QPM GaAs samples

The optical pump beam with a beam size (1/e2 intensity radius) ranging between w=300 μm and The mid IR optical pump beam was focused onto a given sample. The beam waist varied in size for the different samples. It ranged from 300 μm to 1.5 mm. The beam was incident on the <1, 1, 0> direction of the sample. The THz pulse output was focused using a picarin lens through a black polyethylene window (To remove the mid IR pump beam) into a liquid helium cooled bolometer employing a silicon detector element. First the absolute power was measured for a given sample. Then the setup was rearranged by installing a THz Michelson interferometer with the bolometer as the detector element.

The Michelson interferometer was constructed using 2" diameter flat gold mirrors and a 25 μm mylar beam splitter. One of the mirrors was mounted on a computer controlled motorized linear stage. By changing the path length of this arm and taking a measurement from the bolometer through our lock-in amplifier (all under computer control) we took the interferogram of the selected samples.

According to theory the frequency of the generated THz pulses from these QPM structures should be centered [62] at $\nu_{THz} = c/\Lambda\Delta n$ where c is the speed of light, Λ is the layer thickness, and Δn is the difference between the THz and optical refractive indices. For GaAs n_{THz} is nearly constant at 3.6 [63] when well below the lowest phonon resonance of 8.1 THz [67]. The index of refraction for the optical group varies from 3.43 at 2 μm to 3.33 at 4.4 μm [64]. Also according to theory, the spectral width of the THz wave

packet is determined by the QPM acceptance bandwidth which is defined as $\Delta\nu_{THz} = c/L\Delta n$ where L is the length of the crystal.

By dividing the interferogram distance by c/4 one gets the interferometric temporal spectrum. Fourier amplitude transformation from there gives the power spectrum. The spectra of selected samples can be seen in Figure 22. At the top of each interferogram the water vapor absorption spectra is displayed. One can readily see that the water vapor spectrum has distorted the sample spectra. The small inset to the left in each part is the original time interferogram for the displayed spectrum. It is interesting to note that in Figure 22 (d) there is a second peak corresponding to three times the frequency of the primary peak and containing $1/3^2$of the power as one would expect for a third order QPM harmonic[68].

The observed central frequencies and bandwidths are in good agreement with theory. Displayed in Figure 23 is the tuning curve relating layer thickness and generated THz frequency for an input pump beam of 4.4 μm. We generated THz wave packets with central frequencies between .9 and 3 THz demonstrating the wide frequency range of tuning this technique is capable of.

In Figure 24 the optical-to-THz conversion efficiency using a 3.5 to 4.4 μm input beam shows the 2.9×10^{-4} efficiency that at the time of the experiment was a world record using the DB-GaAs sample with the 504 μm thick layers.

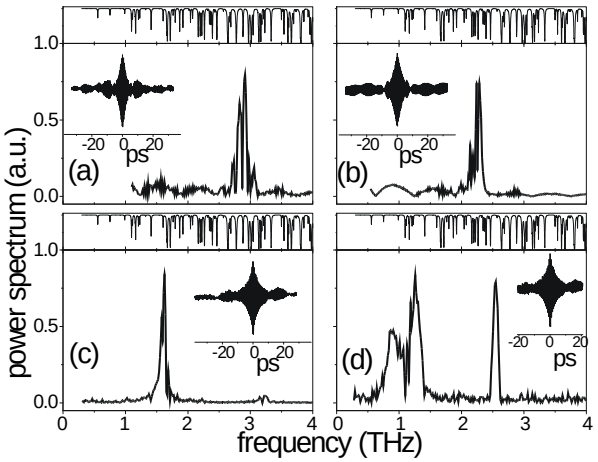

Figure 22: Spectra of the THz pulses obtained by Michelson interferometry. (a) Sample DB-77, pump at 2.03 μm; (b) sample DB-77, pump at 3.5 μm; (c) sample B10, pump at 4.4 μm; (d) sample A10, pump at 4.4 μm. The spectra are distorted by water vapor absorption (HITRAN water transmission spectrum for 10 cm. path is shown on top of each plot). Insets show original interferograms.

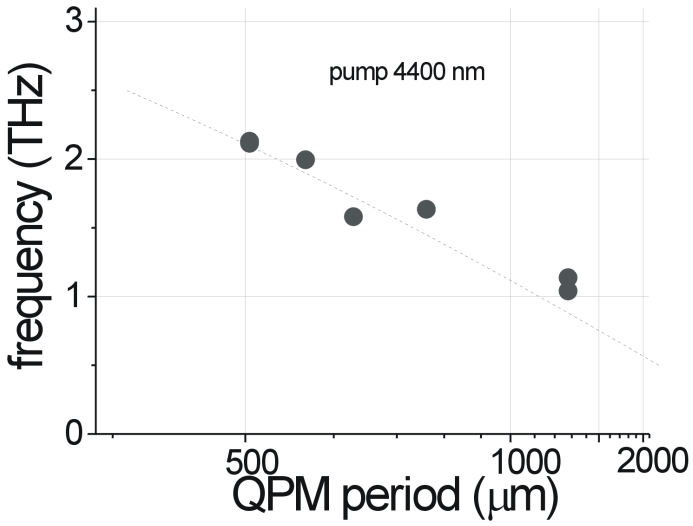

Figure 23: THz tuning curve for the 4.4 μm pump wavelength. Dashed curve - theoretical.

The improved performance seen in this sample over the OP-GaAs samples is attributed to two causes. One is due to the limited height (.4 mm) causing beam clipping as the sample height was about twice the THz wavelength for those samples. The other is that the diffusion bonded sample in question was actually constructed of layers of <1, 1, 1> GaAs so for that case the nonlinear optical coefficient is larger by a factor of $\sqrt{4/3}$.

The roll off seen at high intensity causing efficiency to drop below the theoretical model is probably due to nonlinear refraction causing self-phase modulation and self-focusing inside the sample at high intensity. From the studies presented earlier one can calculate that for a 6 mm sample with central intensity of 2 GW/cm^2 the nonlinear phase shift at 3.5 μm wavelength

is π at the beam center.

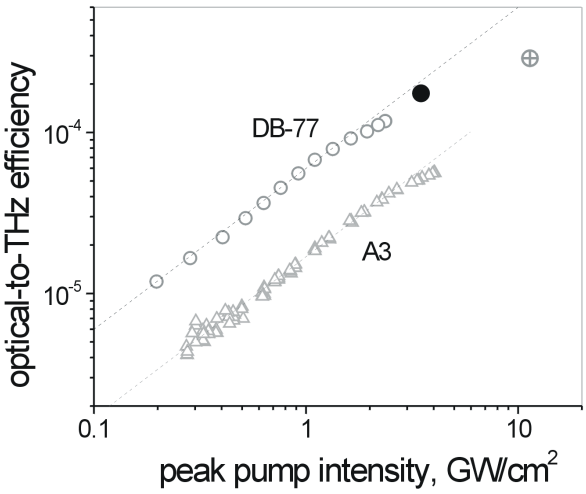

Figure 24: Optical-to-terahertz conversion efficiency as a function of peak pump intensity for the sample DB-77 (central frequency ~2.2 THz, circles) and A3 (central frequency 1.5 THz, triangles). The average pump beam size was 810 μm (open circles), 520 μm(closed circles), 590 μm (triangles) and 300 μm (crossed circles). Dashed lines - linear fits.

The diffusion bonded sample generated .66 nJ of 2.2 THz centered wave packet output power. using 2.3 μJ pump pulse energy with a beam waist of 300 μm at 3.5 μm wavelength corresponding to the quoted 2.9×10^{-4} optical-to-THz conversion efficiency. Since the samples were uncoated we can calculate the internal conversion efficiency using the fact that a significant amount of the incident power is reflected. The internal optical-to-THz conversion efficiency is then 8.7×10^{-4} which still is a world record. One can also calculate

the photon conversion efficiency. Using the fact that 1 THz corresponds to 300 μm we can calculate the photon conversion efficiency ($\eta^{\gamma}_{opt\rightarrow THz}$) using $\eta^{\gamma}_{opt\rightarrow THz} = \eta_{opt\rightarrow THz}\frac{\lambda_{THz}}{\lambda_{opt}} = 3.3\%$ for the internal photon conversion efficiency. This agrees well with the calculated values using the known nonlinear optical coefficient for optical rectification as $d_{eff} = (2/\pi)d_{14}$. The coefficient, d_{14} (47pm/V), having been derived from the electro-optic coefficient, r_{14} (1.5 pm/V) [69].

Clearly, this demonstrates that efficient THz wave production across a wide band is possible.

9 THz Time Domain Spectroscopy: Experimental Setup

The probe beam path was adjusted to have a matching path length by carefully placing the components along that path. The path is shown below in Figure 25. With the power dialed down low using the variable attenuator on the probe path the IR viewer was used to carefully align the near IR beam from the beam splitter before the OPA through the irises along the beam path. The beam splitter itself was not typically used for this alignment as that affects OPA operation by slightly changing the beam input location. If alignment was so far off this was required the OPA needed retuning after this was done. For this reason I aligned the probe beam first when setting up the system for data collection.

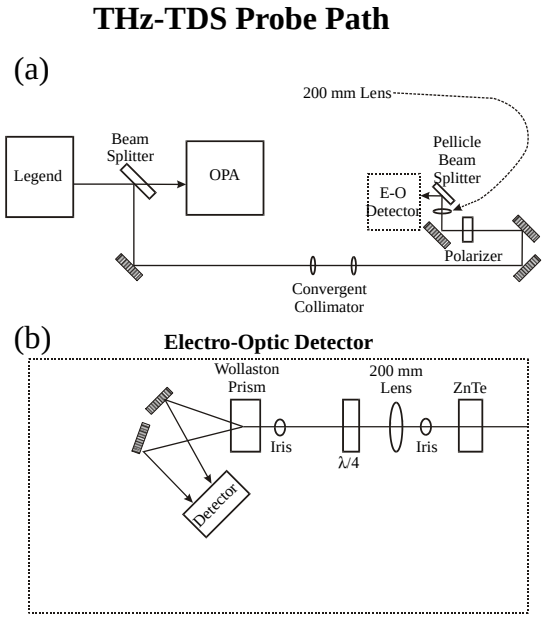

Figure 25: The general path is shown in (a). The Legend system output has 5% beamsplit into the probe path. A 3:1 convergent collimator shrinks the beam waist to close to 1 mm. The beam follows a path that has been adjusted to give the same time delay as the pump path. Eventually it reaches a polarizer where the polarization is precisely fixed. From there it isreflected from the pellicle beam splitter onto the ZnTe crystal. In (b) the detection system is shown.

Each mirror along the path is used in typical optical lever fashion. That means one aligns the beam on the 2nd iris after a given mirror and uses the preceding mirror to re-center on the nearer iris. This process is repeated as necessary until the beam is aligned through both irises. Then the forward iris becomes the rear iris and the next iris becomes the forward iris and the procedure is repeated.

At the beginning of the path is a collimation stage to adjust the beam

diameter and provide collimation. This was setup very precisely originally and realigning to the irises after it is sufficient to set the beam path through the lenses without the need to remove the lenses and rebuild it each time. The probe beam path is inherently more stable than the pump beam path since it does not involve the OPA.

Near the end of the probe beam path is the pellicle beam splitter. Using it and the preceding mirror, the near IR beam was aligned for an initial alignment through the two irises in the detection system. One of which is immediately after the detection crystal and the other immediately precedes the Wollaston prism.

The mid IR pump beam necessary for THz generation with GaAs is not visible with an IR viewer. As a result, a HeNe beam as an alignment beam is a must. After the 2 to 3 meters necessary for beam divergence to a spot size that is large enough to prevent component damage the pump beam was passed through a 2.5 μm low pass filter. Next, a variable attenuator was placed so the beam intensity could be adjusted. In practice it was found that no attenuation was necessary. A beam splitter allowed both splitting off of 5 % of the power for reference monitoring purposes and simultaneously provided the input for the HeNe beam.

For alignment purposes the mirror just after that was temporarily removed and the iris before the mirror along with the distant iris for beam alignment shown in Figure 26 were used to align both HeNe and mid IR beams. The iris spacing was chosen to be the length of the pump path from

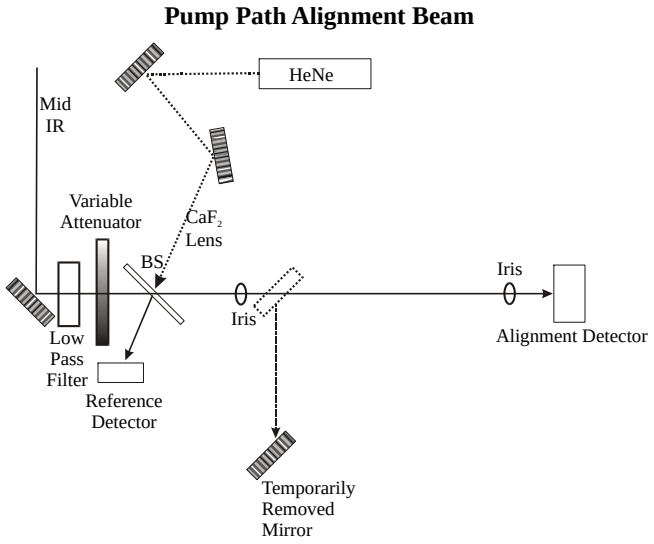

Figure 26: The mid IR beam is passing the final mirror of the beam divergence stage shown in Figure 11 previously. There is an iris mounted just before the temproarily removed mirror. The path between two irises has same length as the pump path from the beamsplitter to the sample location.

beam splitter to sample location. After the alignment was performed in the usual fashion the mid IR beam was blocked and the removed mirror replaced.

Next, the pump path was aligned using just the HeNe beam. The lens used to focus the beam on the sample and the sample were removed at first so the base alignment to the large iris could be made exact. Once this alignment was done the next step was to test the motorized linear stage system by moving the track from end to end and verifying the alignment beam stayed centered in the large iris. Figure 27 shows the entire pump path here with electro-optic detector details omitted as they were presented previously in the probe path. The probe path joins the pump path by the pellicle beam

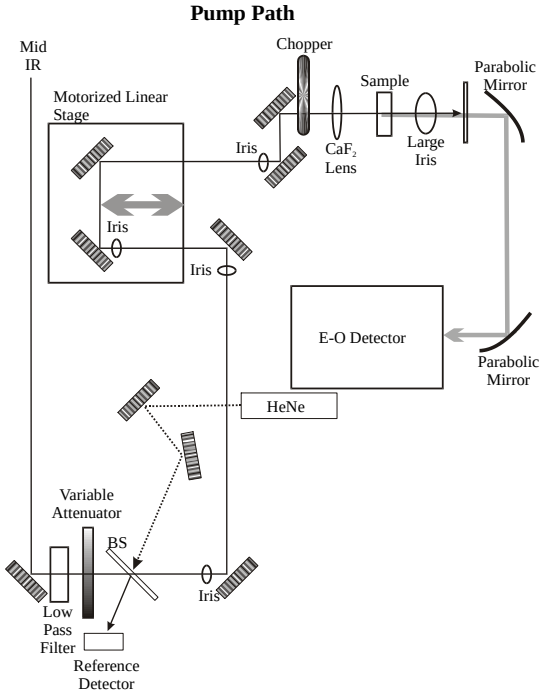

Figure 27: The pump path is aligned with the Helium-Neon beam. The beam is aligned and then the motorized linear stage is moved to the other end of its' range of trave and alignment checked. When aligned through both positions then the alignement through the Electro-Optic Detector can be completed.

splitter which is mounted just slightly closer to the detector system than the last parabolic mirror.

After the baseline beam alignment the 200 mm CaF_2 lens used to focus the mid IR beam on the sample was placed back in the linear stage that holds it and adjusted so that the beam was centered on the large iris again . Then the beam path for the detection system was adjusted next. the beam was adjusted to go through the iris immediately after the detection crystal and

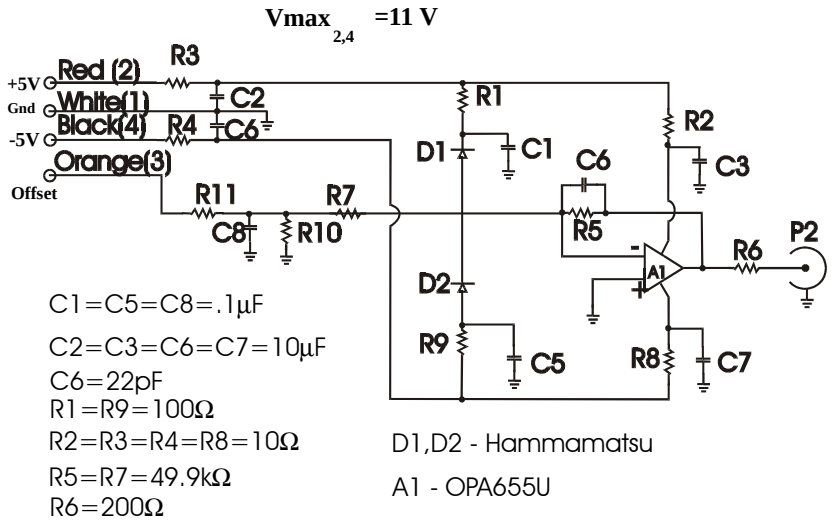

Figure 28: This is the working schematic drawn by Joe Magner after discussions and design sessions with the author and Yun-Shik Lee for the detector used in the 2 color THz-TDS system.

a second iris immediately before the Wollaston prism as shown in previously in Figure 27.

The HeNe beam through the system was then used to align the Wollaston prism output through the two mirrors onto the detector pair. There was a special detector made specifically for the legend system different from that used with the Mira as the source laser system. It was found that this was not necessary. I obtained the best results using the internally amplified Mira detector with the internal amplifier off. It has a similar circuit designed for the faster 76 MHz repetition rate of the Mira. The Legend 1 KHz detector schematic is shown in Figure 28.

One can see that in this detector the outputs are separated and averaging

is done in the lock-in amplifier. This design was built based on a design provided by Oksana Ostroverkhova. After several sessions between the author, Joe Magner and Dr. Lee this design was chosen and Joe Magner constructed it.

Then the last step for pump beam alignment was to place the sample and align it so the reflected HeNe beam was overlapped with the incident HeNe beam as before in the z-scan experiment.

The optical chopper was placed before the focusing lens to the sample and synchronized to the 1KHz trigger signal from the Legend system with a divide by two ratio so that every other pulse would be passed through the system when operating.

The probe beam was again unblocked and the pump beam blocked. The beam alignment to the detectors was checked. The detector system was hooked both to the lock-in amplifier and to an oscilloscope at this point for fine tuning. First, one detector was blocked with a beam stop. Then the output signal of the unblocked detector was maximized by fine adjustment of the appropriate mirror. The beam stop was moved to block the freshly adjusted path and the procedure repeated to maximize signal on both paths. After maximizing the detectors, the polarizer just before the Wollaston prism was adjusted until the signal from the pair of detectors together was minimized.

The probe beam was dialed to a minimum at this point as that had by testing been shown to introduce the least noise in the signal.

The pump beam was then unblocked at that point and the HeNe beam

blocked. The lock-in amplifier was timed using the 500 Hz reference locked output from the optical chopper control box. The appropriate software was used in the data acquisition computer (Either THz.vi or pp.vi mattering on whether the ESP300 had the motorized stage attached in position 1 or 2). The stage was positioned to t_0 using the ESP300r.vi positioning software and the appropriate parameters entered into the data acquisition software.

Data on this experiment was collected by the author. The wavelength was accurately measured afterwards using the monochromator.

9.1 THz Time Domain Spectroscopy on Quasi-Phased Matched GaAs Structures

In recent years a large number of different nonlinear materials have been used to generate THz by optical rectification using femtosecond pulses. In the case of ZnTe the matching of group velocities between THz and 800 nm optical pulses has been shown to make it an excellent wide band THz source. On the other hand, the group velocity mismatch in $LiNbO_3$ has been used advantageously to the development of poled structures for quasi-phase matching to generate narrowband multi-cycle THz pulses. [30][32]-[57]

The technique involves simply inverting the crystal structure so that $\chi^{(2)}$ reverses direction at the boundary after a distance approximately equal to the walk-off length, d_w, inside the structure. This can be repeated for as many cycles as desired. Recalling the equation for the walk-off length, $d_w = \frac{c\tau}{n_{THz}-n_{opt}}$, where c is the speed of light, τ is the duration of the optical pulse, n_{THz} is the group index of refraction in the crystal for the THz, and n_{opt} is the optical pulse group index of refraction; we see that a mismatch allows some interesting behavior in OR that we couldn't get with a phase-matched material like ZnTe. However, zincblende material have many nice properties such as an in general high d_{eff} and for GaAs a low THz absorption coefficient as noted in the previous section.

Further, the front and back surfaces contribute more than a half-cycle to the pulse and so the output power is higher than the square of the number

of layers times the power of one layer as one would expect.. This has been shown by Lee, et al[1] in simulations the contributions were shown to be 6.5 times the power for a 4 layer sample.

With the small difference in refractive indices at 2 μm ($\Delta n = 3.61 - 3.431 = .18$) As this wavelength is a mid IR absorption minimum in the 3PA range available to the OPA in our lab this made it ideal for experimentation. Since this data is also useful in development of other nonlinear technologies such as all optical switching and mid IR OPO's this was of interest to many as well as an eminently performable experiment.

The walk-off length for this case is $d_w \approx .17$ mm, when using 100 femtosecond duration pulses. Theoretical analysis led to the conclusion that between 4 and 8 times the walk-off length for a quasi-phased matched period would reduce the broad low frequency peak and high end harmonics. This places the optimal range from .7 to 1.4 mm thick.[1]

Using 1 mm thick 2" diameter GaAs wafers from AXT, we tested a stack of 4 wafers in a periodically inverted structure as compared to a single wafer. These wafers were provided by Microtech Instruments who also developed a stacking technique resulting in well contacted surfaces with properties much like the diffusion bonding process[70]. These samples are referred to as "Optically Contacted GaAs" or OC-GaAs in brief.

Figure 29 shows the OC-GaAs THz-TDS results. The factor of 6.5 between the power from a single wafer and a stack of 4 wafers matches the numerical solution well as do the waveforms themselves. The frequency,

Sample	Length (mm)	QPM Period (μm)
A10	10	1277
B6	6	759
B10	10	759

Table 2: Orientation Patterned GaAs samples tested using 2 color THz-TDS

ν_{THz}, calculated as before gives .83 THz which is in good agreement with the measured .84 THz.

We also tested 3 orientation patterned (OP-GaAs) samples provided by Stanford University that had been grown by David Bliss at the Air Force Research Laboratory in Hanscom, MA. These samples are listed in Table 12.2

When placed in the two color THz-TDS system constructed by the author the A10, B6, and B10 samples generated narrow band multi-cycle THz with pulse durations of 5.0, 3.6 and 6.0 ps respectively as can be seen in Figure 30. Comparison of the samples shows the expected band narrowing with longer samples matching theory[7]. It also shows the effects of water vapor. This can be seen in time domain as the continued oscillations long after the optical pulse exited the sample. It is more pronounced in the B6 and B10 samples as would be expected since they are near known water lines (HITRAN water spectrum). The calculated spectrum for the A10 sample was 1.31 THz. It measured by FWHM methods as 1.7 THz Looking at the data and the asymmetric valleys cut into the peak by water absorption is the probable explanation for the discrepancy here. The B6 and B10 samples

peak at 2.2 THz with a predicted value of 2.21. It can be seen that the free induction decay from the water vapor has increased the higher frequency components but the bandwidth of the 'ringing' as it is commonly referred to is so wide that the effect on the spectrum is to produce a sideband next to the peak and not a significant shift of the peak. This is an effect I commonly observed in other experiments not presented here as they are not directly related to GaAs research.

These results are in good agreement with the earlier results from the interferogram experiment. This demonstrates that both OP-GaAs and OC-GaAs results are in good agreement with theory. The predictions verified for QPM structures open the way to generation on a large spectral range using GaAs.

The OC-GaAs samples are easier to manufacture with a large clear aperture for up to 5 layers but manufacturing difficulties involving surface flatness and dust contamination begin making for diminishing returns beyond 5 layers using existing techniques.

OP-GaAs can be theoretically grown to any structure desired but aperture thickness so far is a problem. David Bliss has made significant progress in this department recently and long term OP-GaAs holds more promise with precision engineered structures.

Diffusion bonding is still the overall best when it can be done. Unfortunately, no one is currently making samples by this difficult process.

9.2 Conclusion

GaAs can indeed be used to generate large THz signals using a mid IR pump. The slight group index of refraction mismatch makes QPM narrowband and shaped pulse structures possible with fairly large dimensions compared to other materials such as $LiNbo_3$. This is advantageous as it simplifies manufacturing and makes for more precise control as manufacturing techniques for GaAs are very well developed.

Further advantages such as the high d_{eff} and low THz absorption are very promising. With the addition of an OPO and using DFG instead of OR others have shown that cascading takes place opening the possibility of surpassing the Manley-Rowe limit of 1 to 1 photon production.[71]

However, there are still significant problems that any device requiring precise beam paths such as an OPO would face. The self-focusing and self phase modulation produced by nonlinear refraction are still quite significant. Worse, the nonlinear refraction is fairly constant out into the longer wavelengths so even if one goes to higher order multiphoton absorption ranges such as 4 to 5PA band edge at 3.5 μm where we found such excellent power production one would still face the same self-focusing and self phase modulation.

With an appropriate designed device to minimize the n_2 effects GaAs offers the prospect of very high THz production using optical pumping in the mid IR range.

A Appendix 1: Direct 2 Parabolic Bandgap Model of Multiphoton Absorption Coefficients

A.1 Both Even and Odd N

Starting from the were I left off in Chapter 3 we can step by step solve this system. Do so by following the same iterative procedure and recognizing the intermediate state starts from energy E_{bv}.Then the denominator term from this intermediate state will have $2\hbar\omega$ as this is the intermediate transition energy mismatch. Then we see:

$$(103)\quad M_{cv}^{(3)} = \sum_{a,b} \frac{H'_{cb} H'_{ba} H'_{av}}{(E_{bv} - 2\hbar\omega)(E_{av} - \hbar\omega)}$$

This process can be extended indefinitely. Again, in the denominator we see the energy mismatches. These mismatches make $M_{cv}^{(N)}$ proportional to the uncertainty lifetime ($\frac{\hbar}{\Delta E}$)of each intermediate state as one would expect. This result requires the perturbation to be off diagonal as is the case for our chosen presupposed dominant contribution from the $\overrightarrow{A} \cdot \overrightarrow{P}$ interaction term.

Now to complete the analysis of W_N we need to define H'_{fi}. In terms of the intensity H'_{fi} can be defined using the index of refraction, n, the unit

polarization, $\overrightarrow{\epsilon}$,and the electron momentum matrix element, $\overrightarrow{p}_{fi}$, as follows:

$$(104)\quad H'_{fi} = \frac{e}{im\omega}(\frac{2\pi I}{nc})^{1/2}\overrightarrow{\epsilon}\cdot\overrightarrow{p}_{fi}$$

The $\sum_{cv}$simplifies to $\frac{2}{(2\pi)^3}\int k^2 dk^3$. The 2 in the numerator is due to spin degeneracy. Equations for the valence and conduction band energies can be written as follows:

$$(105)\quad E_c = \frac{\hbar^2 k^2}{2m_1} + E_g, E_v = -\frac{\hbar^2 k^2}{2m_2}$$

where $E_g$is the energy difference at $k = 0, m_1$ and m_2 are the conduction effective mass and valence effective mass. Then the effective mass during transition is found by the reduced mass formula. So then writing E_{cv} in these terms gives:

$$(106)\quad E_{cv} = \frac{\hbar^2 k^2}{2}(\frac{1}{m_1} - \frac{1}{m_2}) + E_g = \frac{\hbar^2 k^2}{2m_{cv}} + E_g$$

Now substitute the on resonance value for k ($k_r^2 = \frac{2m_{cv}}{\hbar^2}(N\hbar\omega - E_g)$) in so that the integral becomes the angular averaged value at the resonant state so it looks as follows:

(107)

$$W_N = \frac{2\pi}{\hbar}(\frac{2}{(2\pi)^3}\int k^2\delta(\frac{\hbar^2k^2}{2m_{cv}}+E_g-N\hbar\omega)(\frac{e}{m\omega})^{2N}(\frac{2\pi I}{nc})^N \left\langle \left|S_{cv}^{(N)}(k_r)\right|^2 \right\rangle dk^3)$$

Where $S_{cv}^{(N)}(k_r)$ carries all the $\frac{\overrightarrow{\epsilon}\cdot\overrightarrow{p}_{fi}}{Ecv-(N-i)\hbar\omega}$ math components. Example:

$$\begin{aligned}
(108a) S_{cv}^{(1)}(k_r) &= \overrightarrow{\epsilon}\cdot\overrightarrow{p}_{cv} \\
(108b) S_{cv}^{(2)}(k_r) &= \sum_a \frac{\overrightarrow{\epsilon}\cdot\overrightarrow{p}_{ca}}{E_{av}(k_r)-\hbar\omega}\overrightarrow{\epsilon}\cdot\overrightarrow{p}_{av} \\
(108c) S_{cv}^{(3)}(k_r) &= \sum_{a,b} \frac{\overrightarrow{\epsilon}\cdot\overrightarrow{p}_{cb}}{E_{av}(k_r)-\hbar\omega}\frac{\overrightarrow{\epsilon}\cdot\overrightarrow{p}_{ba}}{E_{bv}(k_r)-2\hbar\omega}\overrightarrow{\epsilon}\cdot\overrightarrow{p}_{av}
\end{aligned}$$

Simplifying after doing the angular part of our integration gives:

$$(109)\quad W_N = \frac{1}{\pi\hbar}(\frac{e}{m\omega})^{2N}(\frac{2\pi I}{nc})^N \left\langle \left|S_{cv}^{(N)}(k_r)\right|^2 \right\rangle \int k_r^2\delta(\frac{\hbar^2k^2}{2m_{cv}}+E_g-N\hbar\omega)dk^3$$

$$\begin{aligned}
(110)\qquad W_N = \frac{1}{\pi\hbar}(\frac{e}{m\omega})^{2N}(\frac{2\pi I}{nc})^N \left\langle \left|S_{cv}^{(N)}(k_r)\right|^2 \right\rangle \frac{2m_{cv}}{\hbar^2}(N\hbar\omega-E_g) \\
\int \delta(k^2+\frac{2m_{cv}}{\hbar^2}(E_g-N\hbar\omega))dk
\end{aligned}$$

Completing the now much simplified integral gives the formula

$$(111)\quad W_N = \frac{1}{\pi\hbar}(\frac{e}{m\omega})^{2N}(\frac{2\pi I}{nc})^N(\frac{2m_{cv}}{\hbar^2})^{3/2}(N\hbar\omega - E_g)^{1/2}\left\langle\left|S_{cv}^{(N)}(k_r)\right|^2\right\rangle$$

So far, this result is identical with the one obtained by Wherrett [3] as I have followed and expounded on his derivation from first principles to here. Using the Kane parameter[72] and numerical functions defined as follows: $\left\langle|p_{cv}|^2\right\rangle = f_{2N}(mP/\hbar)^{2N}, p_{cv} = fm_{cv}P/\hbar$ Wherrett obtained the following:

$$(112)\qquad K_N = \frac{N^{2N}}{\sqrt{2}}(2\pi)^{N-1}(\frac{e^2}{\hbar c})^N f^{-3}\frac{\hbar^{3N-1}}{m^{2N}}\frac{1}{n^N P^3 E_g^{2N-3}}$$
$$\frac{(N\hbar\omega/E_g - 1)^{1/2}}{(N\hbar\omega/E_g)^{2N-1}}\left\langle\left|S_{cv}^{(N)}(k_r)\right|^2\right\rangle$$

A.2 Odd N

In the case when N is odd the solution is easiest so we will do it first. For the value k_r, $E_{cv}(k_r) = N\hbar\omega$. Then, recognizing which of the summed variables are c or v using this as we walk from valence to conduction band back and forth as needed to keep with $E_{cv}(k_r)$ and walking through the sums we have:

$$(113a)\quad S_{cv}^{(3)} = \frac{p_{cv}p_{vc}p_{cv}}{(0-2\hbar\omega)(3\hbar\omega-\hbar\omega)}$$
$$(113b)\quad = \frac{p_{cv}p_{vc}p_{cv}}{(-2\hbar\omega)(2\hbar\omega)}$$

$$S_{cv}^{(5)} = \frac{p_{cv}p_{vc}p_{cv}p_{vc}p_{cv}}{(0-4\hbar\omega)(5\hbar\omega-3\hbar\omega)(0-2\hbar\omega)(5\hbar\omega-\hbar\omega)} \tag{114a}$$

$$S_{cv}^{(5)} = \frac{p_{cv}p_{vc}p_{cv}p_{vc}p_{cv}}{(-4\hbar\omega)(2\hbar\omega)(-2\hbar\omega)(4\hbar\omega)} \tag{114b}$$

$$S_{cv}^{(7)} = \frac{p_{cv}p_{vc}p_{cv}p_{vc}}{(0-6\hbar\omega)(7\hbar\omega-5\hbar\omega)(0-4\hbar\omega)} \frac{p_{cv}p_{vc}p_{cv}}{(7\hbar\omega-3\hbar\omega)(0-2\hbar\omega)(7\hbar\omega-\hbar\omega)} \tag{115}$$

$$S_{cv}^{(7)} = \frac{p_{cv}p_{vc}p_{cv}p_{vc}p_{cv}p_{vc}p_{cv}}{(-6\hbar\omega)(2\hbar\omega)(-4\hbar\omega)(4\hbar\omega)(-2\hbar\omega)(6\hbar\omega)} \tag{116}$$

By inspection there are factors of $(2\hbar\omega)^{N-1}$in the denominator. Also in the denominator we see $(-1)^{(N-1)/2}((\frac{N-1}{2})!)^2$ so we can write the Nth term now as:

$$S_{cv}^{(N)} = \frac{p_{cv}\left|p_{cv}\right|^{N-1}}{(-1)^{(N-1)/2}((\frac{N-1}{2})!)^2(2\hbar\omega)^{N-1}} \tag{117}$$

Then using our substitutions as before with the Kane parameter we get

$$(118)\quad K_N = \sqrt{2}\frac{\pi^{N-1}}{2^N}\frac{N^{4N-2}}{((\frac{N-1}{2})!)^4}\frac{f_{2N}}{f^3}(\frac{e^2}{\hbar c})^N\frac{P^{2N-3}}{n^N E_g^{4N-5}}\frac{(N\hbar\omega/E_g-1)^{1/2}}{(N\hbar\omega/E_g)^{4N-3}}$$

A.3 Even N

Next, is even photon absorption which is trickier as the combination must alternate between our $E_{cv}(k_r)$ and 0 as if one photon does nothing and the other does the transition up or down as the case is needed since we need an even number of transitions ending in the opposite band. Then we have for $S_{cv}^{(2)}$

$$(119)\quad S_{cv}^{(2)} = \frac{p_{cv}p_{vv}}{-\hbar\omega} + \frac{p_{cc}p_{cv}}{\hbar\omega}$$

This raises the issue of how to handle the diagonal elements. They are given by $p_{ii} = m\hbar k/m_i$[72]. k goes to k_r and m_i becomes m_{cv} Continuing on as done for the odd cases gives $S_{cv}^{(N)}$

$$(120)\quad S_{cv}^{(N)} = \frac{N}{2(N-1)!}p_{cv}\left|p_{cv}\right|^{N-2}\frac{m\hbar k_r}{m_{cv}(\hbar\omega)^{N-1}}$$

Then it is handled in the same way with the Kane parameter[72] and E_g.

(121)

$$K_N = \sqrt{2}\pi^{N-1}2^{N-1}N^{4N}((N-1)!)^2\frac{f_{2N-2}}{f}(\frac{e^2}{\hbar c})^N\frac{P^{2N-3}\hbar^{N-1}}{n^N E_g^{4N-5}}\frac{(N\hbar\omega/E_g-1)^{3/2}}{(N\hbar\omega/E_g)^{4N-3}}$$

B Appendix 2: Derivation of Nonlinear Refraction

B.1 General Derivation

First, to include the Raman transitions and Stark effects we could more formally write

$$(122)\quad S = \frac{i}{\hbar}\int_{-\infty}^{\infty} dt \int dr^3 \psi_c^*(\overrightarrow{k}, \overrightarrow{r}, t) H_{int} \psi_v(\overrightarrow{k}', \overrightarrow{r}, t)$$

For a 2 frequency component beam a new $\overrightarrow{A}$ will have to be defined. Using 2 different frequencies with the same linear polarization gives:

$$(123)\quad \overrightarrow{A} = \widehat{a}(A_{01}\cos(\omega_1 t) + A_{02}\cos(\omega_2 t + \phi))$$

Now we need wave functions to describe the process with different ω's which in turn generates the extra terms necessary to calculate in a more refined fashion near the band edges. To accomplish this first a Bloch type wave function must be constructed.[12][74]

$$(124)\quad \psi_i(\overrightarrow{k},\overrightarrow{r},t) = u_i(\overrightarrow{k},\overrightarrow{r})e^{i\overrightarrow{k}\cdot\overrightarrow{r}-\frac{i}{\hbar}\int_0^t E_i(\tau)d\tau}$$

Here, $u_i(\overrightarrow{k},\overrightarrow{r})$is the Bloch wave function for the appropriate band represented by i in the subscript field. The energy for the appropriate band is found by considering the Stark shifted band energies. There will be single photon time independent linear Stark shifting, E_{i0}, time independent quadratic Stark shifting terms, ΔE_{ij}(where $i \neq j$), and a field intensity interaction time dependent Stark shifting term, $\Delta E_{ii}(\tau)$, to consider here.

$$(125a)\quad E_c(\tau) = E_{c0} + \Delta E_{cc}(\tau) + \Delta E_{cv}$$

$$(125b)\quad E_v(\tau) = E_{v0} + \Delta E_{vv}(\tau) + \Delta E_{vc}$$

$$(125c)\quad E_{c0} = E_g + \frac{\hbar^2 k^2}{2m_c}$$

$$(125d)\quad E_{v0} = \frac{\hbar^2 k^2}{2m_v}$$

$$(125e)\quad \Delta E_{ii}(\tau) = -\frac{e\hbar}{m_i c}\overrightarrow{k}\cdot\overrightarrow{A}(\tau)$$

$$(125f)\quad \Delta E_{vc} = -\Delta E_{cv}$$

$$(125g)\quad = -\frac{(\frac{eA_{02}}{2mc})^2\left|\widehat{a}\cdot\overrightarrow{p}_{vc}\right|^2}{(E_g+\frac{\hbar^2k^2}{2m_c}-\hbar\omega_2)(E_g+\frac{\hbar^2k^2}{2m_c}+\hbar\omega_2)}$$

Defining a few simplifying terms[12]:

$$(126)\quad \hbar\omega_{vc} = E_g - \Delta E_{vc} + \Delta E_{cv} + \frac{\hbar^2 k^2}{2m_{cv}}$$

where m_{cv} is the reduced mass given by

$$\frac{1}{m_{cv}} = \frac{1}{m_c} - \frac{1}{m_v}$$

Then

$$(127a)\quad E_c(\tau) = \hbar\omega_{vc} + E_{v0} - \frac{e\hbar}{m_c c}\overrightarrow{k}\cdot\overrightarrow{A}(\tau) + \Delta E_{vc}$$

$$(127b)\quad E_v(\tau) = E_{v0} - \frac{e\hbar}{m_v c}\overrightarrow{k}\cdot\overrightarrow{A}(\tau) + \Delta E_{vc}$$

First finding the wave functions by substituting in our energy relationships:

$$(128)\quad \psi_v(\overrightarrow{k},\overrightarrow{r},t) = u_v(\overrightarrow{k},\overrightarrow{r})e^{i\overrightarrow{k}\cdot\overrightarrow{r} - \frac{i}{\hbar}\int_0^t (E_{v0} - \frac{e\hbar}{m_v c}\overrightarrow{k}\cdot\overrightarrow{A}(\tau) + \Delta E_{vc})d\tau}$$

Substituting in for $\overrightarrow{A}$:

$$(129)\qquad \psi_v(\overrightarrow{k},\overrightarrow{r},t) = u_v(\overrightarrow{k},\overrightarrow{r})e^{i\overrightarrow{k}\cdot\overrightarrow{r}}\exp[-\frac{i}{\hbar}\int_0^t (E_{v0} - \frac{e\hbar}{m_v c}\overrightarrow{k}\cdot\widehat{a} \\ (A_{01}\cos(\omega_1\tau) + A_{02}\cos(\omega_2\tau+\phi)) + \Delta E_{vc})d\tau]$$

Next, doing the same for the conduction wave function.

$$(130)\quad \psi_c(\overrightarrow{k},\overrightarrow{r},t) = u_c(\overrightarrow{k},\overrightarrow{r})e^{i\overrightarrow{k}\cdot\overrightarrow{r} - \frac{i}{\hbar}\int_0^t(\hbar\omega_{vc}+E_{v0}-\frac{e\hbar}{m_c c}\overrightarrow{k}\cdot\overrightarrow{A}(\tau)+\Delta E_{vc})d\tau}$$

Again substituting for $\overrightarrow{A}$:

$$(131)\qquad \psi_c(\overrightarrow{k},\overrightarrow{r},t) = u_c(\overrightarrow{k},\overrightarrow{r})e^{i\overrightarrow{k}\cdot\overrightarrow{r}}\exp[-\frac{i}{\hbar}\int_0^t (\hbar\omega_{vc} + E_{v0} - \frac{e\hbar}{m_c c}\overrightarrow{k}\cdot\widehat{a} \\ (A_{01}\cos(\omega_1\tau) + A_{02}\cos(\omega_2\tau+\phi)) + \Delta E_{vc})d\tau$$

Taking the complex conjugate.

$$(132)\qquad \psi_c^*(\overrightarrow{k},\overrightarrow{r},t) = u_c^*(\overrightarrow{k},\overrightarrow{r})e^{-i\overrightarrow{k}\cdot\overrightarrow{r}}\exp[\int_0^t (i\omega_{vc} + \frac{iE_{v0}}{\hbar} - \frac{ie}{m_c c}\overrightarrow{k}\cdot\widehat{a} \\ (A_{01}\cos(\omega_1\tau) + A_{02}\cos(\omega_2\tau+\phi)) - \Delta E_{vc})d\tau]$$

Now, examining the interaction Hamiltonian and making the appropriate substitutions:

$$
\begin{aligned}
(133a) H_{int} &= -\frac{e}{mc}\overrightarrow{A}\cdot\overrightarrow{P} \\
(133b) &= -\frac{e}{mc}\widehat{a}(A_{01}\cos(\omega_1 t)+A_{02}\cos(\omega_2 t+\phi))\cdot\overrightarrow{P} \\
(133c) &= -\frac{e}{mc}(A_{01}\cos(\omega_1 t)+A_{02}\cos(\omega_2 t+\phi))\widehat{a}\cdot\overrightarrow{P} \\
(133d) &= -i\frac{e\hbar}{mc}(A_{01}\cos(\omega_1 t)+A_{02}\cos(\omega_2 t+\phi))\widehat{a}\cdot\nabla
\end{aligned}
$$

Substituting the various pieces into the equation for S next:

$$
\begin{aligned}
(134)\qquad S = \frac{i}{\hbar}\int_{-\infty}^{\infty} dt \int dr^3 u_c^*(\overrightarrow{k},\overrightarrow{r})(-i\frac{e\hbar}{mc})e^{-i\overrightarrow{k}\cdot\overrightarrow{r}} \\
e^{-\frac{i}{\hbar}\int_0^t(-\hbar\omega_{vc}-E_{v0}+\frac{e\hbar}{m_c c}\overrightarrow{k}\cdot\widehat{a}(A_{01}\cos(\omega_1\tau)+A_{02}\cos(\omega_2\tau+\phi))-\Delta E_{vc})d\tau} \\
(A_{01}\cos(\omega_1 t)+A_{02}\cos(\omega_2 t+\phi)\widehat{a}\cdot\nabla)u_v(\overrightarrow{k},\overrightarrow{r}) \\
e^{i\overrightarrow{k}\cdot\overrightarrow{r}-\frac{i}{\hbar}\int_0^t(E_{v0}-\frac{e\hbar}{m_v c}\overrightarrow{k}\cdot\widehat{a}(A_{01}\cos(\omega_1\tau)+A_{02}\cos(\omega_2\tau+\phi))+\Delta E_{vc})d\tau}
\end{aligned}
$$

Recognizing some of the common parts in the exponents that cancel:

$$
\begin{aligned}
(135)\qquad S = \frac{i}{\hbar}\int_{-\infty}^{\infty} dt \int dr^3 u_c^*(\overrightarrow{k},\overrightarrow{r}) \\
e^{-i\overrightarrow{k}\cdot\overrightarrow{r}-\frac{i}{\hbar}\int_0^t(-\hbar\omega_{vc}+\frac{e\hbar}{m_c c}\overrightarrow{k}\cdot\widehat{a}(A_{01}\cos(\omega_1\tau)+A_{02}\cos(\omega_2\tau+\phi)))d\tau} \\
(-i\frac{e\hbar}{mc}(A_{01}\cos(\omega_1 t)+A_{02}\cos(\omega_2 t+\phi))\widehat{a}\cdot\nabla) \\
u_v(\overrightarrow{k},\overrightarrow{r})e^{i\overrightarrow{k}\cdot\overrightarrow{r}-\frac{i}{\hbar}\int_0^t(-\frac{e\hbar}{m_v c}\overrightarrow{k}\cdot\widehat{a}(A_{01}\cos(\omega_1\tau)+A_{02}\cos(\omega_2\tau+\phi)))d\tau}
\end{aligned}
$$

Combining where appropriate and using our reduced mass definition in the exponent again:

$$(136) \qquad S = \frac{i}{\hbar}\int_{-\infty}^{\infty} dt \int dr^3 u_c^*(\overrightarrow{k}, \overrightarrow{r})$$
$$e^{-i\overrightarrow{k}\cdot\overrightarrow{r} - \frac{i}{\hbar}\int_0^t(-\hbar\omega_{vc} + \frac{e\hbar}{m_{cv}c}\overrightarrow{k}\cdot\widehat{a}(A_{01}\cos(\omega_1\tau) + A_{02}\cos(\omega_2\tau+\phi)))d\tau}$$
$$(-i\frac{e\hbar}{mc}(A_{01}\cos(\omega_1 t) + A_{02}\cos(\omega_2 t + \phi))\widehat{a}\cdot\nabla)$$
$$u_v(\overrightarrow{k}, \overrightarrow{r})e^{i\overrightarrow{k}\cdot\overrightarrow{r}}$$

Now rearranging the time and space components:

$$(137) \qquad S = \frac{e}{mc}\int_{-\infty}^{\infty}(A_{01}\cos(\omega_1 t) + A_{02}\cos(\omega_2 t + \phi))$$
$$e^{-\frac{i}{\hbar}\int_0^t(-\hbar\omega_{vc} + \frac{e\hbar}{m_{cv}c}\overrightarrow{k}\cdot\widehat{a}(A_{01}\cos(\omega_1\tau) + A_{02}\cos(\omega_2\tau+\phi)))d\tau}dt$$
$$\int u_c^*(\overrightarrow{k}, \overrightarrow{r})e^{-i\overrightarrow{k}\cdot\overrightarrow{r}}(\widehat{a}\cdot\nabla)u_v(\overrightarrow{k}, \overrightarrow{r})e^{i\overrightarrow{k}\cdot\overrightarrow{r}}dr^3$$

First, doing the τ integrals as they are the simplest:

$$(138) \qquad S = \frac{e}{mc}\int_{-\infty}^{\infty}(A_{01}\cos(\omega_1 t) + A_{02}\cos(\omega_2 t + \phi))$$
$$e^{\omega_{vc}t - i\frac{e}{m_{cv}c}\overrightarrow{k}\cdot\widehat{a}(\frac{A_{01}}{\omega_1}\sin(\omega_1 t) + \frac{A_{02}}{\omega_2}\sin(\omega_2 t+\phi))}dt$$
$$\int u_c^*(\overrightarrow{k}, \overrightarrow{r})e^{-i\overrightarrow{k}\cdot\overrightarrow{r}}(\widehat{a}\cdot\nabla)u_v(\overrightarrow{k}, \overrightarrow{r})e^{i\overrightarrow{k}\cdot\overrightarrow{r}}dr^3$$

Now doing the spatial integration first breaking it into parts.

$$(139)\quad \int u_c^*(\overrightarrow{k}, \overrightarrow{r}) e^{-i\overrightarrow{k}\cdot\overrightarrow{r}} (\widehat{a}\cdot\nabla) u_v(\overrightarrow{k}, \overrightarrow{r}) e^{i\overrightarrow{k}\cdot\overrightarrow{r}} dr^3 = \int u_c^*(\overrightarrow{k}, \overrightarrow{r})(\widehat{a}\cdot\nabla) \times u_v(\overrightarrow{k}, \overrightarrow{r}) dr^3 + \int u_c^*(\overrightarrow{k}, \overrightarrow{r}) u_v(\overrightarrow{k}, \overrightarrow{r}) e^{-i\overrightarrow{k}\cdot\overrightarrow{r}} (\widehat{a}\cdot\nabla) e^{i\overrightarrow{k}\cdot\overrightarrow{r}} dr^3$$

Next, taking the gradient of the latter piece.

$$(140)\quad \int u_c^*(\overrightarrow{k}, \overrightarrow{r}) e^{-i\overrightarrow{k}\cdot\overrightarrow{r}} (\widehat{a}\cdot\nabla) u_v(\overrightarrow{k}, \overrightarrow{r}) e^{i\overrightarrow{k}\cdot\overrightarrow{r}} dr^3 = \int u_c^*(\overrightarrow{k}, \overrightarrow{r})(\widehat{a}\cdot\nabla) u_v(\overrightarrow{k}, \overrightarrow{r}) dr^3 + i\widehat{a}\cdot\overrightarrow{k} \int u_c^*(\overrightarrow{k}, \overrightarrow{r}) u_v(\overrightarrow{k}, \overrightarrow{r}) dr^3$$

Recognizing the orthogonality in the resulting last piece and rearranging the remaining part:

$$(141a)\quad \int u_c^*(\overrightarrow{k}, \overrightarrow{r}) e^{-i\overrightarrow{k}\cdot\overrightarrow{r}} (\widehat{a}\cdot\nabla) u_v(\overrightarrow{k}, \overrightarrow{r}) e^{i\overrightarrow{k}\cdot\overrightarrow{r}} dr^3 = \int u_c^*(\overrightarrow{k}, \overrightarrow{r})(\widehat{a}\cdot\nabla) u_v(\overrightarrow{k}, \overrightarrow{r}) dr^3$$

$$(142)\quad \int u_c^*(\overrightarrow{k}, \overrightarrow{r}) e^{-i\overrightarrow{k}\cdot\overrightarrow{r}} (\widehat{a}\cdot\nabla) u_v(\overrightarrow{k}, \overrightarrow{r}) e^{i\overrightarrow{k}\cdot\overrightarrow{r}} dr^3 = \widehat{a}\cdot\int u_c^*(\overrightarrow{k}, \overrightarrow{r}) \nabla u_v(\overrightarrow{k}, \overrightarrow{r}) dr^3$$

Defining our familiar interband momentum element here[12]:

$$(143)\quad \overrightarrow{p}_{vc} = -i\hbar \int u_c^*(\overrightarrow{k}, \overrightarrow{r})\nabla u_v(\overrightarrow{k}, \overrightarrow{r})dr^3$$

Then S becomes

$$(144)\ S = \frac{i}{\hbar}\frac{e\widehat{a}\cdot\overrightarrow{p}_{vc}}{mc}\int_{-\infty}^{\infty}(A_{01}\cos(\omega_1 t) + A_{02}\cos(\omega_2 t+\phi)) \\ e^{\omega_{vc}t - i\frac{e}{m_{cv}c}\overrightarrow{k}\cdot\widehat{a}(\frac{A_{01}}{\omega_1}\sin(\omega_1 t)+\frac{A_{02}}{\omega_2}\sin(\omega_2 t+\phi))}dt$$

Next, defining a term to simplify the appearance of the time integral[12]

$$(145)\quad \eta_i = \frac{eA_{0i}}{m_{cv}c\omega_i}\overrightarrow{k}\cdot\widehat{a}$$

So the action now is

$$(146)\qquad S = \frac{i}{\hbar}\frac{e\widehat{a}\cdot\overrightarrow{p}_{vc}}{mc}\int_{-\infty}^{\infty}(A_{01}\cos(\omega_1 t) + A_{02}\cos(\omega_2 t+\phi)) \\ e^{\omega_{vc}t - i\eta_1\sin(\omega_1 t) - i\eta_2\sin(\omega_2 t+\phi))}dt$$

Now making use of the identity to transform this into a integrable form

$$(147)\quad e^{i\eta\sin(\omega t)} = \sum_{n=-\infty}^{\infty} J_n(\eta)e^{in\omega t}$$

Transforms the action into

$$(148)\qquad S = \frac{i}{\hbar}\frac{e\widehat{a}\cdot\overrightarrow{p}_{vc}}{mc}\int_{-\infty}^{\infty}(A_{01}\cos(\omega_1 t) + A_{02}\cos(\omega_2 t+\phi))e^{\omega_{vc}t}$$
$$\sum_{n=-\infty}^{\infty} J_m(\eta_1)e^{im\omega t}\sum_{n=-\infty}^{\infty} J_n(\eta_2)e^{in\omega t}dt$$

Substituting the appropriate Euler formula for $cos(\omega t)$ this is broken into 4 integrals which then can be integrated using orthogonality and the definition of Dirac delta functions.

$$(149)\qquad S = \frac{i}{\hbar}\frac{e\widehat{a}\cdot\overrightarrow{p}_{vc}}{mc}\int_{-\infty}^{\infty}(A_{01}(\frac{e^{i\omega_1 t}+e^{-i\omega_1 t}}{2}) + A_{02}(\frac{e^{i\omega_2 t}+e^{-i\omega_2 t}}{2}))$$
$$e^{\omega_{vc}t}\sum_{m=-\infty}^{\infty} J_m(\eta_1)e^{im\omega t}\sum_{n=-\infty}^{\infty} J_n(\eta_2)e^{in\omega t}dt$$

$$(150)\qquad S = \frac{i\pi e\widehat{a}\cdot\overrightarrow{p}_{vc}}{\hbar mc}\sum_{m=-\infty}^{\infty}\sum_{n=-\infty}^{\infty} J_m(\eta_1)J_n(\eta_2)$$
$$(A_{01}\delta((m\pm 1)\omega_1 + n\omega_2 + \omega_{vc}) + A_{02}\delta(m\omega_1 + (n\pm 1)\omega_2 + \omega_{vc}))$$

This S Matrix is much more general as it applies to any multiphoton process. This more general result can be used to derive the earlier result within a factor of $\frac{\pi}{5}$. It can also be used to give more accurate calculations near the band edge.

B.2 Derivation of β from the general results

In the case where one limits it to $\omega_1$with $A_{02} = 0$, using the first order Maclaurin expansion for the Bessel functions and choosing the two photon absorption terms only $(m = -1, n = 0)$ then this reduction results in the same form of transition amplitude as before in terms of frequency dependence. There is a slight difference in the numerical factors. This can be seen utilizing $A_{01}^2 = \frac{8\pi c I_1}{n\omega_1^2}$ then the transition amplitude is

$$W = \sum_{spin} \int |S|^2 \frac{dk^3}{(2\pi)^3} \tag{151a}$$

$$= \sum_{spin} \int (\frac{\pi A_{01} e\widehat{a} \cdot \overrightarrow{p}_{vc}}{mc\hbar})^2 (\frac{eA_{01}\widehat{a} \cdot \overrightarrow{k}}{m_{cv}c\omega_1})^2 \frac{1}{2} \delta(\omega_{vc} - 2\omega_1) \frac{dk^3}{(2\pi)^3} \tag{151b}$$

Since for this case we are ignoring the Stark effect ω_{vc} simplifies giving:

$$W = \sum_{spin} \int (\frac{\pi A_{01} e\widehat{a} \cdot \overrightarrow{p}_{vc}}{mc\hbar})^2 (\frac{eA_{01}\widehat{a} \cdot \overrightarrow{k}}{m_{cv}c\omega_1})^2 \frac{1}{2} \delta(\frac{E_g + \frac{\hbar^2 k^2}{2m_{cv}}}{\hbar} - 2\omega_1) \frac{dk^3}{(2\pi)^3} \tag{152}$$

Consider that $\overrightarrow{p}_{vc}$ is parallel to $\overrightarrow{k}$ for this 2 band case then the integral becomes

$$(153) \qquad W = \sum_{spin} (\frac{A_{01} e\pi}{mc\hbar})^2 (\frac{eA_{01}}{m_{cv} c\omega_1})^2 \int_{\pi}^{0} \int k^4 \left|\overrightarrow{p}_{vc}\right|^2 \cos^4(\theta) \delta(\frac{E_g + \frac{\hbar^2 k^2}{2m_{cv}}}{\hbar} - 2\omega_1) \frac{dk}{(2\pi)^3} d\cos(\theta)$$

The angular integral immediately gives 1/5 leaving the k integral itself. Which gives the 3/2 power expected

$$(154a) \qquad W = \frac{1}{5} \sum_{spin} (\frac{A_{01} e\pi}{mc\hbar})^2 (\frac{eA_{01}}{m_{cv} c\omega_1})^2 \left|\overrightarrow{p}_{vc}\right|^2 \frac{1}{2} (\frac{2m_{cv}}{\hbar^2})^{5/2} \int (\frac{\hbar^2 k^2}{2m_{cv}})^{3/2} \delta(E_g + \frac{\hbar^2 k^2}{2m_{cv}} - 2\hbar\omega_1) \frac{d(\frac{\hbar^2 k^2}{2m_{cv}})}{(2\pi)^3}$$

$$(155) \quad W = \frac{1}{5} \sum_{spin} \frac{1}{(2\pi)^3} (\frac{A_{01} e\pi}{mc\hbar})^2 (\frac{eA_{01}}{m_{cv} c\omega_1})^2 \left|\overrightarrow{p}_{vc}\right|^2 \frac{1}{2} (\frac{2m_{cv}}{\hbar^2})^{5/2} (2\hbar\omega_1 - E_g)^{3/2}$$

Rearranging, summing over spins, recognizing $2m_{cv} = m_c$, and substituting for the amplitude:

$$(156)\quad W = \frac{2^4\pi}{5}\frac{e^4}{n^2c^2}\frac{I_1^2}{\hbar^6\omega_1^6}\frac{m_c^{1/2}\left|\overrightarrow{p}_{vc}\right|^2}{m^2}(2\hbar\omega_1 - E_g)^{3/2}$$

Next using the appropriate identity from the $\overrightarrow{k}\cdot\overrightarrow{p}$ theory[9][72]

$$(157)\quad \frac{\left|\overrightarrow{p}_{vc}\right|^2}{m^2} = \frac{E_g}{2m_c}$$

$$(158)\quad W = \frac{2^4\pi}{5}\frac{e^4}{n^2c^2}\frac{I_1^2}{\hbar^6\omega_1^6}\frac{E_g}{2m_c^{1/2}}(2\hbar\omega_1 - E_g)^{3/2}$$

Multiplying by $2\hbar\omega_1 I^{-2}$ to get the absorption coefficient, β:

$$(159)\quad \beta = \frac{2^4\pi}{5}\frac{e^4}{n^2c^2}\frac{1}{\hbar^5\omega_1^5}\frac{E_g}{2m_c^{1/2}}(2\hbar\omega_1 - E_g)^{3/2}$$

Next rearranging and using definitions of Kane parameters as needed:

$$(160)\quad \beta = \frac{2^9\pi}{5}\frac{e^4}{m^{1/2}c^2}\frac{\sqrt{E_p}}{n^2E_g^3}\frac{(\frac{2\hbar\omega_1}{E_g} - 1)^{3/2}}{(\frac{2\hbar\omega_1}{E_g})^5}$$

This differs from Wherrett's results[3] by a factor of $\frac{\pi}{5}$. It is found to be within a factor of 5 and typically a scaling factor is fit using the frequency

dependent part of this relationship to give comparison between theory and actual measurements as the frequency dependence is found to be appropriate.[12]

B.3 Addition of the Raman Transition terms and the Nondegenerate ($\omega_1 \neq \omega_2$) 2 Photon Absorption

Consider the three cases corresponding to Figure 31. The first case is two photon absorption with different frequency photons and corresponds to the delta function $\delta(\omega_{vc} - \omega_1 - \omega_2)$. The second is one of two possible Raman Transitions in which time is ordered in the way one normally thinks of it, i.e. photon absorbed then destructive interference from the second photon leaving a small energy difference placing the electron in the conduction band and thus leaving a photon of the difference energy as the Raman emission this corresponds to the delta function $\delta(\omega_{vc} - \omega_1 + \omega_2)$. The third case is the quantum mechanically allowed bizarre case in which the interference happens after the Raman emission corresponding to the delta function $\delta(\omega_{vc} + \omega_1 - \omega_2)$. Due to the Uncertainty principle this bizarre type of transition in which cause seemingly precedes effect is allowed within a certain time window.

Looking at the action again for these terms first recalling our derived expression.

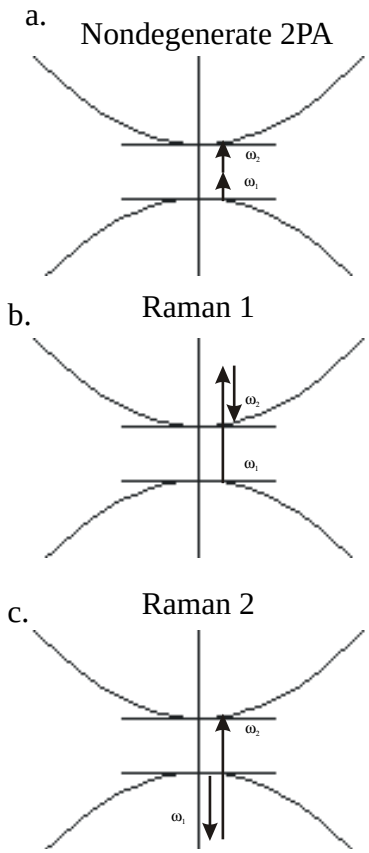

Figure 29: Three cases for two photon interactions are shown here. In a. the nondegenerate 2 photon absorption case where $\omega_1 \neq \omega_2$. Shown in b. is the standard time ordered Raman Transition where the system responds to the first photon and then the second. The last case, c., shows the acausal Raman transition where the second arriving photon changes the system first.

$$(161) \qquad S = \frac{i\pi e\widehat{a}\cdot\overrightarrow{p}_{vc}}{\hbar mc}\sum_{m=-\infty}^{\infty}\sum_{n=-\infty}^{\infty} J_m(\eta_1)J_n(\eta_2)$$
$$(A_{01}\delta((m\pm 1)\omega_1 + n\omega_2 + \omega_{vc}) + A_{02}\delta(m\omega_1 + (n\pm 1)\omega_2 + \omega_{vc}))$$

First, Let's apply the first order Maclaurin expansion to the Bessel functions.

$$(162) \qquad S = \frac{i\pi e\widehat{a}\cdot\overrightarrow{p}_{vc}}{\hbar mc}\sum_{m=-\infty}^{\infty}\sum_{n=-\infty}^{\infty} \frac{\eta_1^m}{2^m m!}\frac{\eta_2^n}{2^n n!}$$
$$(A_{01}\delta((m\pm 1)\omega_1 + n\omega_2 + \omega_{vc})$$
$$+A_{02}\delta(m\omega_1 + (n\pm 1)\omega_2 + \omega_{vc}))$$

Now finding the 2PA term we keep only the terms which result in the appropriate delta function.

$$(163)\quad S = \frac{i\pi}{\hbar}\frac{e\widehat{a}\cdot\overrightarrow{p}_{vc}}{mc}(\frac{\eta_2}{2}A_{01}\delta(-\omega_1-\omega_2+\omega_{vc}) + \frac{\eta_1}{2}A_{02}\delta(-\omega_1-\omega_2+\omega_{vc}))$$

Now squaring this and paying attention to the definition of the η's.

$$(164) \qquad |S|^2 = (\frac{\pi}{\hbar}\frac{e\widehat{a}\cdot\overrightarrow{p}_{vc}}{mc})^2(\frac{\eta_2}{2}A_{01}\delta(-\omega_1-\omega_2+\omega_{vc})$$
$$+\frac{\eta_1}{2}A_{02}\delta(-\omega_1-\omega_2+\omega_{vc}))^2$$

$$(165) \qquad |S|^2 = (\frac{\pi}{\hbar}\frac{e\widehat{a}\cdot\overrightarrow{p}_{vc}}{mc})^2(A_{01}A_{02}\eta_1\eta_2 + \frac{A_{01}^2\eta_2^2}{4} + \frac{A_{02}^2\eta_1^2}{4})$$
$$\delta(-\omega_1 - \omega_2 + \omega_{vc})^2$$

$$(166) \qquad |S|^2 = (\frac{\pi}{\hbar}\frac{e\widehat{a}\cdot\overrightarrow{p}_{vc}}{mc})^2(A_{01}A_{02}\frac{eA_{01}}{m_{cv}c\omega_1}\overrightarrow{k}\cdot\widehat{a}\frac{eA_{02}}{m_{cv}c\omega_2}\overrightarrow{k}\cdot\widehat{a}$$
$$+\frac{A_{01}^2(\frac{eA_{02}}{m_{cv}c\omega_2}\overrightarrow{k}\cdot\widehat{a})^2}{4} + \frac{A_{02}^2(\frac{eA_{01}}{m_{cv}c\omega_1}\overrightarrow{k}\cdot\widehat{a})^2}{4})\delta(-\omega_1 - \omega_2 + \omega_{vc})^2$$

Rearranging

$$(167) \qquad |S|^2 = (\frac{\pi}{\hbar}\frac{e^2\widehat{a}\cdot\overrightarrow{p}_{vc}A_{01}A_{02}}{m_{cv}mc^2}\overrightarrow{k}\cdot\widehat{a})^2(\frac{1}{\omega_1\omega_2} + \frac{1}{4\omega_1^2} + \frac{1}{4\omega_2^2})$$
$$\delta(-\omega_1 - \omega_2 + \omega_{vc})^2$$

$$(168) \qquad |S|^2 = (\frac{\pi}{\hbar}\frac{e^2\widehat{a}\cdot\overrightarrow{p}_{vc}A_{01}A_{02}}{2m_{cv}mc^2}\overrightarrow{k}\cdot\widehat{a})^2(\frac{1}{\omega_1} + \frac{1}{\omega_2})^2$$
$$\delta(-\omega_1 - \omega_2 + \omega_{vc})^2$$

Finding the transition amplitude:

$$(169) \qquad W = \sum_{spin}\int(\frac{\pi}{\hbar}\frac{e^2\widehat{a}\cdot\overrightarrow{p}_{vc}A_{01}A_{02}}{2m_{cv}mc^2}\overrightarrow{k}\cdot\widehat{a})^2(\frac{1}{\omega_1} + \frac{1}{\omega_2})^2$$
$$\delta(-\omega_1 - \omega_2 + \omega_{vc})\frac{dk^3}{(2\pi)^3}$$

$$(170) \qquad W = (\frac{\pi}{\hbar}\frac{e^2 A_{01}A_{02}}{2m_{cv}mc^2})^2(\frac{1}{\omega_1}+\frac{1}{\omega_2})^2 \sum_{spin}\int(\widehat{a}\cdot\overrightarrow{p}_{vc}\overrightarrow{k}\cdot\widehat{a})^2\delta(-\omega_1-\omega_2+\omega_{vc})\frac{dk^3}{(2\pi)^3}$$

And the k space integral is the same as before so the results are

$$(171)\ W = \frac{1}{5}(\frac{\pi}{\hbar}\frac{e^2 A_{01}A_{02}}{2m_{cv}mc^2})^2(\frac{1}{\omega_1}+\frac{1}{\omega_2})^2\left|\overrightarrow{p}_{vc}\right|^2\frac{1}{2}(\frac{2m_{cv}}{\hbar^2})^{5/2}(\hbar\omega_1+\hbar\omega_2-E_g)^{3/2}$$

Rearranging and using $\overrightarrow{k}\cdot\overrightarrow{p}$ theory[9][72] as before leads to:[12]

$$(172) \qquad W = \frac{2^4\pi}{5}\frac{e^4}{n_1n_2c^2}\frac{m_c^{1/2}\left|\overrightarrow{p}_{vc}\right|^2}{m^2}\frac{I_1I_2}{(\hbar\omega_1)^2(\hbar\omega_2)^2} (\frac{1}{\hbar\omega_1}+\frac{1}{\hbar\omega_2})^2(\hbar\omega_1+\hbar\omega_2-E_g)^{3/2}$$

Now inputting this into our standard formula for β will result in an additional term to add in when calculating the change in absorption. For the absorption from input beam 1 due to beam 2:

$$(173)\ \beta = 2\frac{2^2\pi}{5}\frac{e^4}{m^{1/2}c^2}\frac{\sqrt{E_p}}{n_1n_2E_g^3}\frac{(\frac{\hbar\omega_1}{E_g}+\frac{\hbar\omega_2}{E_g}-1)^{3/2}}{\frac{\hbar\omega_1}{E_g}(\frac{\hbar\omega_2}{E_g})^2}(\frac{1}{\frac{\hbar\omega_1}{E_g}}+\frac{1}{\frac{\hbar\omega_2}{E_g}})^2$$

This is good in that one can see that when $\omega_1 = \omega_2$ this reduces to the previous formula. Showing that we have a consistent approach. It also shows the general derivation for 1 photon of each frequency as the only place the sign representing absorption or destructive interference appears is in the part to the 3/2 power.

Doing the two different Raman Transition cases is now simple as the integrals will look exactly the same except for the previously mentioned signs. So one can immediately see results as follows.[12]

$$\beta_{Raman} = 2\frac{2^2\pi}{5}\frac{e^4}{m^{1/2}c^2}\frac{\sqrt{E_p}}{n_1 n_2 E_g^3} \frac{((\frac{\hbar\omega_1}{E_g} - \frac{\hbar\omega_2}{E_g} - 1)^{3/2} + (-\frac{\hbar\omega_1}{E_g} + \frac{\hbar\omega_2}{E_g} - 1)^{3/2})}{\frac{\hbar\omega_1}{E_g}(\frac{\hbar\omega_2}{E_g})^2}(\frac{1}{\frac{\hbar\omega_1}{E_g}} + \frac{1}{\frac{\hbar\omega_2}{E_g}})^2 \tag{174}$$

B.4 Absorption Coefficient Changes Due to Induced Band Structure Shifting: Stark Effects

The stark effect is the result of perturbation in a band structure or discrete electronic configuration due to the presence of an electric field. For intense short duration beams incident on a sample the electric field of the beam itself will produce some stark shifting because of the spectrum width of the pulse. We can consider the change in two manners. The first is that the time varying field produces distortions in the shape of a given band changing how

it couples to itself. The second is the deformation affecting coupling between the two bands. The first one is referred to in literature as the linear Stark effect even though it is an AC effect. And the second is referred to as the quadratic Stark effect[12].

Physically, one can think of the linear effect as perturbing the final dressed states of the electrons or holes. Since this perturbation overall leads to an effective increase in energy one could think of it as an acceleration of the electrons or holes. This acceleration is equivalent to having a lower oscillator strength.

The quadratic Stark effect increases the total energy at every point on both bands so is effectively shifting the well as well as deforming it. This is thought of as 'blue-shifting the bandgap'.[12]

The band self coupling called the linear Stark shift[12] requires expanding the $J_0(\eta_2)$ to second order while the similar term for $J_0(\eta_1)$ remain until first order. The zero order Bessel function as we are looking at the band deformation interacting with itself. Then the appropriate S matrix term describing one photon absorption while the other photon does the deformation term starts as:

$$(175)\quad S = \frac{i\pi}{\hbar}\frac{e\widehat{a}\cdot\overrightarrow{p}_{vc}}{mc}(1-\frac{\eta_2^2}{4})A_{01}\delta(-\omega_1+\omega_{vc})$$

Notice that only the A_{01} delta term is relevant here as only one photon

is absorbed. Squaring this gives:

$$(176)\quad |S|^2 = (\frac{\pi e A_{01}}{\hbar m c})^2 \left|\widehat{a}\cdot\overrightarrow{p}_{vc}\right|^2 (1-\frac{\eta_2^2}{4})^2 \delta(-\omega_1+\omega_{vc})$$

So then the transition amplitude is given as:

$$(177)\quad W = \sum_{spin}\int (\frac{\pi e A_{01}}{\hbar m c})^2 \left|\widehat{a}\cdot\overrightarrow{p}_{vc}\right|^2 (1-\frac{\eta_2^2}{4})^2 \delta(-\omega_1+\omega_{vc})\frac{dk^3}{(2\pi)^3}$$

Substitution for η_2 takes us to

$$(178)\qquad W = \sum_{spin}\int (\frac{\pi e A_{01}}{\hbar m c})^2 \left|\widehat{a}\cdot\overrightarrow{p}_{vc}\right|^2 (1-(\frac{e A_{02}}{2 m_{cv} c \omega_2})^2 \left|\overrightarrow{k}\cdot\widehat{a}\right|^2)^2 \delta(-\omega_1+\omega_{vc})\frac{dk^3}{(2\pi)^3}$$

What is actually needed is the change in transition rate. This leaves the case where only the cross term between A_{01} and A_{02} survives. Then the change in transition rate is found to be from the simple integration above after substitution for the amplitudes and appropriate $\overrightarrow{k}\cdot\overrightarrow{p}$ theory changes[12][72]:

$$(179)\quad \Delta W = \frac{2^5\pi}{5}\frac{e^4}{n_1 n_2 c^2}\frac{m_c^{1/2}\left|\overrightarrow{p}_{vc}\right|^2}{m^2}\frac{I_1 I_2}{(\hbar\omega_1)^2(\hbar\omega_2)^4}(\hbar\omega_1 - E_g)^{3/2}$$

For the quadratic Stark effect consider the deformation of the conduction band by the second frequency. Then the difference in the valence to conduction energies at the maximum change will be:

$$\Delta E_{cv} = E_{cv_{\max}} - E_{cv\,\min} \tag{180a}$$

$$= \frac{\left(\frac{eA_{02}}{2mc}\right)^2 |\widehat{a}\cdot\overrightarrow{p}_{vc}|^2}{E_g + \frac{\hbar^2k^2}{2m_{vc}} - \hbar\omega_2} + \frac{\left(\frac{eA_{02}}{2mc}\right)^2 |\widehat{a}\cdot\overrightarrow{p}_{vc}|^2}{E_g + \frac{\hbar^2k^2}{2m_{vc}} + \hbar\omega_2} \tag{180b}$$

$$\Delta E_{cv} = \left(\frac{eA_{02}}{2mc}\right)^2 |\widehat{a}\cdot\overrightarrow{p}_{vc}|^2 \left(\frac{1}{E_g + \frac{\hbar^2k^2}{2m_{vc}} - \hbar\omega_2} + \frac{1}{E_g + \frac{\hbar^2k^2}{2m_{vc}} + \hbar\omega_2}\right) \tag{181}$$

Now as ΔE_{cv} is no longer zero we need the full ω_{vc} in our integration to get the transition rate. The low order Bessel function expansion works for this case for one photon absorption. Then the transition rate simply becomes:

$$W = \sum_{spin} \int \left(\frac{\pi e A_{01}}{\hbar mc}\right)^2 |\widehat{a}\cdot\overrightarrow{p}_{vc}|^2 \,\delta\left(E_g + \frac{\hbar^2k^2}{2m_{vc}} + \Delta E_{cv} - \Delta E_{vc} - \hbar\omega_1\right) \frac{dk^3}{(2\pi)^3} \tag{182}$$

Performing the simple integration gives:

$$(183)\ W = \frac{1}{40\pi}\sum_{spin}\frac{e^2A_{01}^2}{\hbar^2m^2c^2}(\frac{2m_{cv}}{\hbar^2})^{3/2}\left|\overrightarrow{p}_{vc}\right|^2(E_g+\Delta E_{cv}-\Delta E_{vc}-\hbar\omega_1)^{1/2}$$

With a slight rearrangement and recalling $\Delta E_{cv} = -\Delta E_{vc}$ we get this result in a Maclaurin series expandable form.

$$(184)\ W = \frac{1}{40\pi}\sum_{spin}\frac{e^2A_{01}^2}{\hbar^2m^2c^2}(\frac{2m_{cv}}{\hbar^2})^{3/2}\left|\overrightarrow{p}_{vc}\right|^2E_g^{1/2}(1+\frac{2\Delta E_{cv}}{E_g}-\frac{\hbar\omega_1}{E_g})^{1/2}$$

Now recognizing $\frac{2\Delta E_{cv}}{E_g} \ll 1$ and Maclaurin expanding to first order about it gives:

$$(185)\ W = \frac{1}{40\pi}\sum_{spin}\frac{e^2A_{01}^2}{\hbar^2m^2c^2}(\frac{2m_{cv}}{\hbar^2})^{3/2}\left|\overrightarrow{p}_{vc}\right|^2E_g^{1/2}((1-\frac{\hbar\omega_1}{E_g})^{1/2}+\frac{\frac{2\Delta E_{cv}}{E_g}}{(1-\frac{\hbar\omega_1}{E_g})^{1/2}})$$

To find the change in transition rate we need only the term that has both intensities in it. This comes from the expanded term only. Then the change in transition rate goes as follows.

$$(186)\ \Delta W = -\frac{1}{40\pi}\sum_{spin}\frac{e^2A_{01}^2}{\hbar^2m^2c^2}(\frac{2m_{cv}}{\hbar^2})^{3/2}\left|\overrightarrow{p}_{vc}\right|^2E_g^{1/2}\frac{\frac{2\Delta E_{cv}}{E_g}}{(1-\frac{\hbar\omega_1}{E_g})^{1/2}}$$

$$(187)\qquad = -\frac{1}{20\pi}\sum_{spin}\frac{e^2A_{01}^2}{\hbar^2m^2c^2}(\frac{2m_{cv}}{\hbar^2})^{3/2}\left|\overrightarrow{p}_{vc}\right|^2E_g^{1/2}\frac{\Delta E_{cv}}{(E_g-\hbar\omega_1)^{1/2}}$$

When substituting the definition of ΔE_{cv} in to the equation one must use the energy matched form. This is shown below.

$$(188)\quad \Delta E_{cv} = \int \Delta E_{cv}\delta(E_g + \frac{\hbar^2 k^2}{2m_{vc}} - \hbar\omega_1)dE(k)$$

$$(189a)\quad \Delta E_{cv} = \left(\frac{eA_{02}}{2mc}\right)^2 (\frac{|\widehat{a}\cdot\overrightarrow{p}_{vc}|^2}{E_g + \hbar\omega_1 - E_g - \hbar\omega_2} + \frac{|\widehat{a}\cdot\overrightarrow{p}_{vc}|^2}{E_g + \hbar\omega_1 - E_g + \hbar\omega_2})$$

$$(190)\quad \Delta E_{cv} = \left(\frac{eA_{02}}{2mc}\right)^2 |\widehat{a}\cdot\overrightarrow{p}_{vc}|^2 (\frac{1}{\hbar\omega_1 - \hbar\omega_2} + \frac{1}{\hbar\omega_1 + \hbar\omega_2})$$

Then with the change in interband energy matched to one photon absorption the substitution gives:

$$(191)\quad \Delta W = \frac{-1}{20\pi}\sum_{spin}\frac{e^2A_{01}^2}{\hbar^2m^2c^2}\left(\frac{eA_{02}}{2mc}\right)^2 (\frac{2m_{cv}}{\hbar^2})^{3/2}|\overrightarrow{p}_{vc}|^4\frac{E_g^{1/2}}{(E_g-\hbar\omega_1)^{1/2}} (\frac{1}{\hbar\omega_1 - \hbar\omega_2} + \frac{1}{\hbar\omega_1 + \hbar\omega_2})$$

Substitution for the amplitudes, summing over spins, the use of $\overrightarrow{k}\cdot\overrightarrow{p}$ theory[72] and rearrangement gives[12]:

$$(192) \qquad \Delta W = -\frac{4\pi}{5}\frac{e^4}{n_1 n_2 c^2}\frac{m_{cv}^{3/2}}{m^4}\left|\overrightarrow{p}_{vc}\right|^4 \frac{I_1 I_2}{(\hbar\omega_1)^2(\hbar\omega_2)^2}\frac{1}{(E_g-\hbar\omega_1)^{1/2}} \left(\frac{1}{\hbar\omega_1-\hbar\omega_2}+\frac{1}{\hbar\omega_1+\hbar\omega_2}\right)$$

Now, all the absorption changes can be summed up and applied to our Kramers-Krönig dispersion relation. There is a problem however, this integration produces divergences about zero. Others[12] have found that by expanding as a Laurent series around the origin all the terms but one can be made to vanish. These divergences and their introduction by the $\overrightarrow{A}\cdot\overrightarrow{P}$ theory approach are well known[73]. Using a manner described by Moss[16] these non-physical divergences are simply subtracted.

Following the same procedure Figure 13 (shown earlier) shows n_2 for GaAs as calculated for[74][15]. The scaling curve shown is a fitting for wide gap dielectrics[12] and appears good for the data taken at OSU while the initial curve seems to fit the one data point taken at Stanford University[15]. There is the distinct possibility that the Stanford data was taken with a different polarization orientation. Even though the propagation direction is the same anisotropy in the $\chi^{(3)}$ tensor may have come into play here and anisotropy is another topic.

C Appendix 3: Additional Measurement Procedures

Knife edge measurements are done on the mid IR beam at the location the GaAs sample is placed for this experiment. This should be the focal plane of the beam after the CaF_2 lens. A razor blade is taped to a mount that is attached to the moveable plate of a motorized translation stage. The stage is mounted to either provide vertical or horizontal motion across the beam path with the razor blade. The stage is computer controlled and our THz.vi or pp.vi software (depending on whether the stage is on the ESP300 controller box stage 1 or 2 position). The razor steps across the beam linearly reducing it's intensity profile. A pyroelectric detector is placed along with a 100 mm CaF_2 lens so that all the beam after the blade is incident on the detector. The detector output is sent to the DSP 830 Stanford Research systems lock-in amplifier where it is measured and the data sent to the computer for storage. This is then fit in Origin software with a model for a gaussian beam profile.

Consider the time averaged gaussian beam power calculated from the time averaged intensity. Assuming x and y directions may or may not be the same we wish to examine the x direction only. The equation for this is:

$$(193)\quad P = I_0 \int_{-\infty}^{\infty} \int_{-\infty}^{x} e^{-2(\frac{x'^2}{w_x^2}+\frac{y^2}{w_y^2})} dx' dy$$

Integration along y gives

$$P = I_0 w_y \sqrt{\frac{\pi}{2}} \int_{-\infty}^{x} e^{-2(\frac{x'^2}{w_x^2})} dx' \quad (194a)$$

$$= \frac{I_0 w_y}{2} \sqrt{\frac{\pi}{2}} (1 - \mathrm{erf}(\frac{2x}{w_x})) \quad (194b)$$

So the fit uses the parameters max, min, and w to give a fit to the data as col[B]=(max-min)/2*(1-erf(2*col[A]/w)). This fit has been found to work extremely well with as little as 50 data points.

After taking both horizontal and vertical measurements, collection of pulse duration data completes the needed intensity data. This was done with a Femtochrome autocorrelator.

The autocorellator is appropriately hooked up to the oscilloscope along with the timing signal from a chopper. The Mid IR beam is passed through a chopper at 10 Hz and aligned to the inlet of the autocorrelator so that the maximum autocorrelation signal is obtained. The appropriate detector is used in the autocorrelator for the spectral range. The careful use of the entry iris to keep the output voltage below 1 volt protects the detector in the autocorrelator. A 512 averaged data file is made with the oscilloscope that is then transferred to the computer for analysis.

The autocorrelation signal envelope is a gaussian pulse or a sech squared pulse. Using the appropriate wave form multiplier as listed in the manual after finding the FWHM one multiplies to get the pulse duration.

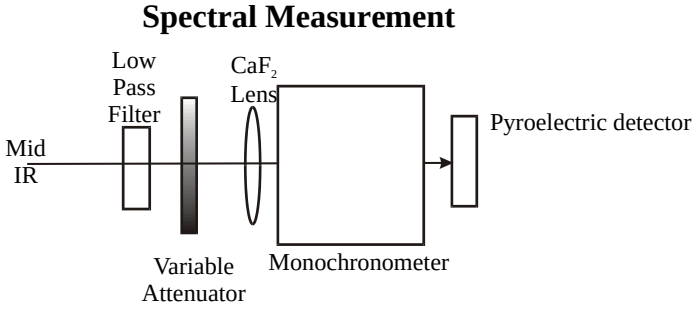

Figure 30: The Mid IR beam is filtered and attenuated as before. This is then passed through a very long focal length CaF■ lens such as one with f= 500 mm. This keeps the beam from spreading too much inside the monochronometer. The beam enters the monochrometer where the different wavelength components can be separated. The output is sent to a pyroelectric detector for measurement.

To accurately characterize the spectrum after characterizing the intensity the lenses from the beam path are removed and a very long focal length lens such as a 50 cm CaF_2 lens is placed into the beam path so that the beam remains small for a very long way. One then plans on placing the monochromator close to the lens and figures where to place a detector so that it will be just after the outlet of the monochromator. This is shown in Figure 32.

The detector is aligned to the beam using the detector output as seen on an oscilloscope. The monochromator is placed into the beam close to the lens so that the beam is incident on the inlet. The monochromator is adjusted to zero wavelength so the entire beam passes through (Zero order propagation). The slits on both ends are opened very wide and the monochromator moved

around until the signal is maximized on the detector coming through the monochromator. Next, the slits and oscilloscope are adjusted to throttle down the signal as far as possible while turning up the input power at the variable attenuator. The slits are adjust small until at full power in one gets around 400 mV displayed on the oscilloscope out. The wavelength is adjusted slightly back and forth around zero to find the peak. This is the offset. Our monochromator had a 4:1 ratio between the number and the actual wavelength with a typical offset of -4 nm. The wavelength is adjusted to find the edge of the spectral range. The detector output is manually recorded at each wavelength in the neighborhood of the mid IR wavelength centered around. The peak gives the center wavelength the OPA is actually operating at. If one found the peak to be numerically 521 on our monochromator then the actual wavelength was $4 \times (521 - 1)$nm= 2080nm.

a smaller 25 mm travel motorized linear stage was mounted at the appropriate angle for either vertical or horizontal travel on the 3 position stage the sample was previously connected to. The knife-edge was mounted to that stage so that the beam could be characterized in the appropriate direction. The correct software was used to control the smaller motorized stage for data collection purposes and the 3 position stage was used to match the position of the locator knife-edge with the moveable knife-edge so that an accurate measurement of the beam profile with respect to the sample location could be made.

The esp300r.vi software was used to control the larger stage so that mea-

surements could be taken along the entire z-scan zone. Beam profile measurements were taken both horizontally and vertically. More than 1 cm from the focal plane, as determined by beam waist analysis done between measurements, the spacing along the z axis was chosen to be 1 cm. Within 1 cm of the focal plane the spacing was typically 1 mm.

The beam waists were then fit to a focused gaussian beam profile using a fitting function in origin. The fitting function used the minimum waist in microns, w_0, the wavelength in microns, λ, and the position offset in microns, z_0, as parameters while using the position from the large stage as the independent variable and the waist measurement calculated by the other software as the dependent variable. The equation governing this is the standard focused gaussian beam equation.

$$w = w_0\sqrt{1 + (\frac{(z - z_0)\lambda}{\pi w_0^2})^2} \tag{195}$$

This fit was performed for both vertical and horizontal directions. Then the data used along with the pulse duration to characterize the intensity. From there the appropriate multiphoton absorption coefficient and the nonlinear refraction were calculated.

D Appendix 4: Experimental Setups and Procedures

D.1 Legend and OPerA Laser system basic operation

D.2 Introduction

The Coherent Legend laser system uses a seed femtosecond laser system (Mira 900F in our case) to feed the Legend regenerative amplifier the pulses that are stretched temporally and spatially then amplified in a Ti-Sapphire crystal. The Legend system uses a 1KHz repetition rate, 532 nm, pump beam from an Evolution diode pumped solid state laser (DPSS). After amplification the pulse is returned through the stretching grating system in the reverse direction to recompress the pulse back down to ~100 femtoseconds.

The Mira 900F is a regenerative amplifier that mode locks at 76 MHz repetition rate. It is pumped by a Verdi V10 ten Watt continuous wave DPSS.

For all of the experiments listed here after a 95%/5% beam splitter the major beam is sent to our Coherent OPerA optical parametric amplifier (OPA). Inside the OPA the beam is parametrically split (down converted) using a Ti-Sapphire crystal to produce two new outputs separated from the pump beam. The higher frequency one of these is called the signal output and has typically >200mW average power. The lower frequency has a much

lower power output of 0 to 80 mW typically and is called the Idler. There is also a beam dump since in nonlinear process there is never 100 % conversion. In general, I kept the beam dump blocked off for the purposes of the experiments.

There is a software control system run by laptop that allows one to start and stop the Legend and another software program to control the parametric amplification choice. The software for the OPA automatically adjusts the crystal angle to the desired angle for production of the wavelengths chosen. As energy is conserved there is a simple relationship governing what output to expect from a given input with a given signal wavelength choice. This energy conserved relationship is below.

$$\frac{1}{\lambda_{pump}} = \frac{1}{\lambda_{signal}} + \frac{1}{\lambda_{Idler}} \tag{196}$$

One very useful feature of this OPA is that the path lengths through the OPA are exactly identical until the output stage. This has several uses. For difference frequency generation all one needs to have overlapped beams co-propagating is to remove the dichroic mirror between the signal and Idler outputs. For the two color THz-TDS all one needs is to make the chosen pump beam move perpendicular in the direction from the beam dump towards the Idler. Make the beam go past the end of the OPA to feed into the THz-TDS system and once you have t_0 you have found t_0 for any pump

beam choice feeding in any other choice with the same orthogonality directed into the same pump path will maintain the same t_0.

One of the difficulties in using the output from the OPA is that the beams exit with very small diameters. The high intensity that results has been known to damage optics and in general a 2 meter to 3 meter path is needed before entering the output into more sensitive optics such as variable attenuators.

Another difficulty is that the OPA is very temperature sensitive. A change of 3 degrees Fahrenheit is enough to cause the output to become unstable and significantly lower the average power.

The final difficulty to consider is that the amplifier output is not radially uniform. For cases where an exact beam profile are needed the output must be sent through a spatial filter. That has the added problem that it significantly reduces available power. Profiling the gaussian spectrum is not a useful method unless the temperature is maintained exact as small temperature variations change the profile. Power fluctuations in the pump beam also lead to profile changes. And every time the system is started the profile is different due to many factors not the least of which is minute changes in the angle of entry for the pump beam.

D.3 System Startup and Adjustment

D.3.1 Mira 900F Start up and Adjustment

Prior to starting any laser system the first step is checking where your beam is going to go and making sure it is appropriately stopped. This is a very important safety consideration. Class 4 lasers such as the Mira or Legend can damage or even permanently blind a person in a fraction of a second.

In the following start up cycle a beam stop is placed after the first mirror of the Mira 900F output and the stop is placed at an angle so a small amount of scattering will occur in the direction of the fiber optic pick up of the Ocean Optics spectrum analyzer.

All high power laser systems should be started by first turning on the cooling system. This is to protect the gain medium (Titanium sapphire crystals in the Mira and Legend as well as the YAg crystals in the Evolution and Verdi pump lasers)

In the case of the Mira 900F the cooling system runs at 19 C so the Verdi V10 pump laser should be turned on very shortly thereafter to avoid condensation forming on the Ti-Sapphire crystal which can cause damage to it. The Verdi V10 is activated by a key on the control box for the Verdi system. When the Mira is used as a seed laser Verdi power is set to a lower level. As of late this has been 7 Watts.

The manual claims a 10 minute warm up time for the Mira system. This is not the case as observed in our lab. Typically, full thermal stabilization

requires an hour. Any attempt to tune the Mira before then is probably a futile effort.

Once warmed up, the power is optimized using the mirror adjustment controls starting with the ones controlling the entry beam steering. Using the Mira control box power display one then maximizes the signal. This optimizes the input beam through the sapphire crystal. Both for optimal conversion angle and feeding into the infrared resonant cavity.

Next one adjusts the mirrors responsible for the near infrared cavity alignment whose knobs are horizontally adjacent instead of the vertical alignment of the 2 pairs of input steering. After that both input beam and the generated near infrared cavity are maximized. Now the cavity is aligned to the optimal wave vector input angle from the sapphire crystal used as the gain medium in this resonant cavity.

Normally, as the Mira is near optimal at start, this procedure requires minimal adjusting and only one repetition. However, if the humidity in the room changes dramatically or an optical component in the cavity is moved/replaced one may need to repeat the process a time or two to reach optimum output.

The slit for cutting off the continuous wave (CW) mode when running mode locked is centered next. To do this, first, one cuts the power down to 1/4 the maximum power obtained by closing the slit with the appropriate one of the two knobs on the output coupler end of the Mira. And then one moves the slit center using the other knob until power is maximized again.

Last one opens the slit back up all the way.

On the laptop, one can monitor the spectrum by opening the Ocean Optics program and adjusting the spectral window to 775nm to 825 nm. In CW mode the spectrum should be a very steep vertical but still somewhat broad spectrum for a CW mode. This laser is designed to have many longitudinal modes simultaneously lasing. This broad spectrum capability of the Mira 900F cavity is what allows for the ~80 femtosecond pulses characteristic of it. Just recognizing that the nature of the Fourier transform of a short pulse in time is a wide band in frequency explains the need for this.

In addition to a wide spectral range one needs phase matching in the spectrum to produce the synchronization that sums into a single narrow pulse. This is provided initially by a shaking piece of glass mounted on a small vibrating piezoelectric motor. There is a horizontal toggle switch on the Mira control box marked CW at the left and ML in the middle. Only when the laser is running and mode locking is desired should this switch be activated. The reason for this is that the small vibrational piezoelectric motor has a limited lifetime so running it as little as possible is desired. The changing angle of the glass surfaces relative to the incident infrared beam in the cavity causes the beam to only be properly aligned for very brief times and this generates an optical pulse.. Once the internal photodiode detectors register a mode locked output this motor stops vibrating. It has produced the necessary short pulse. If the photodetector built into the Mira at any later time fails to detect a pulse the motor is automatically brought back on

to restart the mode-locked condition.

Now, to mode lock one can narrow the slit until the spectrum dramatically widens and the peak drops to the point the vertical scale needs readjustment. By small changes in aperture one sees where the spectrum stabilizes and appears to be gaussian with a width of greater than 10 nm full width half maximum (FWHM). I found the best results were typically with the FWHM around 14.3 to 14.6 nm. The center needs to be very close to 800nm for use as a seed laser for the Legend system. There is a metal control knob for the birefringent crystal that sets the spectral window in the cavity. by small adjustments with this knob the center can be set. Often, I found two mode locked windows, one with a higher peak output and a smaller bandwidth. The second wider bandwidth was at a slightly more narrow slit setting. Typically the second is the more stable.

To understand what is taking place inside the Mira to cause stable mode-locking consider the sapphire crystal itself. It is a nonlinear gain medium and will act as a Kerr lens. So the pulses being brighter than the CW waves are more tightly focused in the cavity. Then by narrowing the slit you are reducing the proportion of CW circulating in the cavity without reducing the pulses until one reaches about the pulse width. This lowers the cavity Q for the CW beam below what is necessary for lasing without lowering the pulse energy. The pulse is also effectively scavenging more and more of the populated excited states in the sapphire during transit through said crystal as well. This results in a stable mode-locked pulse. Additionally, the

more temporally narrow the beam the better the mode-locking versus CW separation as well.

To control the group velocity dispersion allowing for temporally shorter pulses a pair of prisms are used inside the cavity and adjusted by two black knobs near a metal adjustment knob. All optics in a cavity involving a band of frequencies at high peak powers have some dispersion characteristics. To solve this issue the two prisms are placed such that by adjusting the depth in the prism the beam passes. This is arranged to provide dispersion of opposite sign and magnitude to the dispersion of the rest of the cavity. Thus the pulse is recompressed to maintain femtosecond duration.

The metal knob is connected to a birefringent filter that allows one to chose the center frequency of the pulse. This is accomplished by the angle of incidence between he filter and the dispersion properties of the birefringent crystal. By small changes in the angle of the crystal the index of refraction changes and thus the band that is aligned with the cavity can be changed.

If the bandwidth needs adjustment there is a control knob for one of the prism pair that with slight adjustment will change the bandwidth of the spectral window. It, by virtue of the changing effective path length due to the different amount of prism insertion, also shifts the spectrum center so adjustment with the birefringent filter control is often necessary as well.

Once the mode locked pulse is well shaped with no CW mode left and appropriate spectrum obtained the beam stop can be carefully removed. This allows the beam to follow the path into the Legend seed beam entry point.

D.3.2 Legend Start up and Adjustment

For safety one makes sure the Legend output has a beam stop of some kind in place. Typically, I place the power meter as the beam stop since measurement of the Legend output is the first step once the legend is operational.

The Chiller for the legend runs at room temperature so the start up is a little different than the Mira. One starts the Lytron chiller and allows approximately 5 minutes time to reach thermal stabilization at 24 C.

On the laptop control computer one uses the software for the Evolution pump laser to start The system. There is other software to control the OPerA OPA. The Key on the evolution control box is turned to the on position. Next one checks the SDG control box for the Legend to see that all pockel cells (the pulse gate control system for this laser is two pockel cells) have their LEDs lit signifying a signal received from the seed laser. If there is one or both unlit then one hits the reset button to turn them on. Once both show enabled the fault indicator on the software window should go dark. Now one turns on the Evolution pump laser by left clicking and holding the green on button in the software window. One holds it until the red laser running square is lit up in the window and the on button goes bright green. This is usually accompanied by a loud click that signifies the evolution is on and the shutter has opened.

To understand what the physics involved with start up are consider how the Legend regenerative amplifier system actually works. The seed beam

from the Mira sends in a pulse. The pockel cells (coupled with appropriate optical components to act as an optical gate or mirror system) are switched on and off so that only one pulse passes in from the Mira every 1 ms. This pulse is then sent through a pair of reflective gratings positioned to stretch the pulse out temporally. The stretched pulse is then passed through a sapphire gain medium pumped by the 1 KHz Q switched Evolution laser. After passing through the gain medium the pulses are passed back through the same grating pair to re-compress the pulse. The single pulse makes multiple passes and a small beam splitter/photodetector system measures the pulse power on each pass. At some point the pockel cells switch to the output state after a number of passes set using the timing controls on the SDG control box. The amplified and re-compressed output pulse is then directed out of the cavity as an 800 nm, ~100 femtosecond duration, 1 KHz repetition rate high energy pulse. energies in the 1 mJ/pulse range are achieved this way.

The Legend SDG control box has an output with the internal Photodiode signal on it. This should be split off with a BNC T and sent to an oscilloscope along with the trigger signal out. One adjusts the oscilloscope to find the amplification pulse train measured by the photodiode mentioned earlier. Power is maximized once one maximizes this train on the display screen where changes are readily visible.

Using the last two mirrors on the seed input starting with the furthest from the legend, one adjusts the seed beam input to maximize the Legend pulse train. When the signal is maximized the legend is almost ready for use.

The Legend originally had a warm up time of less than 5 minutes. This no longer is the case and a 10 minute to 1 hour warm up time is typical. Once the power meter reads more than 940 mW the Legend output is large enough for OPA operation. Below that the OPA output will be marginal and unstable.

Next one blocks the OPA outputs and the legend output with beam stops. Then the power meter is moved into position to measure one of the OPA outputs once the appropriate beam stops are removed. There is a beam splitter on the Legend output just before the OPA input. For safety, one makes sure the split off 5% beam will be blocked when the Legend beam stop is removed.

To measure one unblocks the Legend output and the output to be measured on the OPA. Typically, I use the Idler as this is the one we used in most experiments. One uses the Legend compressor control to adjust the OPA output to maximum. If there is no output at the time beams are unblocked this typically means the compressor is too far out of adjustment.

By using a timing instrument such as a watch with a second hand to adjust by pressing one of the compressor control box adjustment buttons first in one direction while timing how far one adjusted (this is so that if you don't find the signal you can return to the previous setting). Using the pair of buttons one can search for the appropriate compressor setting. If one doesn't find the signal then one goes back in the other direction with the compressor until one has returned to the original position (same time in each

direction). Then one continues on in the unexplored direction until finding the signal. This is then optimized for maximum power. often I switch to the 'Slow' setting with the control knob once close to the correct compressor setting. This allows one to more accurately fine tune it.

Using the software on laptop control computer one can adjust the wavelength of the OPA as desired. Calibration, done as of the last visit by the Coherent technician, was a little sloppy. I find that 2047 nm on the Idler corresponded to 2080 nm according to the monochromator. I will give more on monochromator use later. One thing to be careful of is to make sure the input wavelength at the bottom of the software window says the center wavelength the Mira was tuned to.

At this point, one blocks the OPA output and remove the power meter. For safety one checks the beam path to make sure when unblocked that the OPA output will go to the desired experiment or at least to a terminating beam stop appropriately placed when assembling an experiment.

D.4 Shut Down Procedure

To shut down the system, one first blocks the output of the Legend. Next, one turns off the Evolution laser through the software window by the red stop button. Then turns off the key to the Evolution on the Evolution control box. After that one blocks the Mira output. Then one turns the Mira control box switch for mode locking to the CW position. One opens the Mira slit to maximum next. Then one turns off the key to the Verdi V10. Immediately

turn off the Verdi/Mira chiller. One waits 5 minutes and turn off the Legend chiller. Last, one closes all software and shuts down the Laptop control computer.

D.5 The Bolometer

The bolometer used was calibrated and loaned by Konstantin Vodopyanov of Stanford University. The bolometer requires cooling with liquid helium. It has a vacuum chamber around the liquid helium so as to lessen the rate heat flows in preserving the liquid helium longer. The design is rated at 24 hours for a liquid helium filling but in practice we found 8 hours typical. There is a 15 volt internal battery and there are two 9 Volt transistor batteries internally in the electronics section. They are not so easy to see unless one gets down to the battery level.

The vacuum chamber has a valve on the outside that after pump down is sealed. It is very easy to move this valve during the cryogenic filling process so great care needs to be taken with this valve as filling becomes impossible if the chamber is at atmospheric pressure. The liquid helium will boil off as fast as it fills.

The coolant filling process begins by filling both the liquid nitrogen chamber and the liquid helium chamber with liquid nitrogen. This is poured back into the liquid nitrogen dewar flask and then the liquid nitrogen chamber is refilled with liquid nitrogen. This is done to bring the entire device down towards 4 k with less liquid helium as liquid nitrogen is much cheaper, easier

to obtain, and work with. The transfer tube is then carefully inserted into the liquid helium tank with all other valves closed. The higher temperature of the transfer tube will result in boiling of the liquid helium pressurizing the container and forcing liquid helium through the transfer tube. Once a liquid jet of bluish tinted clear fluid begins to spray out of the transfer tube the bolometer is slid via the liquid helium chamber onto the transfer tube until the tube is all the way to the bottom of the liquid helium chamber in the bolometer. At first a small steaming stream will rise up as all the liquid helium is boiling off as in Figure 33. During the filling process one must be careful that an ice plug does NOT form in the chamber entrance or the bolometer will explode. When actual filling begins the steaming vapor will go down in volume coming back out of the chamber. When it is full the steam will become thick, strong, very short and wide with a funnel-like appearance. Close examinations showed small droplets coming up and out of the chamber. At this point one opens a valve on the liquid helium tank to release pressure. Then the transfer tube is removed. The bolometer switches are now all turned on with the gain set at the lowest setting. A voltage measurement of the Vs will show 6.6 to 6.9 Volts if the bolometer is operating correctly at this point.

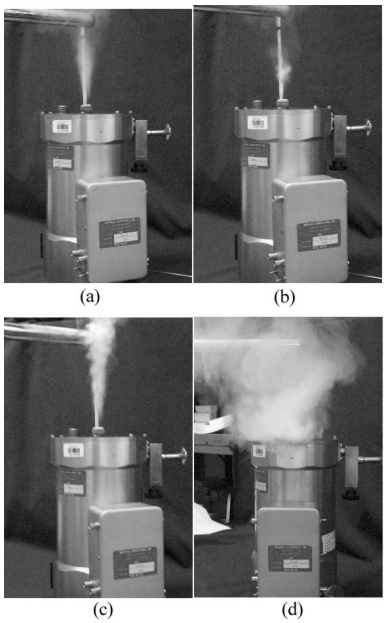

Figure 31: (a) This shows the initial filling when all helium is being boiled off. (b) Shows the drop in vapor associated with the commencement of actual filling after the chamber has cooled off enough for liquid helium to collect. (c) This is the normal vapor level that resumes during filling. (d) Here the profuse vapor stream is shown when the Bolometer is full. This view is from the side the vapor is drifting due to air currents and hids some of the features such as the shorter nature of the wider plume.

Bibliography

[1] Y. -S. Lee, W. C. Hurlbut, K. L. Vodopyanov, and M. M. Fejer, et al., SPIE **6120**, 612003 (2006).

[2] K. L. Vodopyanov, M. M. Fejer, Y. -S. Lee, W. C. Hurlbut, and V. G. Kozlov, Appl. Phys. Lett., Pending, (2006).

[3] B. S. Wherrett, J. Opt. Soc. Am B **1**, 67 (1984).

[4] A. Villeneuve, C. C. yang, G. I. Stegeman, C. -H.. Lin, H. -H Lin, Appl. Phys. Lett., **62** (1993)

[5] B. Gorshunov, A Volkov, I Spektor, A Prokhorov et al., Int. J. IRMMW **26**, 1273 (2005).

[6] V. G. Kozlov, www.mtinstruments.com, 2006.

[7] D. Mittleman, "Sensing With Terahertz Radiation", (Springer-Verlag, Berlin Heidelberg 2003).

[8] G. Gallot and D. Grischkowsy, J. Opt. Soc. Am. B **16**, 1204 (1999).

[9] A. Dragonmir, J. G. McInerney, and D. N. Nikogosyan, Appl. Opt. **41**, 4365 (2002).

[10] P. Kolodner, H. S. Kwok, J. G. Black, and E. Yablonovitch, Opt. Letters **4**, 38 (1979).

[11] S. Polyakov, F. Yoshino, and G. Stegeman, J. Opt. Soc. Am. B **18**, 1891 (2001).

[12] M. Sheik-Bahae, D. C. Hutchings, D. J. Hagan, and E. W. Van Stryland, IEEE J. Quantum Electron. **27**, 1296 (1991).

[13] Yun-Shik Lee, Lectures and disscussions on Point Group Symmetries, Oregon State University, (2006).

[14] R. Desalvo, M. Sheik-Bahae, A. A. Said, D. J. Hagan, and et al., Opt. Letters **18**, 194 (1993).

[15] W. C. Hurlbut, Yun-Shik Lee, K. L. Vodopyanov, and P.S. Kuo, Opt. Letters, Pending, (2006).

[16] D. J. Moss, E. Ghahramani, J. E. Sipe, and H. M. Van Driel, Phys. Rev. B **41**, 1542 (1990).

[17] W. A. Schroeder, D. S. McCallum, D. R. Harken, M. D. Dvorak, and et al., J. Opt. Soc. Am. B, 401 (1995).

[18] D. C. Hutchings, B. S. Wherrett, Phys. Rev. B **49**, 2418 (1994).

[19] R. W. Boyd, "Nonlinear Optics", (Academic Press, San Diego Ca, 1992).

[20] D. C. Hutchings, B. S. Wherrett, Phys. Rev. B **50**, 4622 (1994).

[21] D. C. Hutchings, B. S. Wherrett, Phys. Rev. B **52**, 8150 (1995).

[22] J. U. Kang, A. Villeneuve, M. Sheik-Bahae, G. I. Stegeman, and et al., Appl. Phys. Lett. **65** (2), 147 (1994).

[23] M. Sheik-Bahae, A. A. Said, T. -H. Wei, D. J. Hagan, and E. W. Van Stryland, IEEE J. of Quantum Electron., 26, (1990).

[24] A. E. Siegman, "Lasers", (University Science Books, Sausalito CA 1989).

[25] B. H. Bransden, C. J. Joachain, "Physics of Atoms and Molecules", (Prentice Hall Essex England 2003).

[26] A. Villeneuve, C. C. yang, G. I. Stegeman, C. N. Ironside, and et al., IEEE J. of Quantum Electron. **30**, 1172 (1994).

[27] K. Wynne, and J. J. Carey, Opt. Com., 400 (2005).

[28] T. Skauli, P.S. Kuo, K. L. Vodopyanov, T. J. Pinguet, et al., J. Appl. Phys. **94**, 6447 (2003).

[29] J. Faure, J. Van Tilborg, R. A. Kaindl, and W. P. Leemans, Opt. and Quantum Electron. **36**, 681 (2004).

[30] L. Xu, X. C. Zhang, and D. H. Auston, Appl. Phys. Lett. **61** (15), 1784 (1992).

[31] Y. H. Jin, and X. C. Zhang, J. Nonlinear Opt. Phys. M. **4**, 459 (1995).

[32] T. Meade, Y.-S. Lee, V. Perlin, H. Winful, and T. B. Norris, THz Symposium, (2000).

[33] T. B. Norris, Y. -S. Lee, T. Meade, M. DeCamp, V. Perlin, and H. Winful, CLEO/QELS, Postdeadline paper, (2000).

[34] Y. -S. Lee, T. B. Norris, A. V. Maslov, and D. S. Citrin, Ultrafast Phenomenon, (2000).

[35] Y. -S. Lee, T. Meade, T. B. Norris, and A. Galvanauskas, CLEO/QELS, Invited Paper, (2001).

[36] W. C. Hurlbut, N. Amer, and Y. -S. Lee, APS Northwest Section Meeting, Portland OR, (2003).

[37] N. Amer, W. C. Hurlbut, and Y. -S. Lee, APS Northwest Section Meeting, Portland OR, (2003).

[38] Y. -S. Lee, N. Amer, and W. C. Hurlbut, ThG3, Frontiers in Optics/Laser Science XIX, (2003).

[39] Y. -S. Lee, N. Amer, and W. C. Hurlbut, JThB4, Frontiers in Optics/Laser Science XIX, (2004).

[40] K. L. Vodopyanov, D. M. Simanovskii, M. M. Fejer, V. G. Kozlov, and Y. -S. Lee, CLEO/QELS, (2005).

[41] Y. -S. Lee, N. Amer, W. C. Hurlbut, and B. J. Norton, Optics East, Invited Paper, (2005).

[42] K. L. Vodopyanov, J. Schaar, M. M. Fejer, X. Yu, and et al., CLEO/QELS, (2006).

[43] K. L. Vodopyanov, M. M. Fejer, D. M. Simanovskii, V. G. Kozlov, and Y. -S. Lee, CLEO/QELS, (2006).

[44] N. Amer, J. Danielson, and Y. -S. Lee, CLEO/QELS, (2006).

[45] Y. -S. Lee, T. Meade, M. DeCamp, T. B. Norris, and A. Galvanauskas, Appl. Phys. Lett. **77**, 1244 (2000).

[46] Y. -S. Lee, T. Meade, M. DeCamp, M. L. Naudeau, and et al., Appl. Phys. Lett. **77**, 2488 (2000).

[47] Y. -S. Lee, T. Meade, T. B. Norris, and A. Galvanauskas, Appl. Phys. Lett. **78**, 3583 (2001).

[48] Y. -S. Lee, N. Amer, and W. C. Hurlbut, Optics and Photonic News **14**, 42 (2003).

[49] Y. -S. Lee, and T. B. Norris, J. Opt. Soc. Am. B **19**, 2791 (2002).

[50] Y. -S. Lee, N. Amer, and W. C. Hurlbut, Appl. Phys. Lett. **82**, 170, (2003).

[51] N. Amer, W. C. Hurlbut, B. J. Norton, Y. -S. Lee, T. B. Norris, Appl. Phys. Lett. **87**, 221111 (2005).

[52] Y. -S. Lee, N. Amer, and W. C. Hurlbut, B. J. Norton, and J. R. Danielson, Proc. SPIE 6002, 600211 (2005).

[53] W. C. Hurlbut, B. J. Norton, N. Amer, and Y. -S. Lee, J. Opt. Soc. Am. B **23**, 90 (2006).

[54] Y. -S. Lee, T. Meade, and T. B. Norris, Optics and Photonis News **12**, 46 (2001).

[55] W. C. Hurlbut, B. J. Norton, N. Amer, and Y. -S. Lee, J. Opt. Soc. Am. B **23**, 90 (2006).

[56] Y. -S. Lee, N. Amer, and W. C. Hurlbut, CLEO/QELS, (2003).

[57] M. Schall, and P. U. Jepsen, Appl. Phys. Lett. **77**, 2801 (2000).

[58] T. Yajima, N. Takeuchi, Jpn. J. Appl. Phys. **9**, 1361 (1970).

[59] K.H. Yang, P.L. Richards, Y.R. Shen, Appl. Phys. Lett. **19**, 320 (1971).

[60] Peter H. Siegel, IEEE Transactions on Microwave Theory and Techniques **50**, 910 (2002).

[61] A. G. Stepanov, J. Kuhl, I. Z. Kozma , E. Riedle, and et al., Optics Express **13**, 5762 (2005).

[62] Y. -S. Lee, T. Meade, V. Perlin, H. Winful, and et al., Appl. Phys. Lett. **76**, 2505 (2000).

[63] R. H. Stolen, Appl. Phys. Lett. **15**, 74 (1969).

[64] K. L. Vodopyanov, M. M. Fejer, D. M. Simanovskii, V.G. Kozlov, Y.-S. Lee, CLEO/QELS, CWMI, (2005).

[65] I. Tomita, H. Suzuki, H. Ito, H. Takenouchi, and et al., Appl. Phys. Lett. **88**, 071118 (2006) .

[66] L. A. Eyres, P. J. Tourreau, T. J. Pinguet, C. B. Ebert, and et al., Appl. Phys. Lett. **79**, 904 (2001).

[67] W.J. Moore, and R.T. Holm, J. Appl. Phys. **80**, 6939-42 (1996).

[68] K. L. Vodopyanov, Optics Express **14**, 2263-2276 (2006)

[69] V. G. Dmitriev, G. G. Gurzadyan, D. N. Nikogosyan, "Handbook of Nonlinear Optical Crystals", (Springer, Berlin, 1997).

[70] V. G. Kozlov, K. L. Vodopyanov, M. M. Fejer„ Y. -S. Lee, and W. C. Hurlbut, Int. Conf. IR and MM Waves, WedC4, 390 (2006).

[71] W.C Hurlbut, K. L. Vodopyanov, P. S. Kuo, M. M. Fejer, and et al., CLEO/QELS, (2006).

[72] E. O. Kane, J. Phys. Chem. Solids **1**, 249 (1937).

[73] H. D. Jones, and H. R. Reiss, Phys. Rev. B **16**, 2466 (1977).

[74] J. M. Worlock, "Laser Handbook", (Amsterdam: North Holland, 1972).